The design, calibration and usage of a solid scattering and absorbing phantom for near infra red spectroscopy

Michael Firbank B.Sc

Thesis submitted for the degree of Doctor of Philosophy (Ph.D) at the University of London.

Department of Medical Physics and Bioengineering.
University College London.

August 1994

Acknowledgements

Many thanks must go to my supervisor, Prof. David Delpy for providing such enthusiastic encouragement throughout the project, and for reading the seemingly endless number of drafts of the thesis. Also to Dr Jem Hebden for his encouragement as part of his search for the ultimate imaging phantom. José Pes created the collimators from my designs, and gave lots of advice on lathe operation. Mutsu Hiraoka improved the Monte Carlo code written by Dr Piet van der Zee. Other members of the department whose collective wisdom I benefitted from include Arlene, Clare, Dave, Humberto, Mark, Martin, Matthias, Matthias, Miles, Steve, Tim and Tony.

I am grateful to Jim Cambell of Zeneca Ltd for discussions on infra-red dyes, and for the numerous samples of dyes he provided. Also to Merck for information and samples of their wondrous amorphous silica spheres. To Prof. Boyde for allowing me to use his bone saw, and to Fred Stride for letting me loose on his scanning electron microscope.

Finally, I would like to thank my family, who supported me through the whole thing.

Abstract

Following a review of methods for measuring the optical properties of tissue, the majority of this thesis is concerned with the design, construction, calibration and use of a solid, tissue equivalent phantom.

The phantom material is a clear polyester plastic. This is obtained in unpolymerised form, scattering particles and absorbing dyes are added to it, and it is then polymerised to form a stable solid.

Purely scattering and absorbing phantoms were made separately, and their optical properties were measured using a specially built system. This has a co-linear collimated light source and detector, and measures the unscattered light transmitted through a sample as a function of its thickness.

Other methods of measuring the optical coefficients of tissue were tested with this phantom. One of these uses integrating spheres to measure the transmitted and reflected light from a sample. A model of light transport (in this case a Monte Carlo model) is used to convert these measurements into scattering and absorption coefficients. It was found that the measurement of scattering coefficient was reasonably accurate, but that the absorption coefficient was overestimated at the low values typical of tissue. A measurement of the optical properties of bone was made with this system. The other system investigated uses the diffusion theory to calculate optical properties from measurements made through a thick slab.

The material was also employed to create a test phantom for near infrared spectroscopy machines. This provides a diffusing medium with an attenuation that is variable in discrete steps over three orders of magnitude. The relative attenuation between steps is totally wavelength independent. This phantom was adopted by the EC concerted action on near infrared spectroscopy and imaging.

Finally, the phantom was used to create test objects with which to investigate the potential of imaging with infrared light

Contents

List of Figures

Chapter 1

Medical imaging and monitoring techniques

1.1 Introduction

The work described in this thesis is based around the development, testing and usage of a material which matches the optical properties of tissue in the near infra red region. The material (or phantom) is designed to be an aid to investigators in near infra red spectroscopy and imaging.

Near infra red spectroscopy (NIRS) was first used by Jöbsis in 1977[1a] can be used in vivo to measure the relative quantities of infra red absorbing substances, such as oxygenated and deoxygenated haemoglobin, and oxidised and reduced cytochrome aa_3, the terminal enzyme in the respiratory redox chain. Measurement of the amount of water in the tissues is also possible using derivative spectroscopy. Imaging systems which use infrared light are now also being developed, which as well as determining the absorption distribution, may also provide some information about the local optical scattering properties. This will make it possible to distinguish between different tissue types. NIRS imaging systems are likely to be used in the study of oxygen availability in the neonatal brain, particularly the localisation of ischaemic regions, and the detection of tumours, especially in the female breast. Tumours often have a greater absorption, due to their enhanced vascularity[1b]. They also have different light scattering properties to the surrounding tissue, resulting from their different structure.

The advantage of the NIRS technique is that it is non invasive, and that there is no evidence of it causing damage. It can therefore be used continuously. This is very helpful clinically, where periodic or continuous monitoring can be used to observe the development of symptoms, so the effects of procedures and treatments can be followed.

In the rest of this chapter, as an introduction to the current state of medical

monitoring, several well established non optical imaging techniques will be discussed, with respect to their clinical use and their advantages and disadvantages.

The next four chapters describe the optical properties of tissue in the near infra red, the modelling of light propagation in tissue and the specific techniques of NIR spectroscopy and imaging. This hopefully will give an understanding of the problems associated with the technique, and of the areas in which a stable tissue equivalent material is needed for investigation.

1.2 Alternative imaging techniques

1.2.1 Radiography

X rays are not greatly scattered by soft tissues, and the different tissue types absorb differing fractions of the incident radiation, ranging from fat which absorbs very little, to bone which is the strongest absorber. In simple radiographs, the source is placed on one side of the area in question, and a photographic plate detector on the other side. This method produces the familiar X ray pictures of bones. When it is used for breast tumour detection, this technique is called mammography; tumours often absorb more strongly than the surrounding tissue, since they are more dense, and as micro calcifications are present in 40% of tumours[2]. Using mammography, 93% of tumours are detected[3].

To obtain 2D slice images of the brain or other soft tissues, X ray tomography is used, where a collimated source and detector are located on opposite sides of the object, and data is acquired from rotational and translational scanning[4]. Although the risks of mammography are negligible (for every million forty year old women examined, 10 will go on to develop radiation induced cancer, as opposed to 800 who will have cancers detected by the radiography[5]) there is a perceived risk associated with the technique, which leads to its under use[6]. The relative risk from mammography increases in younger women due to both the reduced occurrence of natural cancer, and an increased risk of radiation induced cancer.[5]

1.2.2 Positron emission tomography (PET)

This technique involves the use of an injected radioactive isotope which decays, producing a positron. The positron annihilates almost immediately on meeting an electron in the surrounding medium, producing two photons (511 KeV) which have equal momentum and hence travel in opposite directions. Because of their high energy, there is little interaction between these photons and the surrounding tissue. The two photons are then detected using a ring of detectors (scintillator crystal and photo multiplier tubes) linked to coincidence counters[7]. The fact that the two photons arrive almost simultaneously on either side of the object allows spurious signals to be ignored and improves signal localization. The isotopes used in PET include ^{15}O, ^{11}C, ^{13}N and ^{18}F. These isotopes are used to label certain compounds, eg $H_2{}^{15}O$ and from the detected photons, an image of the compound distribution can be built up. PET has been used to measure cerebral blood flow using $H_2{}^{15}O$, cerebral blood volume using inhaled $C^{15}O$, which binds strongly to haemoglobin, and glucose metabolism using ^{18}F labelled deoxy-glucose. The isotopes used all have a relatively short half life (123s for ^{15}O up to 110 mins for ^{18}F). The disadvantages of the method are that it uses radioisotopes invasively and that due to their short half life, the isotope preparation is expensive, and must be performed nearby in a large cyclotron. The detection equipment is also bulky and cannot be used at the bedside, which is an important consideration when attempting to study preterm infants or patients requiring intensive care.

1.2.3 Ultrasound

This technique is similar in principle to radar, and involves transmitting high frequency (2.5 MHz - 10 MHz) sound waves into the body and detecting the reflected signal. Waves are reflected primarily at boundaries between organs with different acoustical impedance, but also inside most tissues due to small scale inhomogeneities. From the time taken for the wave to return, the position from which it has been reflected can be calculated[8]. Different tissue types can often be distinguished by the intensity of the signal reflected from them. The amplitude of the received signal must be corrected for the absorption and spread of the sound wave as it passes through the tissue, so that

the reflections from near the surface do not swamp those from deeper inside. Ultrasound can only be used to image the arrangement of different types of tissue, as it does not provide functional information.

1.2.3.1 Doppler ultrasound

Blood velocity can be measured with ultrasound by utilising the doppler effect. This effect causes the frequency F_o of a reflected wave to shift by an amount dF, proportional to the velocity, v of the reflector relative to the detector, given by

$$dF = 2F_o\frac{v}{c}\cos(\alpha) \qquad (1.1)$$

where α is the angle between the direction of movement and the detector and c is the velocity of the waves in the medium.

To get an average blood velocity distribution for all moving particles in the sound beam, a continuous source is used. To determine the velocity at one particular depth, a pulsed source is used, the depth being determined by the phase difference between input and detection. Blood flow can only be calculated using this method if the volume of the blood vessels, and the angle of the vessel to the ultrasound detector, are known, and remain constant throughout the measurement.

Both ultrasound and doppler ultrasound are non invasive, safe and can be used at the bedside.

1.2.4 Nuclear magnetic resonance (NMR)

When a nucleus with a magnetic moment (one with an odd number of protons and angular momentum) is placed in a magnetic field, B, it experiences a force which tends to turn it so that its magnetic moment is parallel to the applied field. Because the nuclei also have an angular momentum, due to their spin, the applied force causes them to precess about the magnetic field axis, rather like a gyroscope, with an angular frequency ω, given by the Larmor equation,

$$\omega = \gamma B$$
$$\text{where} \quad \gamma = \frac{q}{2\pi m} \tag{1.2}$$

q and m being the charge and mass of the proton respectively.

If an electromagnetic pulse of the same frequency as the Larmor frequency is applied to the nuclei, with its magnetic field component perpendicular to **B** there will be a strong interaction or resonance. This causes the orientation of the nuclei with respect to **B** to change by an amount which depends on the strength and duration of the pulse. Once the pulse has finished, the nuclei which continue rotating around the applied magnetic field now produce a small magnetic field component transverse to **B**. This rotating transverse field induces a current in a coil surrounding the sample, which is the signal detected by NMR. The time taken for the nuclei to return to their thermal equilibrium along **B** is known as T_1. Due to small scale inhomogeneities, individual nuclei have slightly different rotational frequencies; this results in their magnetic fields rotating relative to each other, and hence a reduction in the overall directional signal. The time for this to occur is known as T_2. The time constant of the decay of the induced signal in the coil, a combination of T_1 and T_2, is known as T_2^*. The nucleus most commonly used for imaging in tissue is that of hydrogen in water.

Several parameters can be measured in NMR, including T_1, T_2, T_2^*, nuclei density, and change in ω with chemical environment. In order to produce a 2D image of an object, additional magnetic fields are applied, which vary linearly along the axis, so that the applied rf pulse only interacts with the nuclei with the appropriate Larmor frequency, ie only those in a defined position along the axis. Different types of tissue can be distinguished using NMR, depending on their T_1 and T_2, which in turn depend on their molecular environment. Excellent structural images can be produced for soft tissues.

In order to enhance the contrast of specific tissues, eg tumours, a paramagnetic agent which has an affinity for them, such as Gd-DTPA may be employed. The paramagnetic Gd-DTPA causes large differences in T_1 and T_2 in adjacent nuclei. NMR has the disadvantage that it cannot be used at the bedside, as the equipment is very bulky and expensive. A good description of the physics and application of NMR imaging can be found in Westbrook and Kaut[9].

Chapter 2

Near infra red spectroscopy and imaging

2.1 Introduction

In this chapter, the use of near infra red spectroscopy to measure the relative oxygenation state of the blood will be described. Problems associated with the technique will be discussed, along with methods used to circumvent them.

The potential use of infra red light to produce images of human tissue is described in the last part of the chapter.

2.2 Near infra red spectroscopy

If a non scattering medium is illuminated with a collimated beam of light, the transmitted intensity, I is dependant upon the specific absorption coefficient α, the concentration of the absorber,C and the thickness ℓ of the medium. The exact relationship is given by the Beer Lambert law:

$$I = I_o \exp(-\alpha C \ell) \qquad (2.1)$$

where I_o is the incident intensity. Obviously, if the distance travelled through the medium and the specific absorption coefficient of the absorber are known, its concentration can be calculated.

In the situation where there is more than one absorber present, in order to calculate the concentration of each absorber, measurements must be made at different wavelengths. The minimum number of wavelengths needed is equal to the number of absorbers present, the wavelengths should be chosen to coincide with differences in the

absorption spectra of the absorbing compounds.

Using the technique for measuring across human tissue, a problem is caused by the high degree of light scattering. This has the effect that the light takes a convoluted path, and so the distance travelled is much longer than the distance between its entrance and exit points on the tissue surface.

In such a case, the pathlength is not only unknown, but does not have a singular value. It varies nonlinearly with source-detector distance and geometry, and is also dependent upon the absorption coefficient[10]. It is however, still possible to quantify *changes* in absorber concentration if we know, or can measure the relationship between the average photon pathlength, L and the source/detector distance,ℓ and assume that the absorption coefficient does not vary too much. The Beer Lambert law can be modified in such circumstances[11] to take scattering into account to give :

$$I = I_o e^{-(\alpha C \beta \ell)} + K \qquad (2.2)$$

where the differential pathlength factor, $\beta = L/\ell$, and K is a geometry and tissue dependant constant.

If only intensity changes are measured from some arbitrary starting point, assuming that K stays constant, this can be rewritten

$$\Delta I = I_o e^{-(\alpha \Delta C \beta \ell)} \qquad (2.3)$$

By measuring the average time <t> for an ultrashort pulse of light to cross the medium, (see Figure 2.1) the effective or average path length, L, can be determined[12,13] using $L = c\langle t \rangle$, c being the speed of light in the medium. This path length can be measured as a function of optode spacing, and an average conversion factor β determined.

Another method of measuring L is to use intensity modulated light, and to measure the phase angle ϕ between the transmitted and the detected modulated light (see Figure 2.2). Provided that the modulation frequency, f is less than 200 MHz, ϕ relates to the average pathlength by[14,75]

$$L \approx \frac{\phi c}{2\pi f} \qquad (2.4)$$

where ϕ is the phase difference. Using frequency modulation is equivalent to using the fourier transform of the time data, and since the temporal distribution is assymetric

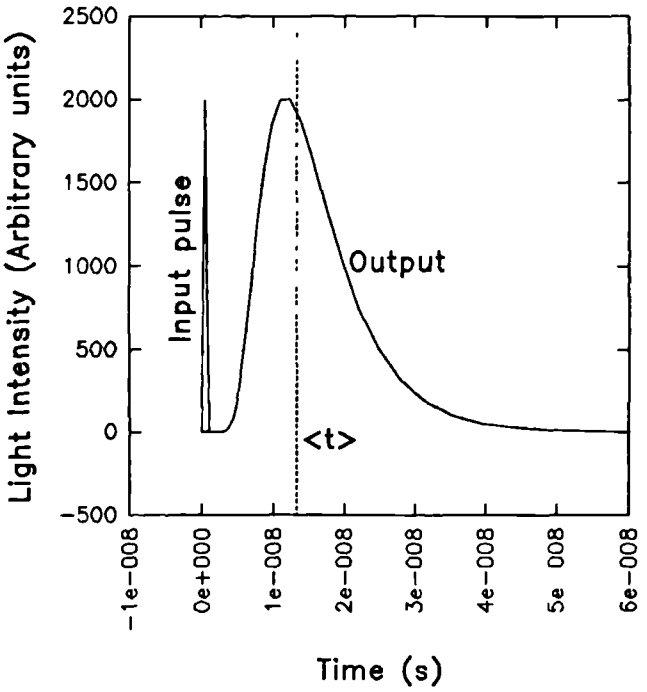

Figure 2.1 Light intensity vs time measured from a ultrashort pulse at time zero, showing the mean time of flight. Data generated using the diffusion equation.

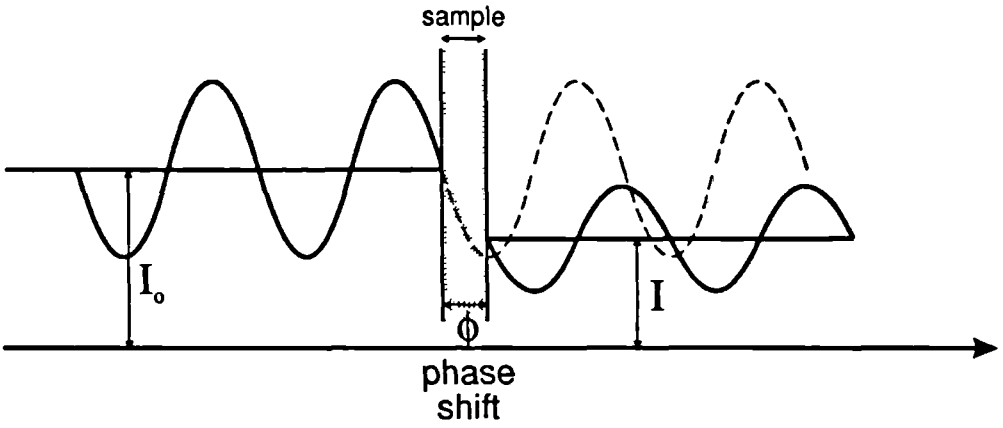

Figure 2.2 Input and output light distributions for an intensity modulated phase system

about its mean, for higher frequencies, the phase deviates from this relationship. This technique has the advantage that the equipment used to measure the pathlength is much less bulky than an ultrashort pulse laser system. This technique has been used by Sevick et al[15], Lakowicz et al[16] and Duncan et al[17].

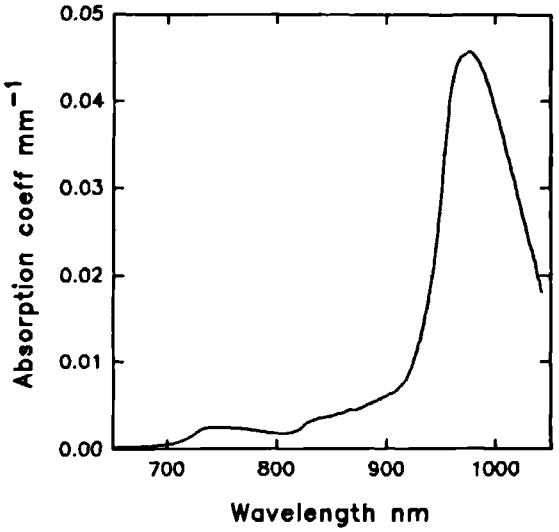

Figure 2.3 Absorption coefficient of water in range 650 to 1025 nm.

Work is also being carried out into the determination of the path length using the absorption of light by water in the tissue[18]. The concentration of water in the body is known fairly accurately, and water has some absorption bands in the near infra red region (see Figure 2.3). If, therefore, the light attenuation through tissue at these wavelengths is measured, and compared with the expected absorption, the actual pathlength travelled by the light through the tissue can be calculated via Eqn (2.2), providing that the concentration of water is known.

Tissue spectrometers using a range of these techniques have been designed to determine relative changes in tissue oxygenation, using previously measured spectra for pure oxygenated and deoxygenated haemoglobin and cytochrome aa_3.[49,19,20,21]

2.3 Imaging with infra red.

2.3.1 Simple imaging

The first attempt at imaging breast tissue using visible light was made by Cutler[22] who used a light beam to illuminate the breast, viewing the resultant shadows in a darkened room. He observed that malignant tumours caused a darkened shadow. Ohlsson et al [23] used infra red light and infra red sensitive photographic film to the same end, and, more recently, television cameras have been used, allowing instant display of images. The technique can distinguish between cystic and solid tumours (when large), but clinical trials have shown that the sensitivity of the technique is

inadequate when compared to mammography, especially for small and deep lesions[24,25,26]. In order to improve the technique, it is necessary to reduce the amount of scattered light detected, or to use some knowledge of light transport in tissue to try to correct for the blurring effects of scattering.

2.3 2 In line measurements

In these measurements, the source and detector are both collimated, and in line with each other. This is in an attempt to reduce the effects of scattered light by measuring only those photons which leave the sample travelling on the their initial axis (Figure 2.4). This procedure does not, however, eliminate all of the scattered photons, as it is quite possible for a photon to be multiply scattered back onto its original path. An image is obtained by linear scanning of the source / detector over the object. This technique has been tried by Jarry et al[27], Araki et al[28], and He et al[29] who compared the technique favourably to X ray mammography.

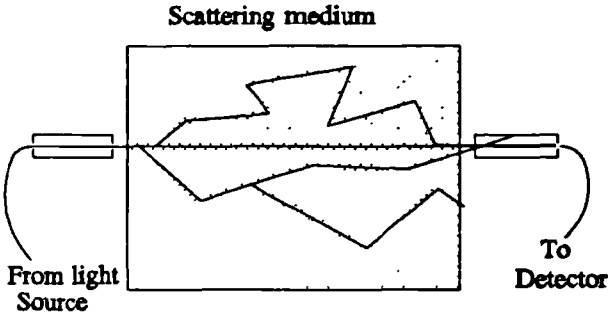

Figure 2.4 In line measurements

2.3 3 Time gated backprojection

This involves the same principle as the in line measurements, but to further reduce the number of photons which have undergone multiple scattering, the sample is illuminated by ultra short pulses of light, and the intensity in the first 10-100ps is measured. Photons which arrive in this time period cannot have deviated too far from the straight through path. Hebden[30] considered the possible deviation r_{max} from the

straight through path, and derived an expression for the resolution, Δx as a function of the time gating Δt:

$$r_{max} = \frac{(c\Delta t+d)}{2}\sqrt{1-t^2/(c\Delta t+d)^2} \qquad (2.5)$$

$$\Delta x \approx 1/2r_{max}$$

where c is the speed of light in the medium, and d the thickness of the medium. This expression is only valid when r_{max} is less than the width of the medium, for larger values, it tends to overestimate the resolution

This process is identical to that used in X ray tomography[31] and has been used by several investigators[32,33,34,35,36,37]. The advantage of this technique is its simple concept, but it has the obvious disadvantage that the measured light intensity is much reduced and falls exponentially with sample thickness, thus reducing the signal to noise ratio.

A development of the technique has been used by Hebden[38] who measured the whole temporal distribution of light (over ~2000 ps), and fitted the data to a temporal distribution calculate using the diffusion equation. The diffusion equation fit was then used to predict the integrated intensity over the first few picoseconds. Improved resolution is obtained with this method.

2.3 4 General inverse technique

This is a general mathematical technique for comparing the measured intensity with a mathematical model. For any given geometry and source, we can define a forward operator, **F**, which gives some measurable quantity λ as a function of the positionally varying optical properties of the medium, μ_a and μ_s, given by

$$F(\mu) = \lambda \,. \qquad (2.6)$$

Considering a small change in the optical properties of μ to $\mu + \delta$ we can further define the derivative forward operator **A** such that

$$A(\delta) = F(\mu+\delta)-F(\mu) \ . \tag{2.7}$$

In order to determine the optical image, μ from the measurements, the Moore Penrose inverse can be used iteratively,[39]

$$\mu^{(k+1)} = [(A^{*}A)^{-1}A^{*}][\lambda - F(\mu^{(k)})] + \mu^{(k)} \tag{2.8}$$

where k indicates the iteration number, and * indicates an adjoint operator, ie **F*F** = μ. Only the first iteration can be obtained using exact solutions of the diffusion equation, as this is only soluble for the homogeneous case. However, some more flexible model such as the finite elements solution[81] of the diffusion equation, or the random walk model[85,86] could be used to give further iterations. The quantities which can be measured and used as data for this method of reconstruction include the integrated intensity as a function of position,$I(\xi)$:

$$I(\xi)=\int_0^{\infty} I(\xi,t)dt \ , \tag{2.9}$$

<t>, the mean of the temporal distribution (see (1.31))

$$\langle t\rangle(\xi) = \frac{\int_0^{\infty} tI(\xi,t)dt}{\int_0^{\infty} I(\xi,t)dt} \ , \tag{2.10}$$

or, if amplitude modulated light is used, the phase shift and modulation depth, M (see Figure 2.2)

$$M = \frac{(I_{ac} \ / \ I_{dc})_{detected}}{(I_{ac} \ / \ I_{dc})_{incident}} \ . \tag{2.11}$$

Chapter 3

Absorption and scattering of light

3.1 Introduction

In this chapter, the theory of light absorption will be discussed, together with the causes of light absorption in tissue. Models of light scattering will then be presented, along with a brief discussion of the causes of light scattering in tissue.

3.2 Absorption

Bouger[40,41] in 1729 derived the first relationship between the thickness of a material and its absorption of light. Lambert[42] later expressed Bouger's relationship mathematically. The Lambert-Bouger law, as it is often known, states that for a pure absorber, a layer of thickness $d\ell$ absorbs a fraction dI/I of the incident light intensity I, ie that $dI/I = \mu_a d\ell$ where μ_a is a constant for the material, called the absorption coefficient.

The collimated light I measured when a collimated light beam of intensity I_o passes through ℓ mm of non scattering material is therefore

$$I = I_o e^{-\mu_a \ell} . \qquad (3.1)$$

This equation can also be expressed in terms of the complex refractive index of the material (n) and the wavelength λ:

$$I = I_o \exp\left(\frac{-4\pi n \ell}{\lambda}\right) \qquad (3.2)$$

Beer[43] in 1852 derived a similar relationship for absorption in terms of the concentration of absorbing molecules in a medium. This states that the absorption coefficient is proportional to the concentration of the absorber. Combining the two laws, we obtain the so called Beer-Lambert law, which states that

$$I = I_o e^{-\alpha C \ell} \qquad (3.3)$$

where C is the concentration of the absorber and α the absorption coefficient per unit concentration ie the specific absorption coefficient, usually quoted in units of mm^{-1} $mmol^{-1}$. This equation can be rearranged as

$$\log_{10}(e).\alpha C \ell \equiv \varepsilon C \ell \equiv A = \log_{10}\left(\frac{I_o}{I}\right) \qquad (3.4)$$

where A is the absorbance or the optical density, and ε is the base 10 absorption coefficient, often called the specific extinction coefficient, and usually quoted in units of cm^{-1} $mmol^{-1}$. In this thesis, base e coefficients will be used in general, although both are widely used in the literature. For a solution containing a mixture of absorbing substances, the absorption coefficients sum, so the optical density is simply given by

$$A = (\varepsilon_1 C_1 + \varepsilon_2 C_2 + ... + \varepsilon_n C_n)\ell \ . \qquad (3.5)$$

3.2.1 Absorbing chromophores in vivo

3.2.1.1 Water

The largest component of tissue is water. The average water content of adult brain is 80%, that of skeletal muscle 74%, and of adipose tissue, which is the main component of the female breast, 21%[44]. This means that any absorption bands of water will have a large effect on light transmission. The absorption coefficient of pure water has been measured[45] and is reproduced in Figure 3.1 for the wavelength range 0.2 μm

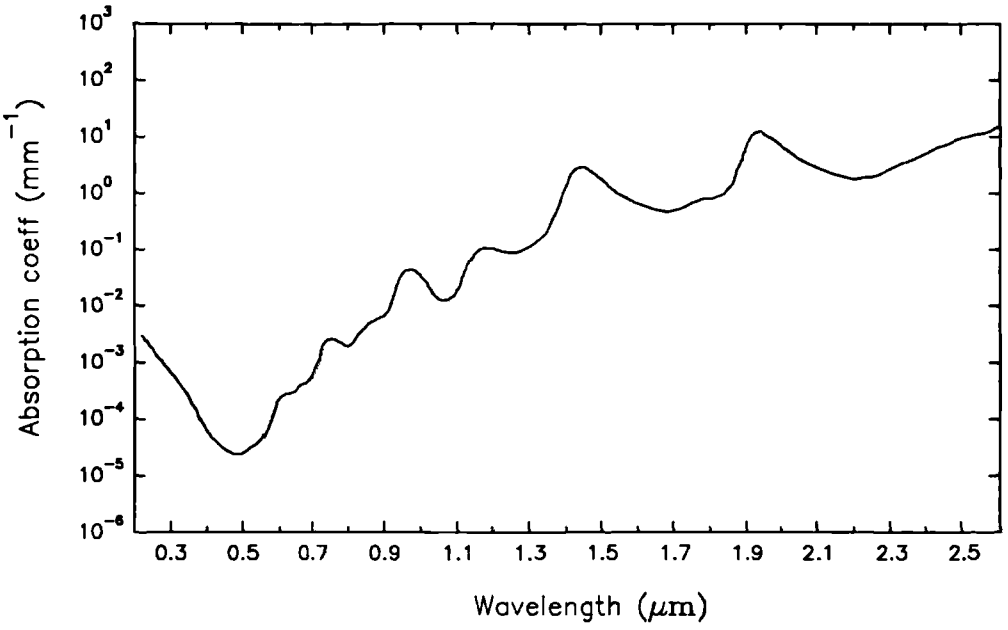

Figure 3.1 The absorption coefficient of water in the range 0.2 - 2.6 μm.

to 2 μm. As can be seen, at wavelengths longer than 1.3 μm the absorption coefficient is greater than 0.1 mm^{-1}. Such a high level of absorption makes light detection through more than one or two centimetres of tissue very difficult, limiting transmission measurements to shorter wavelengths.

3.2.1.2 Lipids

Little data is available on the absorption spectra of human lipids, but the extinction coefficient of pork fat has been measured by Conway et al[46] and the spectrum is shown below. As can be seen, it is similar in many ways to that of water. In the adult brain, the grey matter contains 8% of lipid by mass, and white matter 17%[47]. Lipids will therefore not contribute significantly to the overall extinction in the 600-900 nm region where the intrinsic absorption is low.

The percentage of lipid in adipose tissue, of which the breast is largely composed, is approximately 75%, which means that there, the lipid absorption must be taken into account.

The percentage of lipid in skeletal muscle is approximately 4% in normal

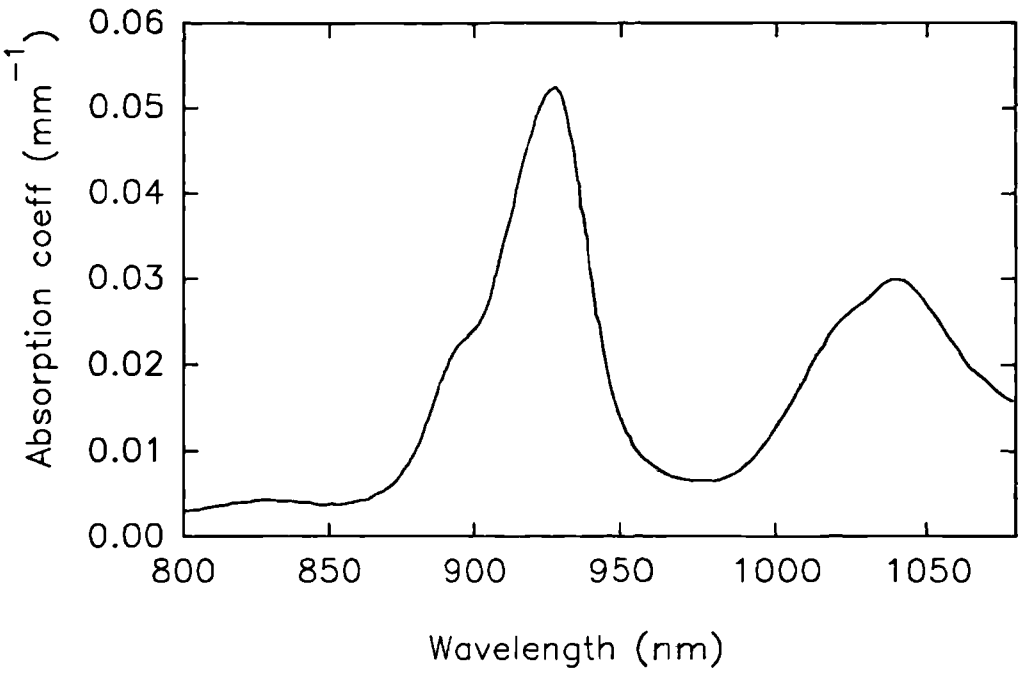

Figure 3.2 The absorption spectra of pork fat in the range 800-1100 nm.

adults[44], although certain clinical diseases can lead to muscle wastage and fat deposition (eg muscular dystrophy).

There is also a contribution to all measurements of light transmission from absorption by subcutaneous adipose tissue, which will vary from individual to individual, but will tend to be larger in women.

3.2.1.3 Haemoglobin

Haemoglobin is found in the red blood cells and is the major oxygen carrying compound in the blood. There are several different forms of haemoglobin which can be found naturally in the blood, the most common are oxygenated and deoxygenated haemoglobin (HbO_2 and Hb). Also found are carboxyhaemoglobin (HbCO), typically present at 2-4%, but up to 10% in smokers[48], haemiglobin (Hi), typically 0.5 - 2.5%, and sulphaemoglobin (SHb), which does not occur in normal blood, but does occur in patients with certain hereditary disease, after the ingestion of certain nitrogen compounds, or in patients taking certain drugs such as sulphonamides. The spectra of these compounds are shown below[49]. Since the concentration of blood in the brain is

approximately 84μM[49], it is apparent that light absorption by haemoglobin will limit the wavelength of light used for spectroscopy across several centimetres of tissue to wavelengths above 600 nm.

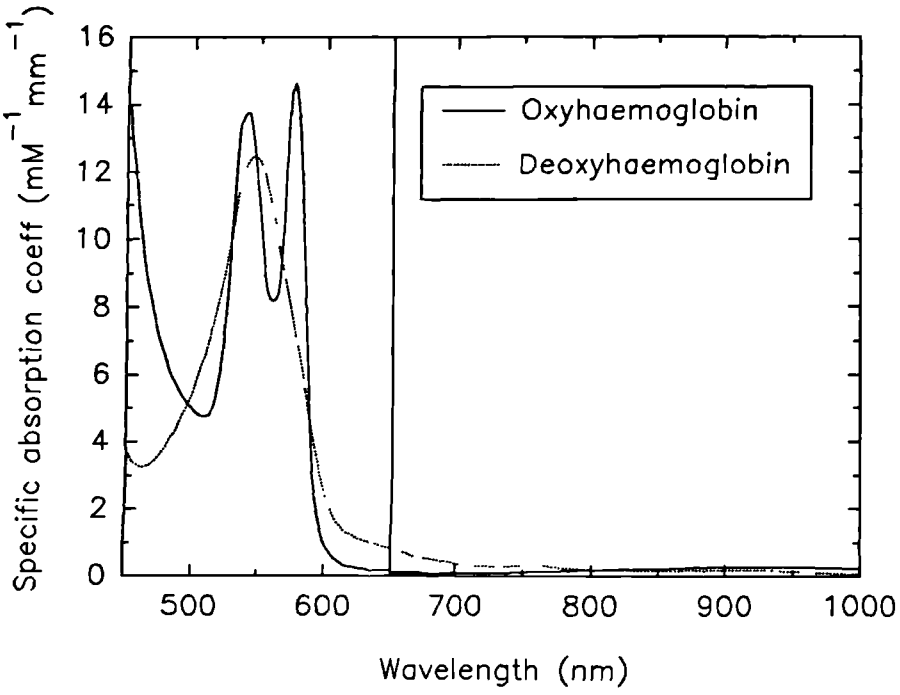

Figure 3.3 The absorption spectra of Haemoglobin in both oxygenated and deoxygenated states in the range 450 to 1000 nm.

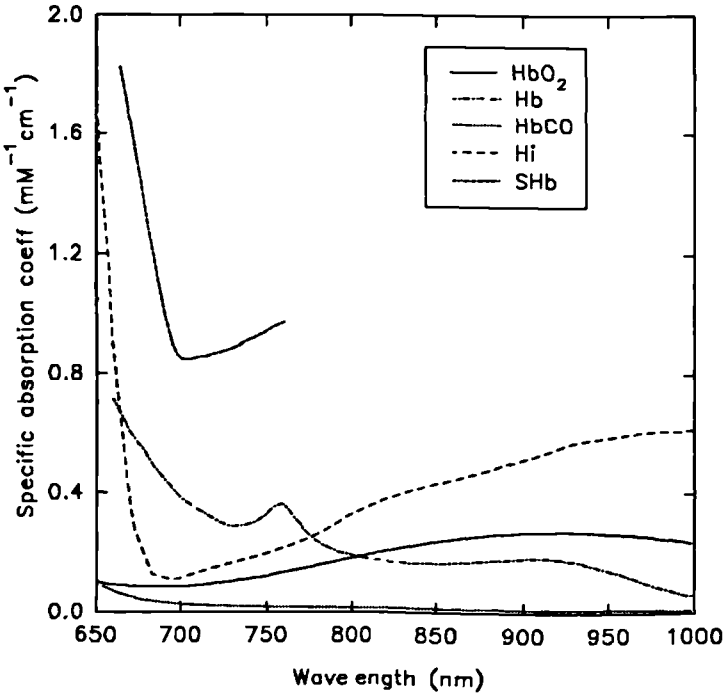

Figure 3.4 The absorption spectra of several haem compounds in the near infra red between 650 and 1000 nm.

3.2.1.4 Myoglobin

Muscle contains the chromophore myoglobin. Its NIR absorption spectra is almost identical to that of haemoglobin[50] although the spectra are different in the UV and visible region. The binding of oxygen to myoglobin occurs at lower partial pressures than haemoglobin ($P_{50} \approx 1$ kPa cf $P_{50} \approx 3.5$ kPa for Hb). This means that in general, in well perfused tissues, most of the myoglobin is fully oxygenated.

3.2.1.5 Cytochromes

The cytochrome chain of enzymes are responsible for electron transport in the mitochondria where oxygen is reduced to form water, and ADP phosphorylated to form ATP. Cytochrome aa_3 is the terminal enzyme in the chain, and has the strongest absorption coefficient. The absorption spectra of the cytochrome enzymes[49] are given in Figure 3.5

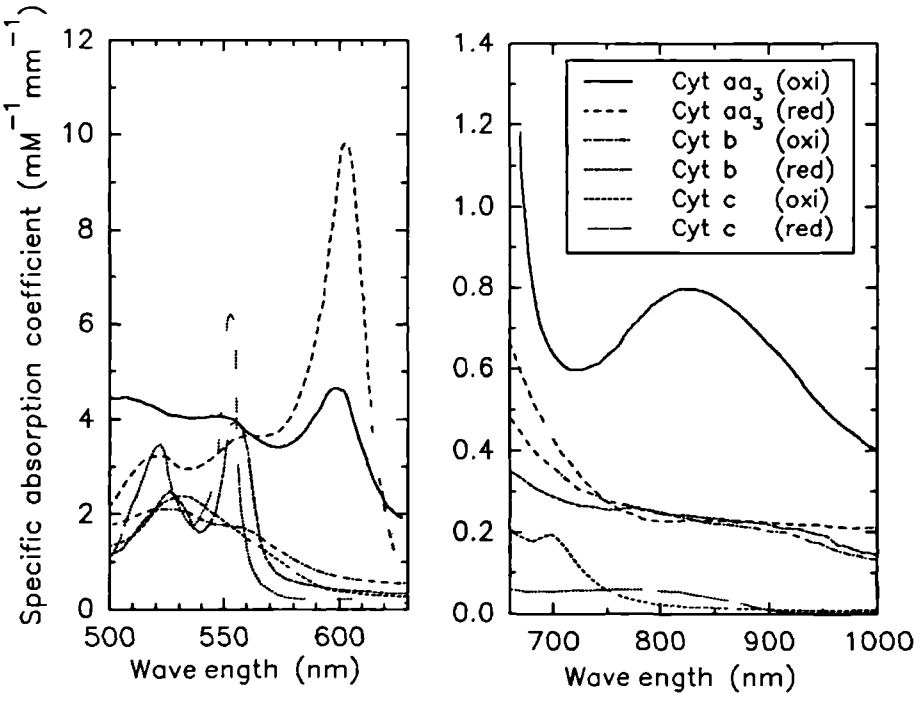

Figure 3.5 The absorption spectra of the cytochrome enzymes in the range 500-1000nm.

3.3 Scattering

Tissue scatters near infra red light elastically, which means that the wavelength of the light remains constant. The scattering of light is dependent on two quantities: the relative refractive index of the scatterer and its surrounding medium, and the dimensions of the scattering particle relative to the wavelength of the light. The percentage of scattered light and its angular distribution depends greatly upon the ratio of particle size to wavelength. The size of the scatterers in tissue cover the range from somewhat larger to smaller than the wavelength of near infra red light.

The scattering coefficient of a substance, μ_s is defined in much the same way as the absorption coefficient, ie

$$I_u = I_o e^{(-\mu_s l)} \tag{3.6}$$

where I_u is the unscattered light intensity at depth ℓ.

Two other parameters which can be defined are the scattering and extinction cross-sections, σ_s and σ_a respectively.

$$\sigma_s = \frac{W_s}{I_o} \qquad \sigma_a = \frac{W_a}{I_o} \tag{3.7}$$

where I_o is the total intensity incident on the particle, W_a the rate of energy absorption by the particle, and W_s the rate of energy scattering by the particle. The scattering coefficient is related to σ_s by

$$\mu_s = \frac{\sigma_s}{d^3} \tag{3.8}$$

where d is the average distance between particles.

3.3.1 Angular distribution of scattered light

The angular distribution of the scattered light is known as the scattering phase function, $f(\theta)$. From it can be obtained the mean cosine of the scattered intensity, g

$$g = \frac{\sum f(\theta)\cos\theta\sin\theta}{\sum f(\theta)\sin\theta} \qquad (3.9)$$

which is used in diffusion theory as a measure of the anisotropy of the scattering (see chapter 4.1.2). g varies from 1 (totally forward scattered light) to 0 (isotropically scattered light.

The transport scattering coefficient is defined as $\mu_s' = \mu_s(1-g)$. $1/(1-g)$ is the number of scattering events which occur before the directionality of the scattering becomes randomised. This means that in the far field, the light distribution in a scattering medium with an anisotropy factor of g and a scattering coefficient of μ_s is equivalent to that in an isotropic scattering medium with a scattering coefficient of $\mu_s(1-g)$.

The Henyey Greenstein function[51,52] is often used to approximate the angular dependence of scatter, f as a function of the cosine of scatter, u. It involves only the parameter g, and the ratio of reflected to incident light, or albedo, ω_o :

$$f(u) = \omega_0(1-g^2)(1+g^2-2gu)^{-3/2} \qquad (3.10)$$

This function gives a reasonably good approximation to the exact predictions of Mie theory (see next section), and has the advantage of being an easy expression to handle mathematically.

3.3.2 Mie theory of single scattering by spherical particles

The exact theory of the scattering of light by a solid sphere was developed by Gustav Mie in 1908[53]. He calculated the internal and external scattered electromagnetic fields as a function of the size parameter, x and the relative refractive index, m:

$$x = \frac{2\pi na}{\lambda} \quad ; \quad m = \frac{n_1}{n} \qquad (3.11)$$

where n and n_1 are the complex refractive indices of the medium and particle respectively, and a is the radius of the scattering particle. The solutions involve infinite series of Bessel and modified Bessel functions; for an incident wave of wavenumber k

travelling in the x direction,

$$E_i = E_o e^{ikr\cos\theta}\hat{e}_x \tag{3.12}$$

the electric and magnetic fields of the scattered wave are given by

$$\begin{aligned} E_s &= \sum_{n=1}^{\infty} E_n(ia_n N_{eln} - b_n M_{oln}) \\ H_s &= \frac{k}{\omega p}\sum_{n=1}^{\infty} E_n(ib_n N_{oln} + a_n M_{eln}) \end{aligned} \tag{3.13}$$

where

$$\begin{aligned} M_{on} &= \cos\phi\,\pi_n(\cos\theta)h_n^{(1)}(kr)\hat{e}_\theta - \sin\phi\,\tau_n(\cos\theta)h_n^{(1)}(kr)\hat{e}_\phi \\ M_{en} &= -\sin\phi\,\pi_n(\cos\theta)h_n^{(1)}(kr)\hat{e}_\theta - \cos\phi\,\tau_n(\cos\theta)h_n^{(1)}(kr)\hat{e}_\phi \\ N_{on} &= \sin\phi\, n(n+1)\sin\theta\,\pi_n(\cos\theta)\frac{h_n^{(1)}(kr)}{kr}\hat{e}_r \\ &\quad + \sin\phi\,\tau_n(\cos\theta)\frac{\left[kr\,h_n^{(1)}(kr)\right]'}{kr}\hat{e}_\theta + \cos\phi\,\pi_n(\cos\theta)\frac{\left[kr\,h_n^{(1)}(kr)\right]'}{kr}\hat{e}_\phi \\ N_{en} &= \cos\phi\, n(n+1)\sin\theta\,\pi_n(\cos\theta)\frac{h_n^{(1)}(kr)}{kr}\hat{e}_r \\ &\quad + \cos\phi\,\tau_n(\cos\theta)\frac{\left[kr\,h_n^{(1)}(kr)\right]'}{kr}\hat{e}_\theta - \sin\phi\,\pi_n(\cos\theta)\frac{\left[kr\,h_n^{(1)}(kr)\right]'}{kr}\hat{e}_\phi \end{aligned} \tag{3.14}$$

(e and o designate even and odd)

$$\begin{aligned} a_n &= \frac{pm^2 j_n(mx)[xj_n(x)]' - p_1 j_n(x)[mxj_n(mx)]'}{pm^2 j_n(mx)[xh_n^{(1)}(x)]' - p_1 h_n^{(1)}(x)[mxj_n(mx)]'} \\ b_n &= \frac{p_1 j_n(mx)[xj_n(x)]' - pj_n(x)[mxj_n(mx)]'}{p_1 j_n(mx)[xh_n^{(1)}(x)]' - ph_n^{(1)}(x)[mxj_n(mx)]'} \end{aligned} \tag{3.15}$$

and

$$E_n = i^n E_o \frac{(2n+1)}{n(n+1)}$$
$$\pi_n = \frac{P_n^1}{\sin\theta} \qquad (3.16)$$
$$\tau_n = \frac{dP_n^1}{d\theta} .$$

θ and ϕ are the planar and azimuthal spherical polar angles, p and p_1 are the permeability of the medium and sphere respectively, $h_n^{(1)}$ is a spherical Bessel function of the third kind, j_n a spherical Bessel function, and P_n^1 a Legendre Polynomial.

From these equations can be calculated the rate of energy scatter, W_s

$$W_s = \frac{1}{2} Re \int_0^{2\pi} \int_0^{\pi} (E_{s\theta} H_{s\phi}^* - E_{s\phi} H_{s\theta}^*) r^2 \sin\theta \, d\theta \, d\phi \qquad (3.17)$$

and using equation (3.7), σ_s can be calculated.

$$\sigma_s = \frac{2\pi}{k^2} \sum_{n=1}^{\infty} (2n+1) Re[a_n + b_n] \qquad (3.18)$$

Not surprisingly, solutions to these equations are normally calculated numerically using a computer, although the equations used for this are slightly modified for ease of calculation and convergence, the speed of convergence being faster the smaller the particle. From the scattered fields can be calculated the scattering and extinction cross sections and the angular dependence of scatter. The angular scatter function for particles of size greater or equal to the wavelength is highly forward weighted. Figure 3.6 shows the angular distribution of scattered light for particles which are 0.1,1 and 10 times the size of the

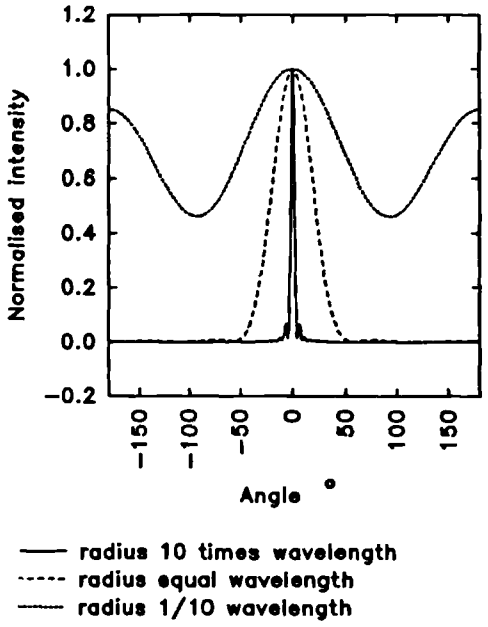

Figure 3.6 Showing the variation of scattered light intensity with particle size.

incident light wavelength (zero represents the forward direction).

Mie theory has also been applied to other simple geometries, including elliptical particles and hollow spheres, but is not strictly valid for particles of arbitrary geometry. It is, however, the only accurate theory which applies to particles of size comparable with the wavelength. A full derivation of the Mie equations for a spherical particle and a FORTRAN algorithm to evaluate them is given in Bohren and Huffman[54].

When the particle size is less than 1/4 of the wavelength the theory simplifies, and Rayleigh scattering theory applies.

3.3.3 Rayleigh theory of light scattering

Rayleigh's theory concerns the scattering of light by particles much smaller than the wavelength. He derived it by considering the dimensions of the variables involved, these being the volume V of the particle, the distance r at which observations are made, and the wavelength λ of the light. His equation states that the scattered intensity, I_s, is given by

$$I_s \propto \frac{V^2}{r^2\lambda^4} \tag{3.19}$$

A similar equation can be derived from Mie theory by taking the first few terms of the Bessel series expansion. For unpolarized incident light I, the scattered light I_s at angle θ is

$$I_s = \frac{8\pi^4\, n\, a^6}{\lambda^4 r^2}\left(\frac{m^2-1}{m^2+2}\right)^2 (1+\cos^2\theta)\, I_i \,. \tag{3.20}$$

The angular dependence of scatter is thus a sinusoidally varying function, and as the radius of the particle, *a*, tends to zero, the distribution becomes isotropic.

3.3.4 Variation of scattering with wavelength

There are two causes of the variation of scattering with wavelength. The first

is the changing ratio of particle size to the wavelength of the light. The scattering cross section is highly dependant on this ratio, especially when the particle is approximately the same size as the wavelength. For particles much smaller than the wavelength of the light, the cross section is inversely proportional to the fourth power of the wavelength. This was shown in the section on Rayleigh scattering, and incidentally, is responsible for the blueness of the sky and redness of sunsets[116]. For particles much larger than the wavelength, the scattering cross-section is approximately constant (See Figure 3.7). The anisotropy of the scattering also changes with wavelength, becoming more forward biased as the wavelength gets shorter.

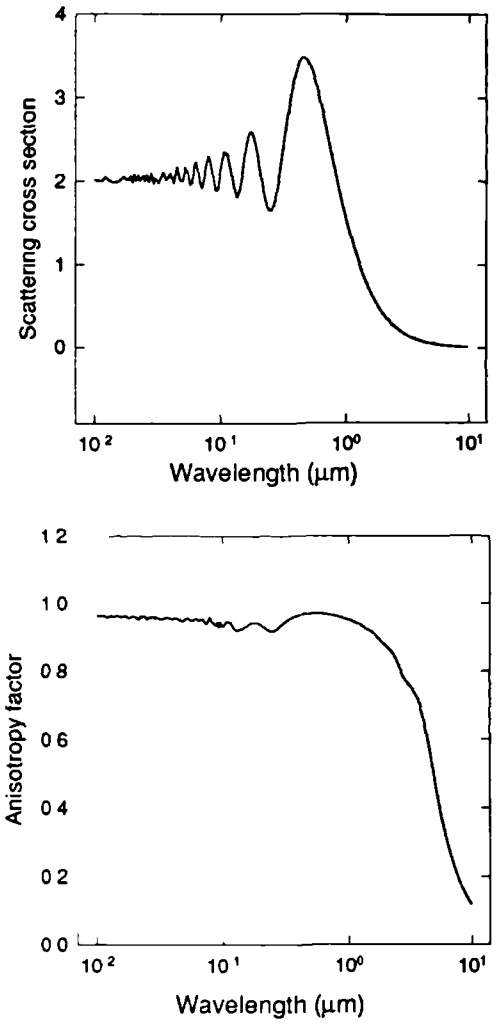

Figure 3.7 Showing the variation of scattering cross section and g factor with wavelength for a particle of diameter 1μm.

The refractive index of the scattering particles and medium will also vary with wavelength, and this is the other cause of variation in the scattering cross section. The refractive index slowly decreases with wavelength for transparent materials, and this decrease can be approximated by using an approximation discovered by Cauchy[55]

$$n = A + \frac{B}{\lambda^2} + \frac{C}{\lambda^4} + \ldots \qquad (3.21)$$

where λ is the wavelength and A, B etc are constants for the particular material. The effect of this variation will differ, depending upon the individual refractive indices of scattering particle and medium.

3.3.5 Causes of scatter in vivo

Variations in refractive index are responsible for light scattering. In tissue this is due to two effects. The first is changes in overall refractive index at the boundaries between one type of tissue and another, analogous to scattering of ultrasound in tissue by the change in density. The other cause is small scale variations in refractive index within cells, and between cells and the extracellular fluid. The problem of scattering by tissue is a complex one, due to the intricate structure of the cells. Cope[49] examined this problem and came to the conclusion that in brain, the main scatterers were mitochondria, which act as Mie scatterers, and the cell membrane, which acts rather like a dielectric film. The effects of light scattering by red blood cells is small because of the generally low concentration of blood in tissues (typically 3% by volume, of which approximately half is red cells). For the modelling of light transport, it does not matter so much what the exact causes of scatter are, so long as their effect can be determined.

Chapter 4

Light propagation in tissue

4.1 Models of light propagation in tissue

In order to use light therapeutically or diagnostically, it is imperative to know how it propagates through tissue, so that the degree of illumination as a function of position is known. Several methods of doing this have been developed, with varying degrees of complexity, the more important of which are described in this chapter.

Theories of light propagation through tissue usually involve treating the light as being particulate, rather than wavelike in nature. Twersky[56] developed a theory of light transport using EM theory, but this approach is little used, being both complex and difficult to apply to anything other than simple homogeneous geometries. In addition, due to the random nature of tissue, wave effects and interference rapidly average out and become negligible.

4.1.1 Discrete ordinates or Kubelka Munk theory

The discrete ordinates method involves transforming the continuous direction variable Ω, into N discrete values, so that

$$\int_{4\pi} d\Omega I(r,\Omega) \rightarrow \sum_{n=1}^{N} w_n I_n(r) \qquad (4.1)$$

where w_n are the weighting factors for the numerical integration. This has also been called the N flux method.

Kubelka Munk theory is basically a two flux model, having a forward and backward diffuse flux in a infinite slab. It assumes isotropic irradiance and zero reflection at the boundaries of the sample[57,58]. Using this theory, the 'Kubelka Munk' scattering and absorption coefficients can be directly related to the measured diffuse reflection and transmission. However, the coefficients measured this way are not directly equivalent to μ_s and μ_a and several conversion formulae have been derived for them (see Cheong et al [79]). Also, the assumptions made in Kubelka Munk theory are usually far from realistic, resulting in an inadequate model. Assorted modifications of the theory have been made, to incorporate collimated beam irradiance, anisotropic scatter and specular reflection at the sample boundaries[59,60]. Other models based on the discrete ordinates method have been suggested, with N of 3 (van Gemert et al[61]) and 7 (Welch et al[62]).

4.1.2 The radiative transfer equation

The transfer equation has been extensively used for modelling neutron diffusion in reactors[63] and atmospheric light transport[64,65,66]. In this theory, light is assumed to diffuse randomly through the medium. A derivation of the radiative transfer equation is given in several texts, eg Case et al[63], Chandrasekhar[64], and Duderstadt et al[67]. For a source, **q**, the photon density, Φ at position **r**, in direction $\hat{\mathbf{s}}$, is given by

$$\hat{s}.\nabla\Phi(r,\hat{s}) + (\mu_a+\mu_s)\Phi(r,\hat{s}) = \left(\frac{1}{c}\right)\hat{s}.q(r) + \mu_s\int_\Omega \sigma(\hat{s},\hat{s}')\Phi(r,\hat{s}')\,d\Omega \qquad (4.2)$$

where c is the speed of light in the medium, and σ is the probability of scattering from direction $\mathbf{s}'$ to direction **s**. The terms on the left hand side are, respectively, the gradient of the intensity and the light lost from direction **s**. The terms on the right hand side are, the source distribution, and the light scattered into direction **s** from all other directions.

Unfortunately, this equation is too complex to be solved analytically except for very simple geometries, eg the infinite homogeneous case. Some simplifications can be made however, which allow solutions to be derived for more realistic cases. If the assumption is made that σ is not spatially variant, and that it is a function of the cosine of the angle of scattering only, then equation (4.2) can be expanded into spherical

harmonics [63,68 69.] to yield the light intensity,

$$\Phi(r,\hat{s}) = \sum_{n=0}^{\infty}\sum_{m=-n}^{n}\left(\frac{(2n+1)}{4\pi}\right)^{1/2}\Phi_{n,m}(r)Y_{n,m}(\hat{s}) \qquad (4.3)$$

where the Y are the spherical harmonics. The summation may be truncated after N terms if subsequent derivatives of ϕ vanish. This produces $(N+1)^2$ coupled partial differential equations, known as the P_N approximation. The most common approximation is the P_1, or the diffusion approximation, which, under the assumption that the source, q_o is isotropic, can be reduced to one equation[63]

$$\left[\nabla.D(r)\nabla-\mu_a(r)c\right]\Phi(r) = q_o(r) \qquad (4.4)$$

where D(r), the diffusion coefficient is given by

$$D(r) = \frac{c}{3(\mu_a(r)+(1-g)\mu_s(r))} \qquad (4.5)$$

where g is the mean cosine of the scattering phase function. This approximation has been used by several workers[70,71,72,73,74] and can be solved analytically for simple geometries such as a point source in an infinite medium[75,76]. In order to obtain a boundary condition of zero intensity on the boundary of finite media, a common solution is to use the method of images, with a positive and negative source about the boundary[77,78].

One advantage of the diffusion approximation is its simple conversion to a time dependent equation[75] :

$$\left(\nabla.D\nabla-\mu_a c-\frac{d}{dt}\right)\Phi(r,t) = q_o(r,t) \qquad (4.6)$$

The diffusion approximation is only strictly valid for cases where $\mu_s' = \mu_s(1-g) >> \mu_a$ and for situations where all dimensions are larger than a transport mean free path. However, these conditions are mostly met in tissue, especially in the NIR, where μ_s' is in general at least an order of magnitude greater than μ_a, and the mean free path approximately 0.1 mm[79].

The P_3 approximation has been investigated by Star[80], who compared it with both the P_1 approximation and a Monte Carlo model (see section 4.1.4). It showed a greater level of agreement with results from the Monte Carlo than the P1 approximation,

especially near boundaries. However, it has not been much used, since the improvements it brings are only significant near the surface, and because of the increased computation time required to solve the six equations involved.

4.1.2.1 Finite elements method

This is a technique by which analytical equations can be applied to situations of arbitrary geometry. It has been used for light transport problems to analyse the diffusion approximation to the transport equation. Basically, the method involves dividing the area under investigation into a large number of elements, and finding a solution to the P_1 approximation, which holds for all elements individually. This approach has been taken by Arridge et al[81] who have shown that results from FEM modelling show a high degree of agreement with the predictions of Monte Carlo models and that for simple geometries, the model agrees with the analytical solutions of the diffusion equation. It has the advantage of being fast, and applicable to any geometry. The technique has also been used by Suddeath et al[82], and Yamada et al[83]. It has the same restrictions on its applicability as the P_1 approximation, ie that $\mu_a << \mu_s'$. It is, in principle, possible to use any of the P_N approximations to improve the model, although this results in increasing the complexity of finding a solution.

4.1.3 Random walk model

In this model, the region is divided into unit cubes, or 'voxels', and photons can either move into an adjacent voxel or be absorbed; the probability of absorption being dependent on the absorption coefficient. This method was first applied to tissue optics by Bonner[84] who assumed that movement in any direction was equally likely : a true lattice random walk, equivalent to isotropic scatter. In order to calculate the surface fluence rate, he calculated the probability of a photon exiting, having taken a particular path, and summed over all possible paths. A similar approach has been taken by Grünbaum et al[85] who assigned different probabilities to movement forwards, backwards, and sideways, and used a set of linear equations to solve the problem. This

model has since been used by Schlereth[86] who used a random number generator to produce paths through the medium in a fashion akin to Monte Carlo methods.

Chandrasekar[87] in 1943 examined random walks, and derived expressions for the probability of finding the 'walker' at position **r** after N steps. For small N, the theory is complex, but a simple approximation can be made where $N >> r/\ell$, ℓ being the step size. This approximation is equivalent to the diffusion theory solution.

4.1.4 Monte Carlo simulations

Monte Carlo simulations treat light as a collection of discrete particles, with a probability of travelling a distance ℓ without scattering of $\exp(\mu_s \ell)$ and a probability of travelling a distance ℓ before absorption of $\exp(\mu_a \ell)$. The probability of scattering occurring between ℓ and $\ell + d\ell$ is given by :

$$P[\ell\ ]d\ell = \mu_s e^{(-\mu_t \ell)} . \qquad (4.7)$$

The method involves generating a series of random numbers, R to determine the scattering length between interactions and the angle of scatter. The scattering length ℓ_s is determined using

$$\ell_s = -\frac{\ln(R)}{\mu_s} . \qquad (4.8)$$

The probability of scattering in a particular angle is either defined by a function such as isotropic scattering or the Henyey Greenstein function, or by an empirical phase function stored in a probability versus angle table. In calculating the amount of absorption, to make the process computationally efficient, the photon is assigned an initial intensity, which is reduced according to $\exp(-\mu_a \ell)$. Individual photons are followed through the medium, until either their intensity drops below a predefined limit, or they leave the medium. A good description of the theory of Monte Carlo modelling for light transport is given by Essenpreis et al[88].

Although Monte Carlo modelling is physically realistic, and can be used for media of arbitrarily complex geometries, in order to produce data with adequate statistics for even small simulations (<2 cm diameter), a large number ($\geq 10^6$) of photons must

be followed through the media, and this involves extensive computing time ($\geq 10^5$ seconds). The time required increases exponentially with the size of the situation being modelled.

The model is generally regarded as being the most realistic, and has been used by a large number of investigators in the field including Donnelli et al[89], Flock et al[90] Haselgrove et al [74], Jacques[91], Key et al[92], Peters et al[93], van der Zee[94] and Hiraoka[95]

Chapter 5

Review of techniques for measuring the optical properties of tissue

5.1 Introduction

In this chapter, an overview of the different methods of measuring the optical properties of tissues will be described. The relative advantages of the different methods will be discussed. The different methods of tissue preparation are also briefly considered. A short review of optical properties of tissue taken from the literature is also given.

5.2 Single scattering phase function

The single scattering phase function is the angular distribution of light resulting from one scattering event. In order to measure this distribution, it is necessary to use samples which are ~$1/\mu_s$ thick. For most tissues, this means a thickness of 10 - 40 μm[79]. Preparing such samples without altering their optical properties is difficult. Techniques for doing so have included a) grinding of samples to produce a homogeneous slurry, which can then be formed into a thin sample[96], and b) using a microtome to slice both frozen[97] and fresh[94] tissue. The first technique is easiest, but destroys any contribution to the scattering from the structure of the tissue, as well as possibly altering the shape of the scattering particles. Freezing of samples facil tates the use of a microtome, as it keeps the sample rigid. It is also likely to effect the structure and optical properties of the sample[98]. Other considerations include the freshness of the sample and the temperature, especially for fatty tissue, where the body temperature is close to or above

the melting point of many lipids, and room temperature is generally below it.

The measurement itself presents several problems. The dynamic range of the scattering phase function is large, the phase functions of most tissues being highly forward peaked, with the forward directed intensity being 4-5 orders of magnitude greater than that at angles greater than 60°. Also, tissues of the required thickness are not self supporting, and hence have to be mounted onto some material. Glass is usually used for this purpose, being both transparent, and possessing a refractive index not dissimilar to that of tissue. There is still, however, a refractive index change both between glass and tissue, and glass and air, which results in unwanted reflections and refraction. The light path through the sample changes as a function of angle, along with the area which is illuminated.

Several experimental systems for the measurement of phase functions have been used. Key et al[97] and Wilksch et al[99] held a sample between two glass cover slips in air. Flock et al[96] and Marchesini et al[100] used a sample held between two cover slips and placed in a circular water tank, with the source and detector outside the tank. At UCL, van der Zee et al [101] used a pair of glass hemi cylinders, with the sample held between them to form a glass cylinder with the sample in the middle. As part of this project, this latter equipment has been improved upon, and is described more fully in section Figure 6.15.

Both the latter methods attempt to maintain a constant angle between the input light beam and the main change of refractive index, but there is still a refractive index change between the water/glass and the sample. Also, as the beam is of finite width, the curved surface acts to some extent like a lens. This could be avoided for the water bath system by having the source and detector inside the bath. To reduce reflection at the water glass boundary, the water could be index matched to the glass by dissolving sugar in it, sugar increasing the refractive index of water up to 1.5[102].

The mean cosine of scatter, g can be calculated from the phase function. It can also be determined from measurements made on thicker samples using the diffusion equation. (see section 5.3.2)

5.3 Scattering and absorption coefficients

5.3.1 Direct measurement

Since both absorption and scattering remove light from its initial trajectory, an in-line measurement of intensity attenuation can only be used to determine μ_a or μ_s if one of them is much greater than the other. Measurements on tissue samples, where light is scattered as well as absorbed give only the attenuation coefficient, μ_t which is equal to the sum of the absorption and scattering coefficient.

On such scattering samples, care has to be taken that the thickness, x is such that multiple scattering does not occur, ie $\mu_s x << 1$. If this is not the case then multiple scattering of the light will occur, and the received intensity will contain a scattered component. This requirement for thinness can lead to preparation problems for biological samples (see section 5.2). Measurements of the attenuation coefficient have been made on tissue by Flock et al[96], Key et al[97], Peters et al[93], Marchesini et al[100].

5.3.2 Indirect measurement

In order to measure both μ_a and μ_s, some model of light transport is needed which calculates the surface fluence as a function of μ_a, μ_s and g. Usually, a measurement is made of the diffusely transmitted and reflected light on a thinnish (2-4 mm) slab of tissue. These measurement are then compared with a model of light transport through the slab. The model used is usually either the diffusion equation[103] or the Monte Carlo model[104,93] although the Kubelka Munk theory has been used in the past[105,106]. The absorption and scattering coefficients can be determined from these comparisons. Sometimes, in addition to the diffuse transmittance, the collimated transmittance is also measured[103]. This extra measurement allows an estimation of the anisotropy factor to be made.

Another way to determine the optical properties is to measure the diffusely reflected light at different positions on the surface of the tissue[107]. The diffusion equation can then be used to calculate the reflectance as function of distance. This method has the advantage that it can be used in vivo, but requires several different

measurements to be made.

Time resolved measurements have also been used to determine optical properties. In this case, the temporal distribution of either the reflected or transmitted light is made. This is then compared with predictions of the time dependant diffusion equation. Madsen et al[108] tested this latter technique, and found that in semi infinite phantoms, the results for both μ_s and μ_a were better than 10%. They also found that in smaller volumes, the technique is less accurate. Again this has the advantage that it can be used in vivo, but the equipment needed is bulky and expensive.

Prahl et al[109] suggested an alternative method of measuring the absorption and scattering properties by using pulsed photothermal radiometry to measure the temperature changes of the tissue due to absorption of light. This technique has the advantage that the received signal increases with absorption.

5.4 Review of the optical properties of tissue

Cheong et al [79] produced a comprehensive review of the published optical properties of tissue, although some of this data has been measured at wavelengths outside our range of interest (600-1000 nm), and much of it has been derived via Kubelka Munk theory, which has been shown to give rise to significant errors in the derived values[110] due to its unrealistic assumptions (see section 4.1.1).

The following table gives a summary of tissues relevant to this work.

Tissue	μ_a mm^{-1}	μ_s mm^{-1}	g	$\mu_s(1-g)$ mm^{-1}	wavelength nm
dermis	0.2 - 0.3	40	0.81-0.9	2-4	630
brain					
grey matter	0.05 - 0.09	50 - 60	0.95	2 - 4	600 - 1000
white matter	0.02 - 0.08	40 - 70	0.7 - 0.9	11 - 7	600 - 1000
breast					
fat	0.03 - 0.07	20 - 30	0.95 - 0.98	0.6 - 1.2	600 - 1000
glandular	0.03 - 0.06	20 - 40	0.92 - 0.96	1.2 - 1.3	600 - 1000
carcinoma	0.03 - 0.05	15 - 40	0.88 - 0.94	1 - 2	600 - 1000
fibrocystic	0.01 - 0.03	50 - 90	0.98	1.8 - 1	600 - 1000
fibroadenoma	0.03 - 0.07	40 - 20	0.98	1.2 - 0.4	600 - 1000
muscle	0.015 -0.02			0.9 - 1.1	800

The breast data is taken from Peters et al[93] and Key et al[97]. Dermis data from Graaff et al[104]. The brain data is from van der Zee[94] and the muscle from Barilli et al[111]

Tumours are in general more highly attenuating than the surrounding tissue, they absorb more strongly in some bands, eg < 600 nm, probably due to increased vascularity and hence haemoglobin content. The complex vascular structure and the cell density also lead to a higher degree of scattering by the tumour.

Chapter 6

Measurement of the optical properties of tissue and phantom materials

6.1 Introduction

This chapter describes the techniques which I have used for measuring the optical properties of phantom material and biological tissue. The first to be described is a method of measuring absorption and scattering coefficients separately. This is later used as a standard to investigate the accuracy of two other methods which measure scattering and absorption coefficients simultaneously. The first uses a pair of integrating spheres to measure the light transmitted through and reflected from a thin sample. Optical coefficients are derived from this measurement. The second involves measuring the temporal dispersion of light travelling through a thick sample of material, and uses the diffusion equation to derive the optical properties from this measurement.

The system for measuring the scattering phase function is also described.

6.2 Direct measurement of absorption and scattering coefficients.

In this section is described a method of directly determining absorption or scattering coefficients. This method was used to measure the optical properties of the phantom material [See chapter 8].

As stated in chapter 3 the coefficient of absorption or scattering is given by

$$\mu = -\frac{1}{Cx}\ln\left(\frac{I_x}{I_o}\right) \qquad (6.1)$$

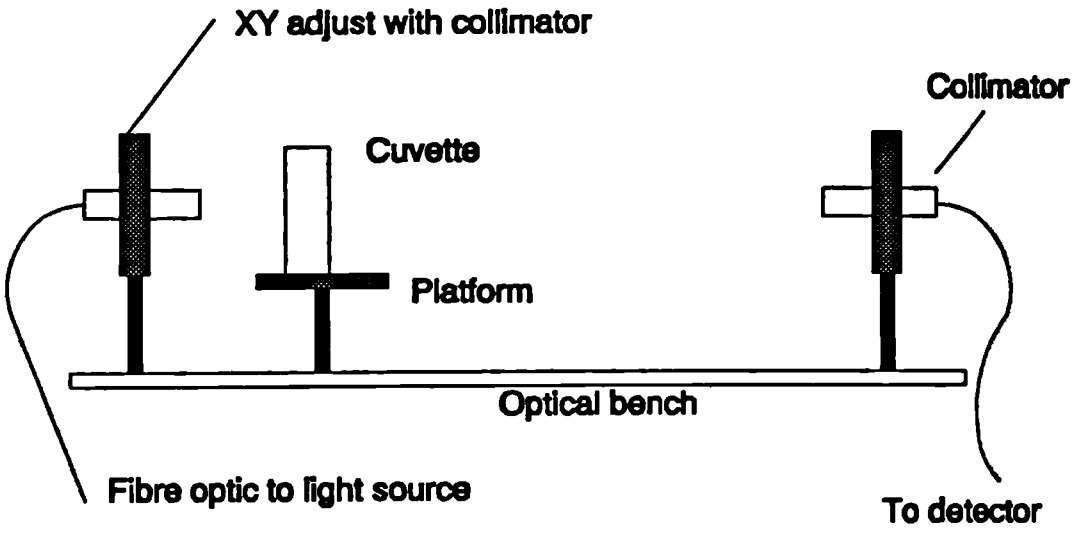

Figure 6.1 Showing the system for measuring collimated transmission through a sample.

where I_0 is the incident and I_u the unscattered light intensity, x is the thickness of the sample and C is the concentration of the scatterer/absorber. To determine the scattering or absorption coefficients directly, a means of quantifying the variation of the unscattered light intensity with thickness or concentration is needed.

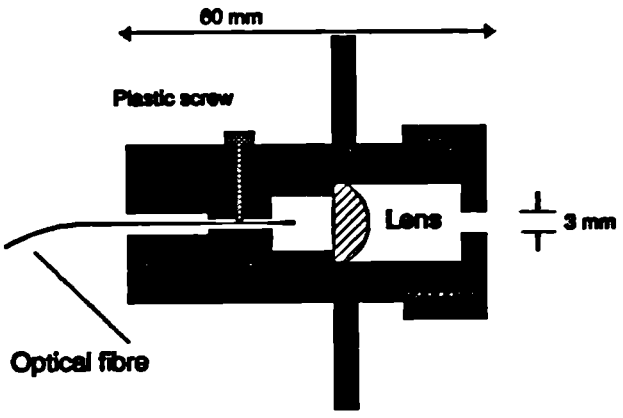

Figure 6.2 Showing a cross-section of one of the collimators.

To perform this measurement, a system was constructed which consists of an optical bench onto which is mounted two collimators and a platform (see Figure 6.1). A cuvette holding a sample can be mounted on the platform. The collimators are held on xy adjustable mounts, and consist (see Figure 6.2) of a lens with focal length of 16mm held between an aperture of 3mm in diameter on one side, and a channel for an optical fibre at the other. The optical fibre is a 100

μm diameter glass graded indes fibre with a polymer sheathing 0.5mm in diameter (Corning, New York) and is held in place with a plastic screw, enabling its position to be altered to place it at the focal point of the lens. This position was determined by moving the fibre until the spot size projected on the far end of the bench was at a minimum. This procedure was repeated for both collimators. The half angle of the collimated beam was estimated from a measurement of the beam size at the other end of the bench to be 0.15°.

The light source used was a quartz halogen broad band light source (Oriel Ltd), and the detector a cooled CCD spectrophotometer[112]. The spectral range of the detector covers 500 to 1050 nm. A diffraction grating is used to disperse the light over the CCD chip, giving 400 nm over the entire chip, For the measurements presented here, this was set to give a range of 630- 1030 nm. A coloured glass filter (Oriel, USA) was used to cut off wavelengths less than 650 nm, to avoid higher order diffractions. The resolution, which is controlled by varying the light entrance slit width, is set at 3 nm. A IBM compatible computer was used to collect the spectra.

The collimators were aligned in two stages. Initially, the fibre in one collimator was connected to the light source, and the two collimators were held closely together. The source collimator was moved laterally and vertically to make the light beam coincident with the aperture of the other collimator. Then, with the collimators far apart, the tilt of the source collimator was adjusted to bring the beam back onto the far aperture. This procedure was repeated iteratively until the light beam was in the correct position at both near and far separations. The alignment was performed initially by eye, but ultimately with the detecting fibre connected to the CCD spectrometer to measure the light intensity. The whole procedure was then repeated with the light source connected to the other collimator.

The cuvette on the platform was aligned perpendicularly with the light beam by rotating it until the specularly reflected light beam was coincident with the source collimator output hole. It was then fixed in this position on the platform.

The system was calibrated using polystyrene microspheres of precisely known diameter (Seradyn Ltd). These were in a 10% by volume suspension in water. They were agitated in an ultrasonic bath to ensure total dispersion of the spheres prior to the experiment, and the suspension was further diluted 10:1 in distilled water. A 50 ml volume of distilled water was poured into a 2 cm thick cuvette on the optical bench.

Into the cuvette were added 20 μl volumes of the dilute sphere suspension. The liquid was stirred, and the light intensity was measured after each addition. The scattering coefficient of the solution was then calculated from the variation of the light intensity with concentration using equation (6.1).

To calculate the theoretical scattering coefficient of the solution, Mie theory (see 3.3.2) was employed. This uses the refractive indices of the scattering particles and the medium, together with the particle size in comparison to the wavelength. The refractive indices of polystyrene and water in the near infrared were calculated using Cauchy's equation (3.21) to extrapolate data given in the CRC data book[102] and the American Institute of Physics handbook.[113]

This extrapolation of refractive index is shown in Figure 6.3, and the calculated dispersion equations are

$$n_w = 1.32 + \frac{3418}{\lambda^2} - \frac{4*10^7}{\lambda^4} \qquad (6.2)$$

for water and

$$n_p = 1.566 + \frac{7996}{\lambda^2} + \frac{3*10^8}{\lambda^4} \qquad (6.3)$$

for polystyrene.

The scattering coefficient calculated using this range of refractive indices is shown together with the measured scattering coefficient in Figure 6.4. As can be seen, there is a good agreement between the theoretical and measured scattering coefficient. The deviations at 600-650 nm are due to the filter used to cut off light less than

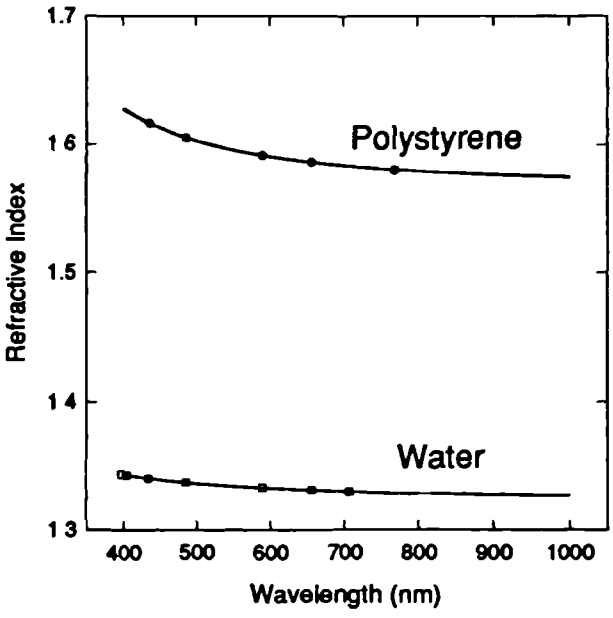

Figure 6.3 Showing the extrapolated variation of refractive index with wavelength for water and polystyrene. Symbols are literature values, solid line extrapolation.

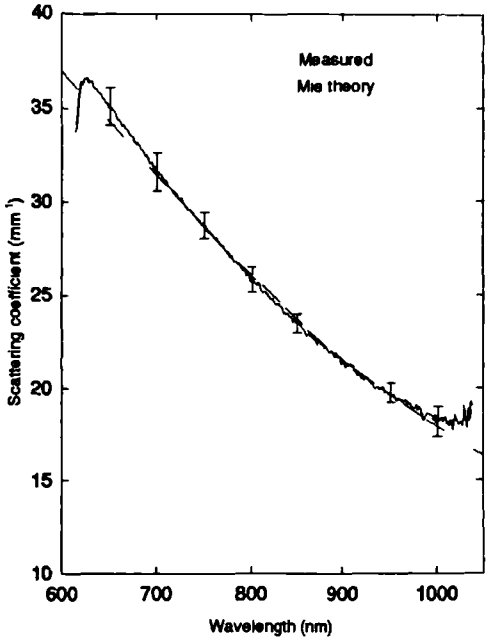

Figure 6.4 Showing the measured scattering coefficient of polystyrene spheres as compared with the value calculated by Mie theory. Errors bars ± 1 SD.

630 nm, and at greater than 1000 nm by the low detection efficiency of the CCD chip at these long wavelengths.

When measuring absorption coefficients with this technique, there may be situations where a small degree of light scattering by the sample is unavoidable. This occurs when measuring very low absorption coefficients such as those of the clear resin used as the base for the phantom. Scattering would lead to the absorption coefficient being overestimated as some of the transmitted light was scattered away from the detector. To avoid this, it is possible to use an integrating sphere to collect all of the transmitted light.

6.3 Phase function measurements

The measurement system consists of a goniometer turntable, mounted onto which are a dual pinhole collimator, and a collimated telescope. Optical fibre bundles were used to deliver light from the quartz halogen light source, and to the CCD detector (see previous section). To hold the sample, two glass hemi-cylinders were used, the sample being sandwiched between them to form a cylinder of 65mm diameter. A coupling liquid (Ethylene Glycol for tissue samples, and ethyl cinnamate for the phantom material) was used to provide optical coupling between the glass and sample. The hemicylinders have an anti reflection coating for 800nm.

After aligning the source and detector collimators, the sample holder was mounted on the goniometer turntable, between the collimated light source and detector

telescope. The cylinder was initially positioned so that the sample was oriented at an angle 80° in the horizontal plane to the incident light beam. This means that light which is specularly reflected from the sample-glass interface does not reach the detector, and hence reduces errors caused by the detection of spurious light which would otherwise occur.

Measurements were made by scanning the incident beam through 170°, moving the sample at half this angular rate to ensure that the light path through the sample is kept to a minimum, and so that the area illuminated was kept approximately constant. When the source beam had been scanned through 90°, the cylinder was rotated through 70° (Figure 6.6). This ensured that the illuminated area of the sample was kept approximately constant through the 90° - 170° range.

Initially, the detector simply consisted of a telescope which focused the incoming light onto the receiving fibre bundle end at its focal point, 185 mm away. This provided collimation with a half angle of 0.46°, but

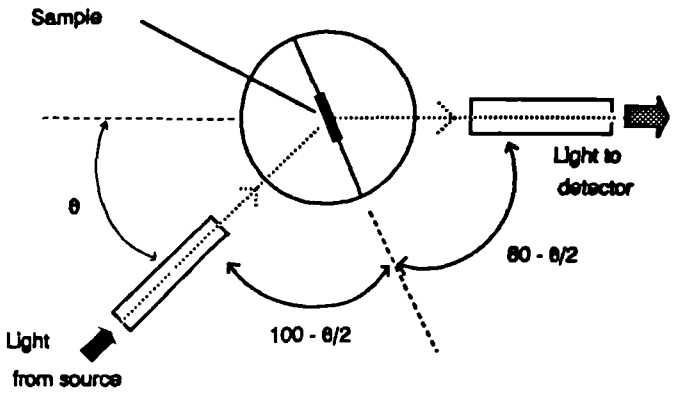

Figure 6.5 Showing the goniometer setup for measurements from 0 - 90°

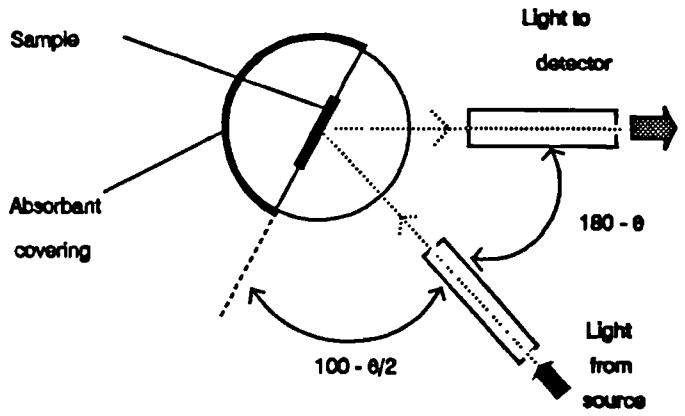

Figure 6.6 Goniometer setup for measuring angles between 90° and 170°

had an aperture of 25 mm, or an f number of 7.4. Measurements of the received intensity with only coupling fluid between the hemicylinders showed that this arrangement resulted in a system response which was too (see Figure 6.7). To improve this, the aperture of the detector was reduced by placing a pinhole of diameter 1 mm was placed in front of the telescope. This results in a half angle of 0.3°, which is the same as that from the source collimator. The resultant system response is also shown in Figure 6.7.

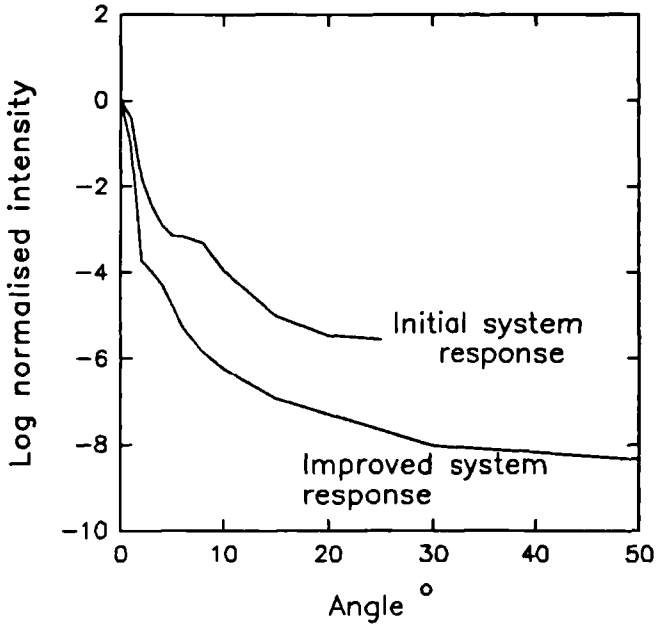

Figure 6.7 System response of the goniometer system

This figure shows the large dynamic range of the measurements. In order to keep the total collected light on the CCD chip approximately constant, the exposure time (which is computer controlled) was adjusted from 0.1 seconds to 2000 seconds (~thirty minutes)

For angles greater than 90°, it was discovered that light was being reflected from the rear surface of the cylinder and then being detected. To reduce this spurious signal, a piece of

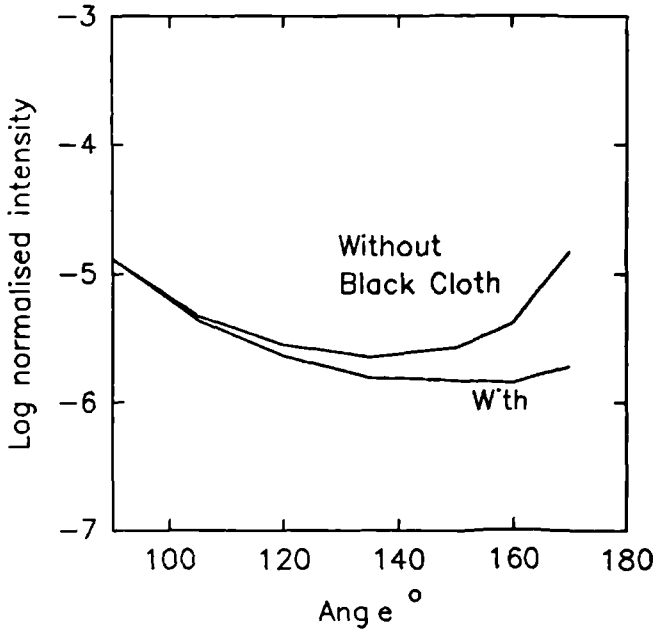

Figure 6.8 Showing the effect of stopping specularly back reflected light form being detected.

black cloth impregnated with propylene glycol (as a coupling liquid) was attached to the rear surface of the cylinder. The improvement that this produced is shown in Figure 6.8.

The system is still not perfect, especially for measuring the phase function of materials with a low value of g. For materials, which have a fairly isotropic scattering function, the angular range 50 - 140° has the greatest influence upon g, due to the sin factor in its calculation. In this angular region it is difficult to accurately measure the phase function, since it is low in intensity, and scattered light inside the hemicylinders causes artifacts. This is a particular problem in the 90 - 180 ° region, where any diffuse scattering from the glass - sample boundary will be detected and will lead to a greater measured intensity and thus reduce the calculated value of g.

6.4 Simultaneous measurement of μ_a and μ_s using a pair of integrating spheres

To simultaneously measure the scattering and absorption coefficients, a pair of integrating spheres were used to measure the diffusely reflected and transmitted light from a 2.5 mm thick sample. The spheres have an internal diameter of 6 cm and are internally coated with diffuse reflection paint (Kodak ltd 'white reflectance coating').

To measure the reflected light, a collimated beam of light was shone through a hole in the first sphere directly onto the sample. The diffusely reflected light was collected through a port hole in the wall of the integrating sphere by an optical fibre bundle, and carried to the CCD camera (see section 6.2) where the intensity was measured. A measurement was also made of the reflected light from a 99% reflectance standard (Oriel ltd)

To measure the transmitted light, a second sphere was placed on top of the sample, and the light was measured through another port hole in the second sphere. A measurement was also made of the transmitted light with no sample present. The arrangement for making this measurement is shown in Figure 6.9 and the position of the sample in greater detail in Figure 6.10.

The actual reflectance/transmittance of the sample cannot be simply related to the intensity measured in the spheres. This is because the light undergoes multiple

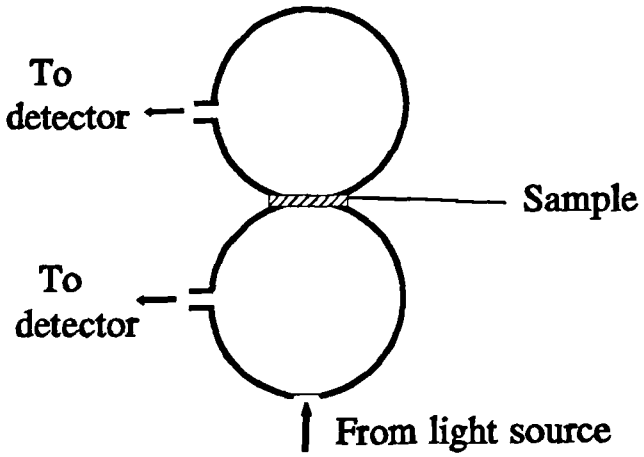

Figure 6.9 Integrating sphere arrangement for measuring diffuse reflectance and transmittance

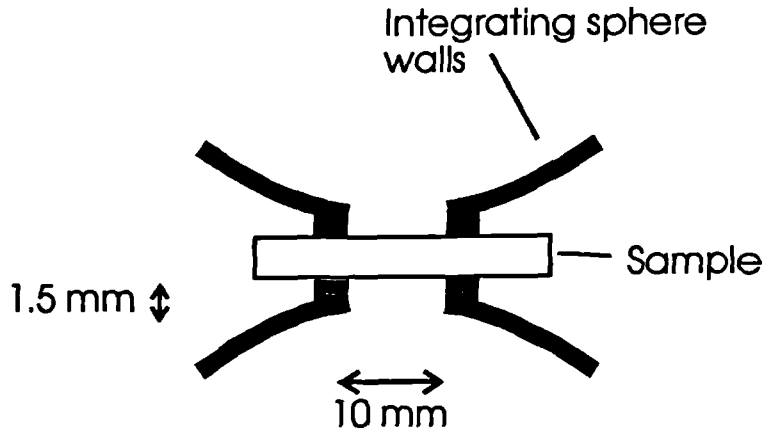

Figure 6.10 Showing a detail of the integrating sphere with the sample.

reflection inside the spheres, and is hence reflected numerous times from the sample before being detected. In the next section, details of formulae to convert the measured light intensity into absolute reflectance are given. I developed the equations presented in the next two sections, based upon analysis of integrating sphere theory by Pickering[114] and Ojala[115]

6.4.1 The reflectance sphere

Consider the reflectance integrating sphere with an incident collimated light source of power P. Since the light source is not perfectly collimated, a fraction f of the light can miss the sample and hit the sphere walls, which have reflectance m. A fraction $R_\perp$ of the light hitting the sample is specularly reflected, β hits the walls, and $(1-\beta)$ of this exits through the input port hole. The resulting light intensity is hence

$$R_1 = P\left[\,(1-f)(m\beta R_\perp + R_s(1-R_\perp)) \;+ mf\,\right] \tag{6.4}$$

where R_s is the internal reflectance of the sample; this is what we are trying to measure.

The light which is reflected from the sample then scatters off the walls (or is lost through the port holes). This produces a diffuse field, with intensity given by

$$R_2 = R_1\, ma \tag{6.5}$$

where a is the relative surface area of the sphere walls, A fraction γ of this light is detected.

The light then scatters again from the walls and from the sample, producing

$$R_3 = R_2\left[am + s(R_d+(1-R_d)R_s)\right] \tag{6.6}$$

where s is the fractional area of the sample port hole to total internal surface area and R_d is the average specular reflection for diffuse light. Again a fraction γ is detected. This is repeated ad nauseam, and the overall light D which is detected is γ (R_2 + R_3 + ...), which can be written as

$$D = \gamma R_2(1 + A + A^2 + \ldots..) \tag{6.7}$$

where

$$A = [am + s(R_d+(1-R_d)R_s)] \tag{6.8}$$

The (1 + A ..) term is a geometric series, and its sum is given by 1/(1-A), hence

$$D = \gamma P \left[\frac{(1-f)(m\beta R_\perp + R_s(1-R_\perp)) + mf}{1-am-s(R_d+(1-R_d)R_s)} \right] ma \tag{6.9}$$

To calibrate the system, reflectance standards are used. These are diffusive reflectors, and $R_\perp$ and R_d are both zero. For a standard with reflectance of R_w,

$$D = \gamma P \left[\frac{R_w(1-f) + mf}{1-am-sR_w} \right] ma \tag{6.10}$$

Dividing Equation (6.9) by Equation (6.10) enables us to find an expression for R_s which does not depend on the incident power.

$$R_s = \frac{Q_1(1-ma-r_d s)(R_w(1-f)+mf) - (1-ma-R_w s)(mr_\perp(1-f)\beta+mf)}{(1-ma-R_w s)(1-r_\perp)(1-f) + Q_1(1-r_d)s(R_w(1-f)+mf)} \tag{6.11}$$

where Q_1 is the ratio of the detected light from the sample to the detected light from the reflectance standard.

6.4.2 The transmittance sphere

For the transmittance case, we have to consider both spheres, as the light can pass from one to the other.

The light intensity, I which is incident on the sample is given by the sum of the collimated light and a fraction, s of the diffuse light intensity in the first sphere. This latter contribution is given by equation (6.9) and results from the multiple reflections in the sphere from the initial reflection.

$$I = P\left[\left(\frac{(1-f)(m\beta R_{\perp} + R_s(1-R_{\perp})) + mf}{1-am-s(R_d+(1-R_d)R_s)}\right)sma + (1-f)(1-R_{\perp})\right] \quad (6.12)$$

A fraction T of I is transmitted through the sample, and in a similar fashion to that described for the single sphere, gives rise to a diffuse intensity D_2

$$D_2 = \left[\frac{I}{1-a'm-s'(R_d+(1-R_d)R_s)}\right]Tma' \quad (6.13)$$

a′ and s′ being the relative areas of the walls and sample hole in the second sphere.

To complicate matters, a fraction s′ T of D_2 is transmitted through the sample to the first sphere. A fraction sT of this is then transmitted back again. This gives an intensity of BD_2 in the second sphere, where

$$B = \frac{s'T}{1-am-s(R_d+R_s(1-R_d))}\cdot\frac{sT}{1-a'm-s'(R_d+R_s(1-R_d))}m^2aa' \quad (6.14)$$

the overall distribution of light in the second sphere is given by D_2 (1+B + B^2 +....) and again the total distribution is given by D_2/(1-B)

Measurements in the second sphere are calibrated using a measurement of the transmitted light in the absence of a sample. In this case, T = 1 and the reflectance is obviously zero.

The ratio Q_2 of the transmitted light with a sample present to the transmitted light in the absence of a sample can be written as

$$Q_2 = \frac{ITma'}{d'\left(1-\frac{ss'T^2m^2aa'}{dd'}\right)}\cdot\frac{1-a'm-\frac{s's\,m^2aa'}{1-am}}{\frac{smf}{1-am}+1-f} \quad (6.15)$$

where

$$d = 1-am-s(R_d+(1-R_d)R_s) \quad \text{and} \quad d' = a-a'm-s'(R_d+(1-R_d)R_s) \quad (6.16)$$

It is possible to rearrange this equation to give a quadratic equation of the form

$aT^2 + bT + c = 0$, where

$$a = m^2 a a' \frac{ss'}{d}\left(\frac{smf}{1-am}+1-f\right)Q_2$$
$$b = I\,ma'\left(1-a'm-\frac{s's}{1-am}m^2aa'\right) \qquad (6.17)$$
$$c = -d'\left(\frac{smf}{1-am}+1-f\right)Q_2$$

6 4.3 Calibration and Improvements to the system

In order to calibrate the integrating spheres, reflectance standards of 99, 75, 50 and 1 % (Oriel Ltd) were used and measurements were made of the reflected intensity from each of the standards. A measurement was also made with no sample present, with a polished piece of silver, and another with a clear sample of the resin used for the phantom material.

The wavelength variation of the reflectance of the paint on the sphere walls was taken from manufacturer's data (Kodak). The surface area of the sphere walls was calculated by subtracting the area of port holes from the total surface area.

The collimation of the light source in the integrating spheres originally was simply provided by a lens, and is shown in Figure 6.11. The main problem with this arrangement is that as the light entered the sphere, part of the light beam was hitting the edges of the entrance hole, causing a fraction of it to scatter over the sphere interior. From measurement of the reflectance with no sample present, it was found that approximately 10% of the collimated light was missing the sample and hitting the walls of the sphere. As this causes errors in measuring low values of reflectance, it was decided to improve this arrangement by changing the collimator design. A holder was constructed which held the source fibre bundle 5 cm away from the sphere and introduced a pinhole just in front of the sphere input port hole. Figure 6.12 shows the new arrangement. This reduced the amount of light missing the sample to 0.3 %

The reflectance from the standards was calculated using equation (6.11) and the reflectance factor of the walls adjusted (to 99% of its initial value) to give the best fit between the calculated reflectance and the manufacturers data for the standards. These fits are shown in Figure 6.13. The manufacturers data were at 50 nm intervals, and

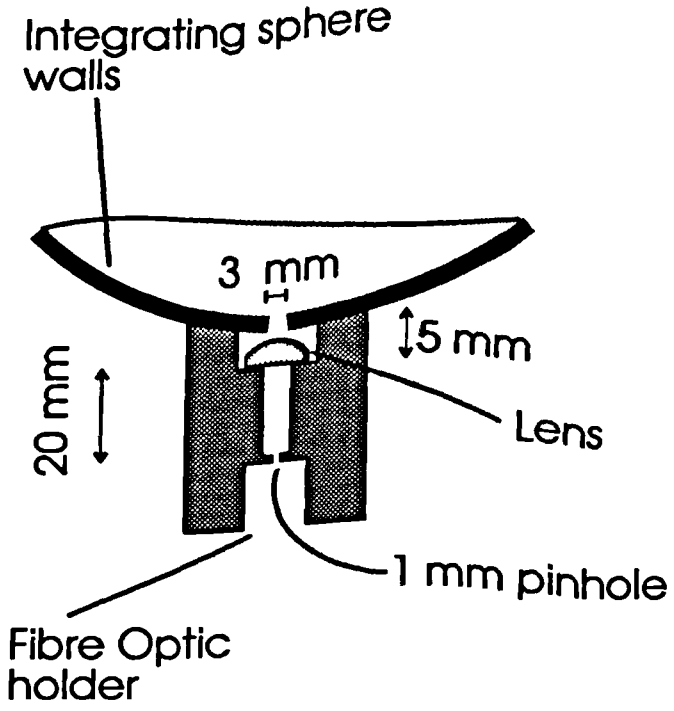

Figure 6.11 Showing the original collimation system for the integrating spheres.

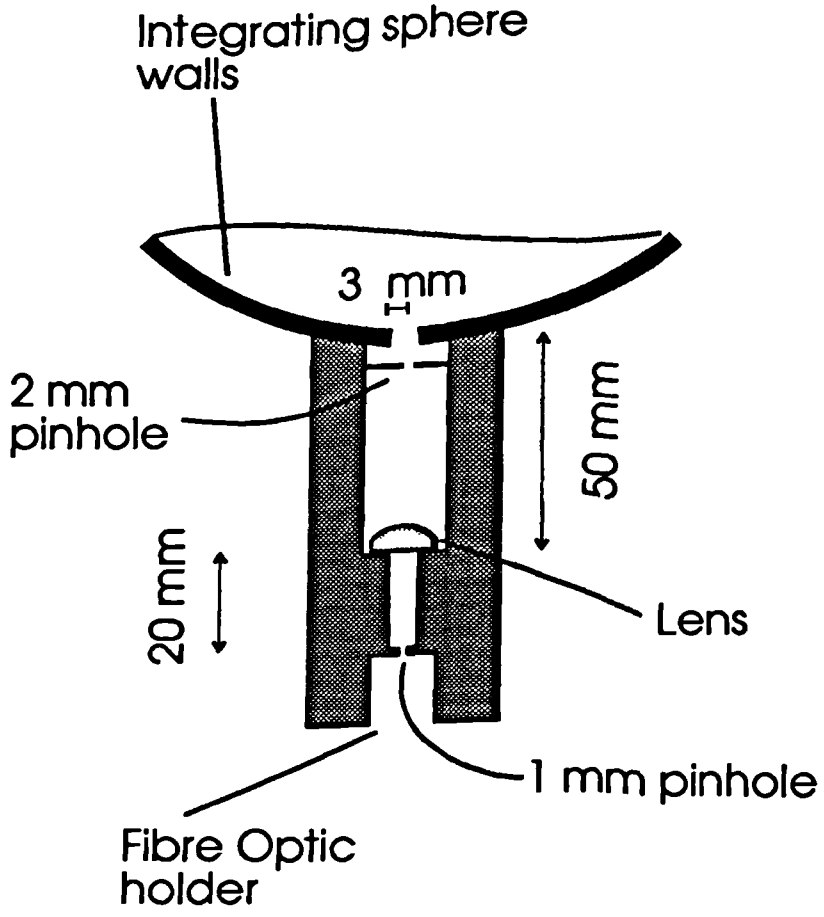

Figure 6.12 Showing the improved collimator for the integrating spheres.

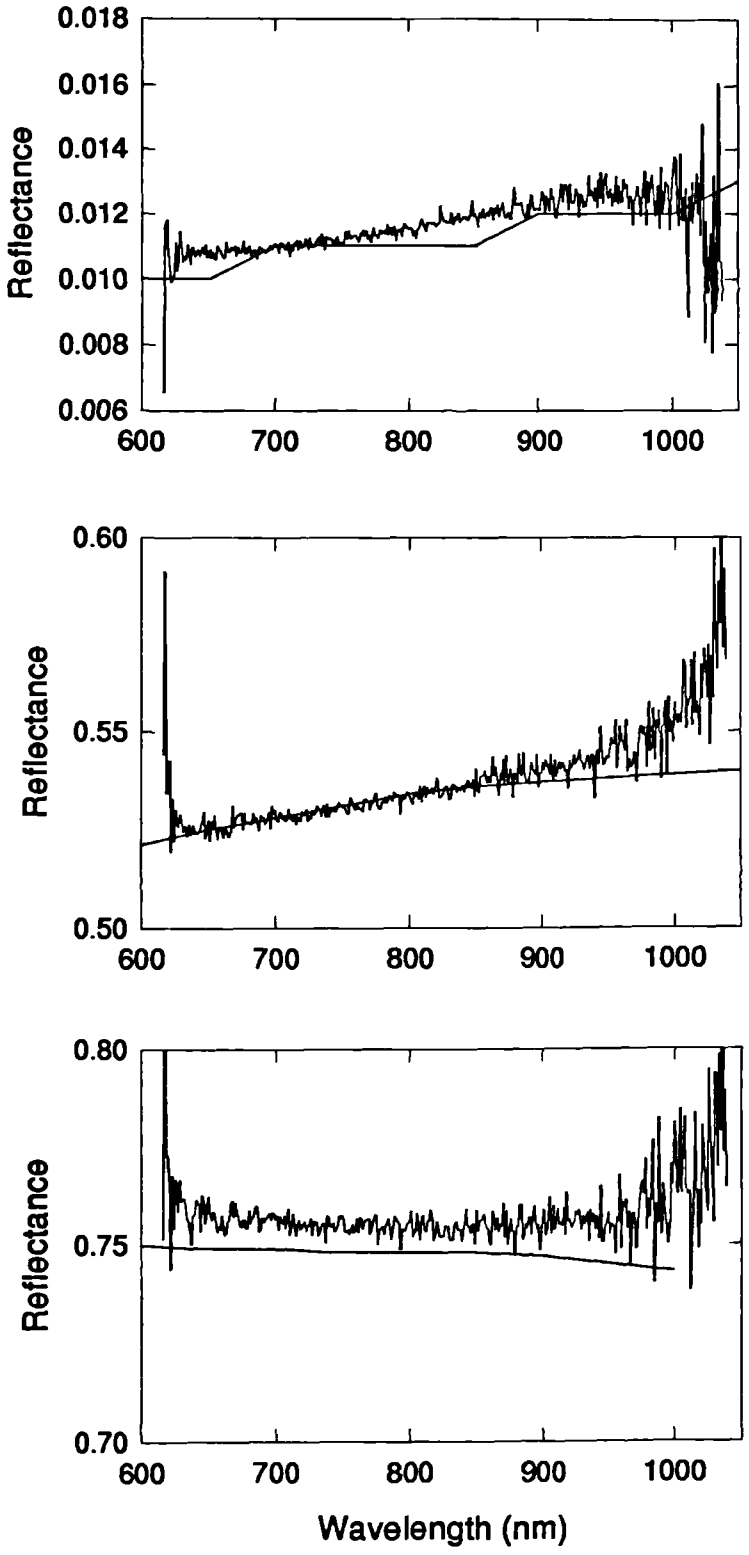

Figure 6.13 Graph showing the reflectance from the standards as measured using the integrating spheres in comparison with the manufactures data.

these have simply been interpolated, which gives rise to a step like variation for the 1% standard. For this standard, there is approximately a 4 % variation between the calibrated and measured values. This is an improvement on the 10 % variation observed before the collimator was changed. For the 50 % standard, better than 1 % agreement is observed for most of the wavelength range (dropping to 2 % at the edges of the spectrum, due to low light detection). With the 75 % standard, the values agree to approximately 1 %. The reason that a better agreement is not found may be because the integrating sphere formulas assume that the spheres are wholly spherical, while, as Figure 6.10 shows, the sample is slightly set back from the sphere.

The specular reflectance from the phantom was calculated using the fresnel formulae.[116] For the diffuse specular reflection, the average reflection was calculated using:

$$R_d = \frac{\int_0^{90} R(\theta)\sin(\theta)}{\int_0^{90} \sin(\theta)} \qquad (6.18)$$

Using a refractive index of 1.57 (measured - see 8.4.4) for the phantom material gives a specular reflection $R_\perp$ of 0.049 at 90° and a diffuse reflection R_d of 0.22. When using the system to measure the optical properties of tissue, as these are not self supporting, glass cover slips can be used to hold the sample and give it defined edges. The cover slips used (Chance Propper, Smethwick) had a refractive index of 1.51. This gives a specular reflection $R_\perp$ of 0.042 and a diffuse reflection R_d of 0.21.

In order to calculate β (the fraction of the specularly reflected light which exits the sphere), a measurement of the reflected light from a

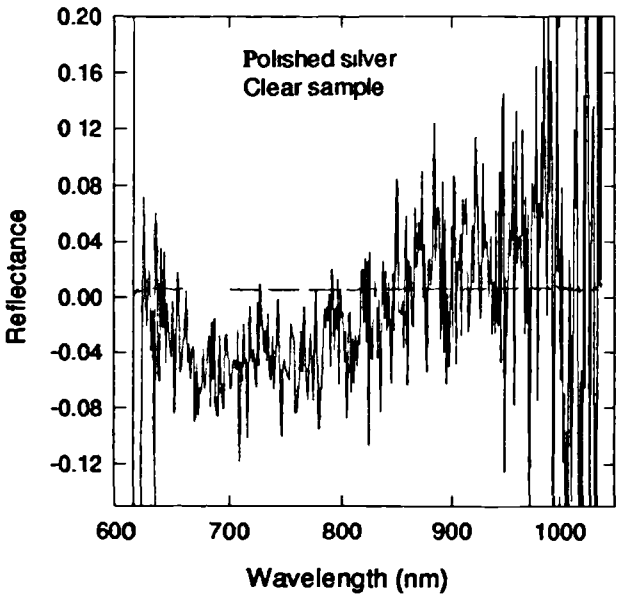

Figure 6.14 Showing the difference between the measured and expected reflectance from polished silver and clear polyester samples.

polished silver flat was made. β was calculated from the difference between the reflectance measured in the integrating spheres and the value given in the literature[102], 0.93 for our wavelength range of 600-1000nm. Figure 6.14 shows the difference between the measured and actual reflectance for silver. As an independent verification of this measurement, the reflectance from a clear sample of the resin was measured. In order to prevent reflections from the second surface, the sample was coated on its far side with strongly absorbing dye (PROJET 900NP, Zeneca Ltd) dissolved in ethyl cinnamate. Using the above specular reflectance factors, the non specular reflectance was calculated, and is also shown in Figure 6.14. This is very close to zero (R = 0.005), as would be expected.

6.4.4 Monte Carlo inversion

In order to convert the measurements of reflected and transmitted light into absorption and scattering coefficients, a Monte Carlo simulation of the experimental system developed by van der Zee[94] was used. This uses the experimental geometry and calculates the transmittance and reflectance as a function of μ_a and μ_s. This simulation can use an experimentally measured scattering phase function to calculate the angular distribution of the photons as they scatter. The measured reflectance and transmittance are then compared with the calculated values by a step wise search using a Newton Raphson technique. Linear interpolation is then used between the closest data to give a more accurate estimate of μ_a and μ_s.

6.5 Measurement of optical properties from transmission through a slab

A separate method for measuring the optical properties of a large block of material is to measure the intensity and time distribution of light transmitted through the block. These measurements can then be compared with the diffusion equation to derive the optical properties.

The TPSF (temporal point spread function) is the temporal distribution of light resulting from a very short pulse of light transmitted through a medium. Measurement

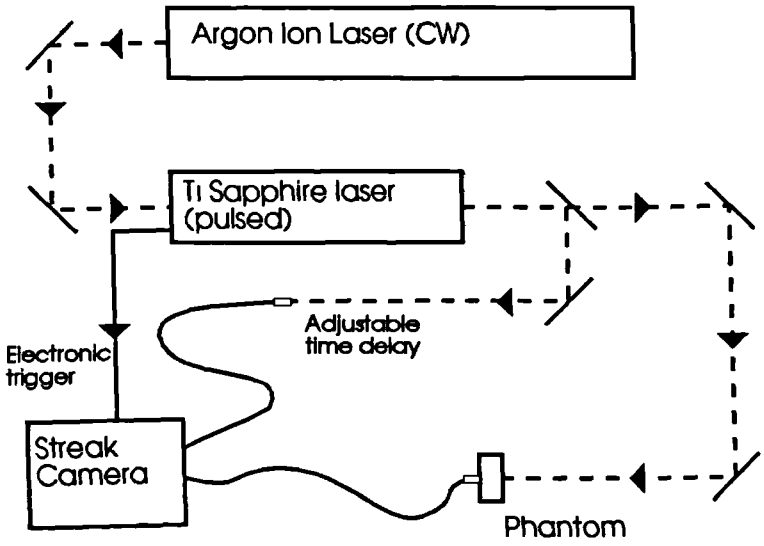

Figure 6.15 Showing the experimental configuration for measuring the temporal distribution of light

of the TPSF was made using a picosecond pulsed laser (Tsunami, Spectra physics Ltd) and a synchroscan streak camera (Hamamatsu Ltd) to detect the light pulses. The experimental configuration is shown in Figure 6.15.

A least squares fit of the transmitted light profile to the time dependant diffusion equation for an infinite slab[117] was made using a program written by Jeremy Hebden (of the department). This fits the entire shape of the TPSF to the diffusion theory, using the absorption coefficient and reduced scattering coefficient as variable parameters.

Chapter 7

Optical properties of skull

7.1 Measurement of the optical properties of skull

An extensive search of the literature yielded no measured data on the optical properties of bone in the wavelength region that we are interested in, the closest being data for the complex index of refraction of dentine at 10.0μm[118]. To correct this deficit, measurements were made, using samples of bone obtained from the adult pig skull. This bone was chosen for several reasons. Firstly, the physical and chemical composition of bone of the adult large mammals does not vary greatly[120] and hence adult pig bone is a good substitute for adult human bone. Secondly, the frontal/parietal bone of the pig is a flat plate of approximately 2cm in thickness, from which it is easy to prepare samples of a suitable size. The results presented in this chapter have previously been published as a paper[121]. The systems used to make these measurements have been investigated with the phantom material (see 9.3) and the optical properties of bone can be interpreted in the light of these comparisons.

7.1.1 Sample Preparation

The heads of freshly slaughtered pigs were obtained from a commercial butcher, and the parietal bone was removed. All surface tissue was removed by careful scraping with a scalpel blade. The bone was then sawn into pieces approximately 20 mm square with a hacksaw, the bone samples being about 15mm thick. From these pieces, sections approximately 2 mm thick were cut, either parallel or perpendicular to the surface, using

a slow speed diamond saw (Buehler Ltd). These were then placed in a 0.9% saline solution in an ultrasonic water bath for 30 minutes to remove as much blood as possible. These samples were used for the measurement of diffuse reflectance and transmittance. When making the measurements, the samples were held between glass cover slips, with a ethylene glycol providing optical continuity. This was to try to provide a constant and quantifiable amount of specular reflection.

Thin bone slices for the scattering phase function measurement were prepared from these samples by grinding with 400 grit abrasive paper (Buehler Ltd), with the samples held in a water soluble wax (Crystalbond 555, Aremco Inc.). These were again washed in the ultrasonic bath to remove any grit. These sections were approximately 60-90 μm thick and 5mm square. In the goniometer apparatus, ethylene glycol was again used as a coupling liquid between the glass hemicylinders and the bone.

7.1.2 Measurements

7.1.2.1 Results

Pieces of bone were obtained from a total of three pig's heads. Six separate samples were taken from each for the integrating sphere measurements (ie 18 samples in total), and two samples from each were prepared for the phase function measurements (ie 6 samples in total). Figure 7.1 shows the average of the scattering phase functions measured at 800 nm, together with

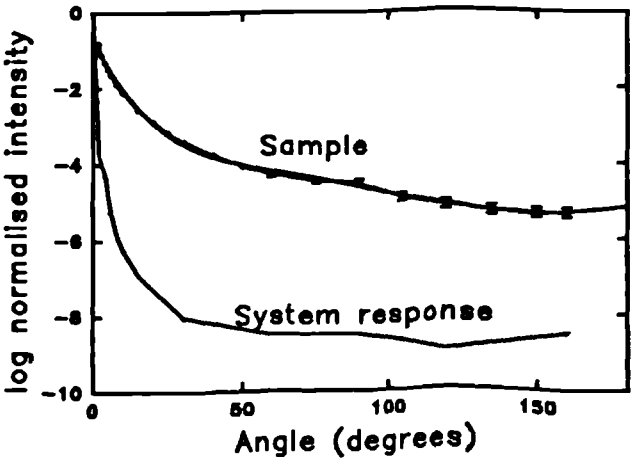

Figure 7.1 The phase function of bone at 800nm. Error bars ± 1 sd

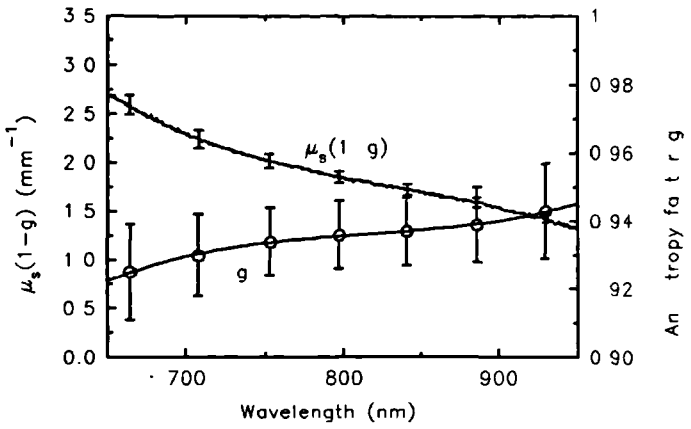

Figure 7.2 Transport scattering coefficient and g value of bone. Error bars ± 1 sd.

transmission and reflection at 90°. It is reasonable to assume that the phase function should be smoothly varying, and the data between 80° and 100° was rejected, and a smoothly varying polynomial was fitted over this range. A similar method was used to extrapolate from 170° to 180°. This fitted phase function was used in the Monte Carlo calculation for the integrating sphere analysis

the angular response of the system. The two sets of data measured at 0-90° and 90-170° were fitted together by matching the values of scattered intensity at 90° for the reflection and transmittance measurements. As can be seen, this procedure results in a small peak in the phase function at 90°. This peak is thought to be a measurement artifact due to the difference between

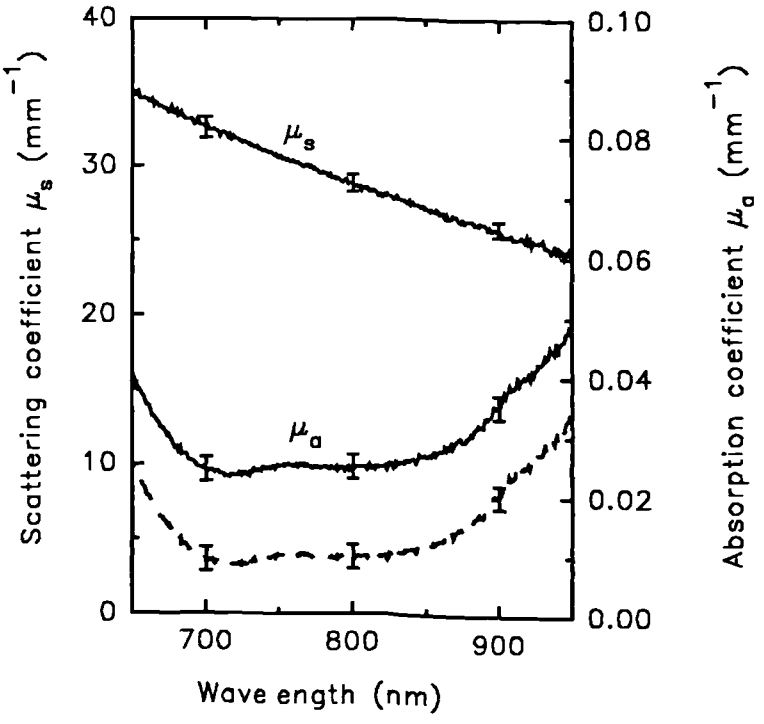

Figure 7.3 Scattering and absorption coefficients of bone. Error bars ± 1 sd. The μ_a spectrum corrected for a systematic error of + 0.015 mm^{-1} is also shown (dotted line)

Figure 7.2 shows the transport scattering coefficient, together with measured values of g over the wavelength range 650-950 nm. Finally, Figure 7.3 shows the scattering coefficient together with the absorption coefficient as a function of wavelength.

The scattering phase function is highly peaked in the forward direction, having an average g value of 0.93, varying by only a few percent over the wavelength range. The major components of bone are hydroxyapatite (58%), collagen (25%), water (12%) and carbohydrate (5%) (White et al[122]). The average size of hydroxyapatite crystals is 30 x 3 x 3 nm and that of collagen molecules 300 x 1.5 x 1.5 nm[123], and since they are much smaller than the wavelength of the illuminating light, isotropic scattering should ensue. Since this is not the case, the scattering must be dominated by conglomerations of the crystals, which have a much greater scattering efficiency than the individual crystals.

The scattering coefficient shows an almost linear fall with wavelength over this wavelength range, and there were no noticeable differences between data obtained from samples cut parallel or perpendicular to the skull surface. Measurements made on the phantom material (9.3) indicate that these results are correct to within 10%

Subsequent analysis of the accuracy of the integrating sphere technique showed that there is a systematic error (see 9.3.1), the measured absorption coefficient is approximately 0.015 mm^{-1} too large (wavelength independent). The main features of the absorption spectra are the water peak above 900 nm, and a rise below 700 nm together with a small ripple at 750 nm, which are attributable to residual deoxygenated haemoglobin.

Chapter 8

Phantoms

8.1 Introduction

A phantom in the medical physics context is simply an inanimate object or material (ie other than a patient), on which equipment is tested or used. The phantom is usually designed to match the properties of the tissue in respect of the quantity being measured.

In the field of near infra red (NIR) monitoring, phantoms are needed for three separate functions. First of all to investigate the accuracy of systems for measuring the optical properties of tissue. Secondly to ensure that measurements made by NIR spectroscopic instruments are correct. Finally they are needed to investigate the potential of imaging in tissue using NIR light. It must be possible to manufacture the phantom with known optical properties, and these must be similar to those of tissue.

Several types of phantom have previously been used by different investigators. As a substitute for the overall tissue medium, some of the substances used have been whole milk[37], non dairy creamer[33,124], intralipid[77,125,126,127,128], polyester microsphere suspensions in water[89,129], wax[130], cheese and ham slices[131], and a yeast and blood mixture[132]. The absorbers which have been used include india ink[125,77], molecular dyes[129] and blood[124,28]. For imaging, items used as test objects to be imaged have included black plastic rods[39], metal rods[27] and spheres[133], and in a rather bizarre paper by Benaron[36], a hamburger, and a screw inside a homogenized olive suspended in a mixture of blood and yeast. A more typical phantom (eg Yoo et al [37]) would be a glass/perspex box, containing intralipid (a fat/water emulsion) as a scattering medium, a dye added to give the required absorption, and an absorbing object, eg an anodised metal sphere suspended at various positions.

This vast range of substances has several disadvantages. Firstly, the 'biological' materials are not precisely reproducible, and their optical properties are not known exactly. There is also a noticeable difference between the cheeses and milks of the world. Intralipid is less variable, and some experimentally measured data has been published on its properties[134]. However, there is probably still some sample to sample variation especially between different brand. Also, it deteriorates once exposed to air, as it is a vegetable oil based emulsion. Suspensions of polystyrene microspheres in water provide a good phantom, though they cannot be left to stand in suspension for too long, as they settle, although this could conceivably be avoided by using a gelling agent.

Indian ink is not ideal as an absorber, as Madsen et al[135] have shown that it also acts as a scatterer. They found that it is a suspension of carbon particles of diameter 0.1 μm, but that ~1.5% of the particles were agglomerates of diameter 1 μm, which results in an albedo of ~ 0.3, ie 1/3 of the incident light is reflected.

A basic description of the phantom material presented in this chapter has been published in 'Physics in Medicine and Biology'[136]. A much fuller description is given here, along with improvements and measurements of its optical properties which have since been made.

8.2 Choice of phantom for this work

In order for a phantom to be useful as a calibration standard, it must have defined optical properties and be both stable and reproducible. Although phantoms made by suspending particles in water are reproducible, they are not stable, due to short term settling of the particles, and in the long term, agglomeration of settled particles. A further problem with liquid phantoms occurs in their usage in imaging experiments, where phantoms which have variable contrast between different regions are needed. In liquid phantoms, in order to have regions of differing optical properties, a boundary between the regions is required, and this boundary (eg a test tube) will introduce unwanted optical inhomogeneities into the phantom.

In order to have a material with a variety of scattering and absorbing properties, but with the same basic refractive index, I chose to design a phantom around a clear colourless polyester plastic (Clear embedding resin, Jotun Polymers (UK) Ltd). The

liquid resin consists of unsaturated polyesters dissolved in ~35% styrene. Absorbing dyes and scattering particles can be added to the liquid to give it the required optical properties. Addition of a catalyst leads to polymerisation and the formation of a solid.

8.3 Components of the phantom and production thereof

To produce scattering in the phantom, a concentrated suspension of titanium dioxide particles in a paste compatible with the resin was used ("super white pigment" Tiranti Ltd, London). To alter the absorption of the phantom, a range of solid dyes which were developed by Zeneca ltd were used. These absorb in the region 600-1000 nm. A stock solution of each dye in styrene was made. A quantity of this dilute dye was added to the resin to give it the required absorbance. Once the desired quantities of absorber and scatterer have been added to the liquid, addition of a hardener results in the material setting to form a rigid and stable solid.

For making small phantoms (<100 g), all the components are simply added to the resin in a beaker and then mixed together by hand. For making larger phantoms, the mixing was done with a mechanical mixer (Janke & Kunkel, Germany). When making large phantoms, to ensure that the scattering particles are thoroughly mixed in the resin, it is best to mix the scattering paste into a small amount of resin (~30 g) before adding this to the rest of the resin. After thorough mixing, to remove any air bubbles, the samples were placed in a vacuum chamber which was pumped down with a rotary pump (Edwards, Sussex) for about 5

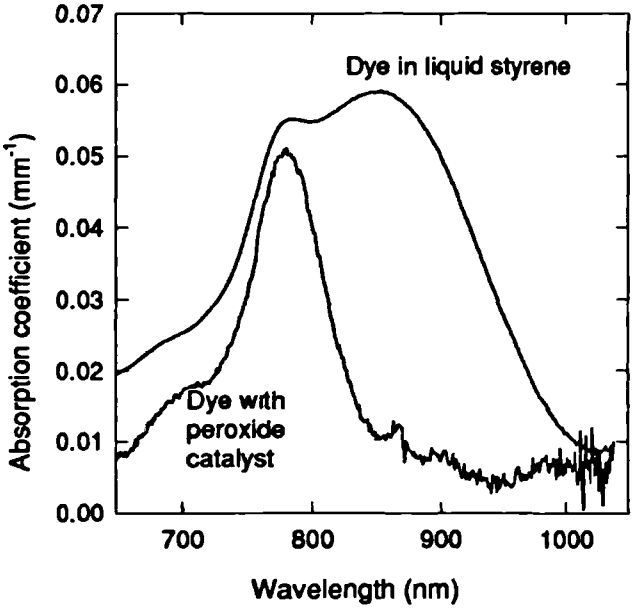

Figure 8.1 The effect of different catalysts on the absorption spectra of a dye (PRO JET 900 NP, Zeneca Ltd).

minutes. The mixture was then poured into a mould.

The catalyst which was initially used was methyl ethyl ketone peroxide (Tiranti Ltd), but it was discovered that this was reacting with the dyes used, and effectively reducing their absorption (see Figure 8.1). This problem was solved by using a different catalyst, azo-iso-butyronitrile (AIBN). Using this catalyst, the resin needs to be heated to 110° C for approximately an hour in order for the polymerisation to occur. It was found empirically that the optimum amount of catalyst is 0.03 % by weight for large blocks (bigger than 100g) though slightly more is needed for smaller quantities of resin.

When producing large phantoms (>500g), it was found that attempts to cast the block in one go inevitably resulted in cracks forming in the plastic. These are a result of the shrinkage (~6 %) which occurs during setting. To avoid this unfortunate occurrence, it was found by experiment that the blocks should be cast in several stages, about 200 g at a time. Moulds for casting the resin should ideally either be coated with silicone grease, or constructed from non stick material such as PTFE or polypropylene. This prevents the resin from adhering to the mould and enables the resin to shrink away from the walls during curing.

One problem arising with this combination of AIBN and polyester is that there are fluctuations in the refractive index of the plastic, which give rise to a rippled effect in a clear sample. These fluctuations are thought to be due to separation of the two polymers in the resin (styrene and polyester). The scattering caused by the fluctuations is too small to have an effect on the scattering coefficient when particles are added to the resin, though they do produce a problem in accurately measuring the absorption coefficient of the clear resin.

8.3.1 Index matching liquid

A refractive index matching liquid is required for the phantom. This is used in the measurement of the scattering coefficient where it is necessary to prevent diffuse reflection at the boundary of the phantom sample. Index matching liquid is also needed in the construction of phantoms with inhomogeneities in them for imaging purposes. The liquid in this case is needed to fill the gap between the different parts of the phantom (see section 9.6).

Ethyl cinnamate was chosen as the index matching fluid. This has a refractive

index, n_d of 1.55 at 589 nm, which is sufficiently close to that of the phantom material n_d = 1.58. A perfect match is difficult to obtain, since very few liquids (especially non toxic ones) have such high values of n_d.

In order to check that ethyl cinnamate does not react with the plastic, a piece of the phantom was placed in a beaker containing ethyl cinnamate and left there for 2 months. There was no discernable change in the appearance of the sample, the measured thickness of the piece did not alter over this period, and it had not noticeably softened. Ethyl cinnamate also has the distinct advantage of being non toxic.

8.4 Optical properties of the phantom

8.4.1 Scattering properties

To measure the scattering coefficient of the phantom, the collimated light system described in section 6.2 was used. A total of four samples of polyester with TiO_2 were prepared containing differing quantities of the TiO_2 suspension, varying from 0.03 to 0.4% by weight. From initial measurements using the integrating spheres system, it was estimated that this would be equivalent to scattering coefficients varying from 1 to 5 mm^{-1}.

Circular samples approximately 2mm thick and 2 cm in diameter were cut from a larger cylinder, and their surfaces polished flat using 400 grit paper. For ease of handling, they were then bonded to a glass microscope slide with clear epoxy resin. A 2cm thick glass cuvette was filled with ethyl cinnamate as a index matching liquid. To measure the scattering coefficient, the sample was placed in this

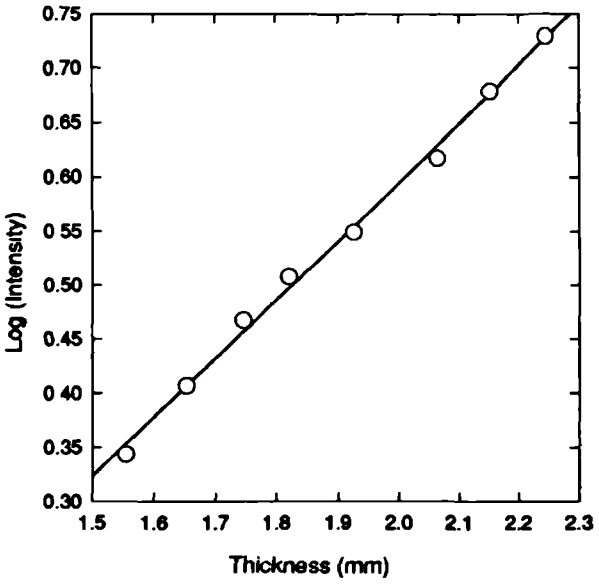

Figure 8.2 Showing the variation on one of the samples at 800 nm of the unscattered transmitted light against thickness of glass (~1.5 mm) + sample.

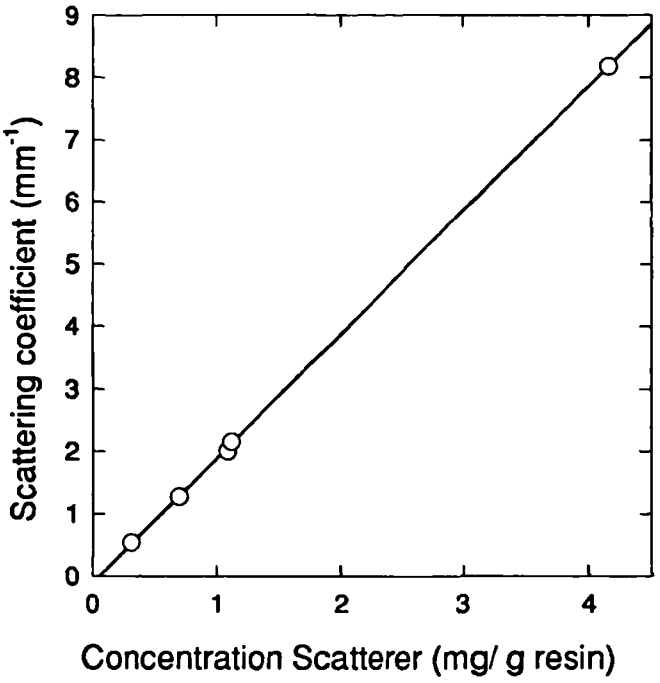

Figure 8.3 The variation of scattering coefficient with scatterer concentration at 800 nm for five samples of the phantom material.

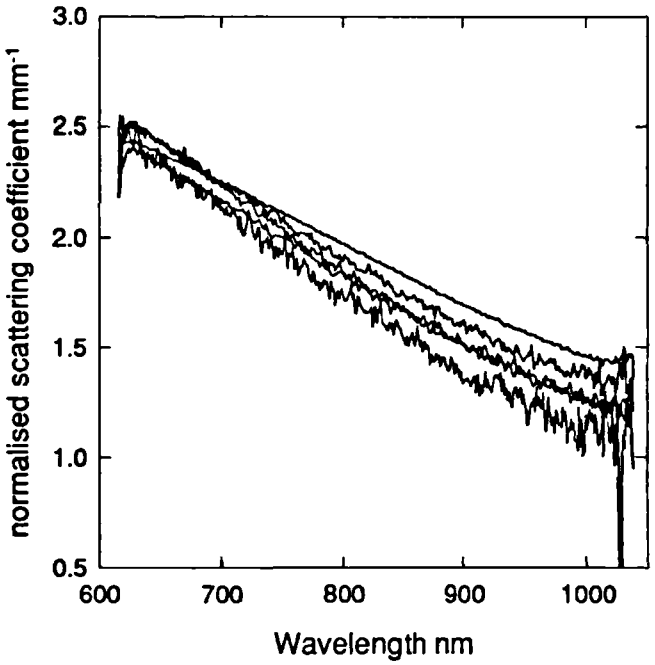

Figure 8.4 Scattering coefficient versus wavelength for 5 different samples, μ_s normalised for scatterer concentration.

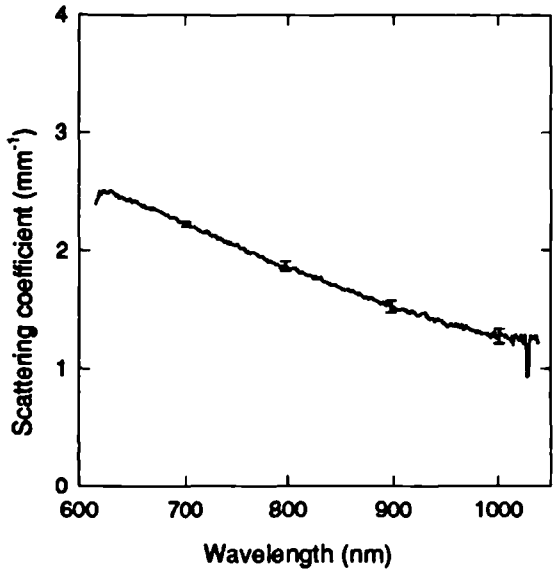

Figure 8.5 Average scattering coefficient as a function of wavelength. (Error bars ± 1SD)

cuvette and a measurement of the transmitted unscattered light made. The sample was then removed and its thickness reduced by grinding with 400 grit emery paper. A micrometer was used to measure the thickness, ensuring that it did not vary by more than 0.01mm over the area of the sample. Figure 8.2 shows the variation of transmitted intensity with thickness of one sample at 800 nm. From the slope of this graph the scattering coefficient was calculated. The variation of the measured scattering coefficient with the concentration of scattering particles is shown in Figure 8.3 for 800 nm. Figure 8.4 shows the scattering coefficients normalised for the scatterer concentration as a function of wavelength. Figure 8.5 shows the average scattering coefficient against wavelength.

The largest source of error for this measurement is in determining the thickness of the sample. As the grinding was done by hand, it was difficult to ensure that the surface being ground remained uniformly parallel to the back surface. It is estimated that this could lead to a systematic error in the thickness measurement of up to 5%.

The scattering properties of the TiO_2 particles are dependent on their size. To determine their mean size, the concentrated solution was diluted with the resin solvent (styrene) and 2 samples were prepared for a scanning electron microscope by pouring this solution on a target and evaporating the solvent. On each sample, 150 particle were randomly chosen, and their diameter on the x axis measured. The particles appeared roughly ovoid. The measured distribution is shown in Figure 8.6 and follows approximately normal distribution with a mean of 0.27 ± 0.07 μm.

A measurement of the particle density of TiO_2 in the concentrate was also made. To make the measurement, a 1ml syringe was weighed. It was then filled with the concentrate and weighed again. The volume fraction (vf) of the TiO_2 was then

calculated to be 0.33, using

$$vf = \frac{m-\rho_l}{\rho_t-\rho_r}$$

where m is the total mass of the concentrate, ρ_l the density of the liquid, 1.2 kg/ℓ (manufacturers data) and ρ_t the density of TiO_2 4.26 kg/ℓtaken from CRC data book[102].

If the particles are assumed to be spherical, Mie theory can be used to calculate the theoretical μ_s from the measured volume fraction and size distribution. Dispersion equation for the refractive index of TiO_2 as a function of wavelength were taken from the American Institute of Physics handbook[113].

$$n_e^2 = 5.913 + \frac{2.441*10^5}{\lambda^2 - 0.803*10^5}$$

$$n_o^2 = 7.197 + \frac{3.322*10^5}{\lambda^2 - 0.843*10^5}$$

(o is the ordinary ray and e the extraordinary ray - $TiO_2$is birefringent) Measurements were made of the refractive index of the polyester (see 8.4.4). The results of a calculation of

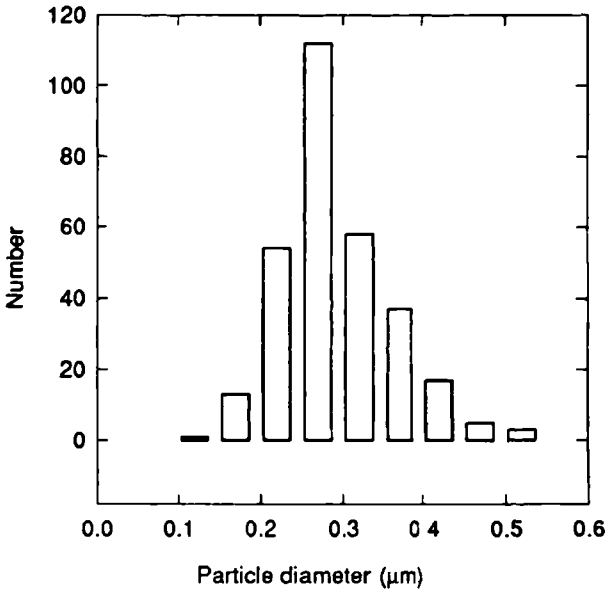

Figure 8.6 Particle size distribution as measured with an electron microscope. (2 samples and total of 300 particles)

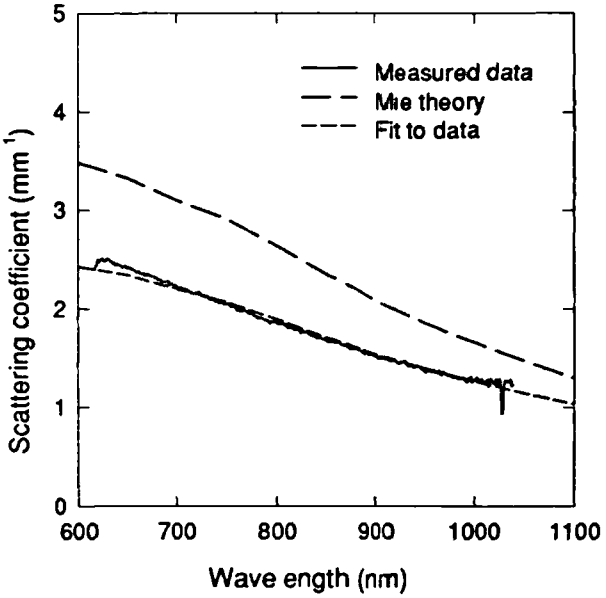

Figure 8.7 Comparison between the measured scattering coefficient and the theoretical value (calculated using the measured size distribution).

scattering coefficient are shown in Figure 8.7. As can be seen, this is somewhat higher than the measured scattering coefficient, but this difference can be explained if we assume that a portion of the scattering particles are clumped together. The figure also shows a typical best fit to the measured scattering coefficient, using a larger particle distribution. This has 64% of the particles with the measured size, and 36% with a diameter four times larger, having the same size distribution. It must be remembered that many other size distributions can give this shape of curve.

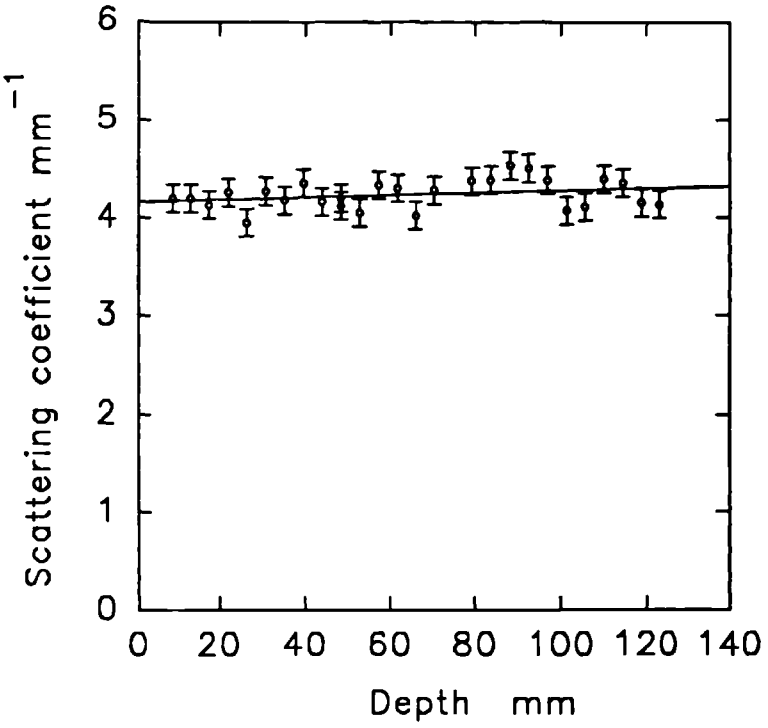

Figure 8.8 Showing the variation in scattering coefficient along the length of a 13 cm sample

Integrating spheres were used to measure the variation of μ_s with depth on a 13 cm long sample of the phantom. There is only a slight variation with depth (see Figure 8.8). This is due to settling of the particles. This measurement was made on a phantom cast with the original catalyst. The phantoms made with AIBN as a catalyst have a similar setting time, and hence any settling will not be worse.

8.4.2 Angular scattering function

The average angular scattering distribution of the TiO_2 particles in the resin, measured on 3 samples at 800 nm is shown in Figure 8.9. Also shown in this figure are the phase function calculated using the measured size distribution, and that calculated using the size distribution giving the best fit to the μ_s data. The latter gives a better fit over the 0-90° range, which is the region where the goniometer is most accurate. The

wavelength dependence of g is shown in Figure 8.10. This is an average of the three different samples. Unfortunately, the calculation of g from the measured scattering function may be somewhat inaccurate (estimated systematic error ± 0.05), due to the imprecision in the goniometer measurements (see section 6.3). The value of g calculated from Mie theory using the measured size distribution is also shown in the figure, along with that from the best fit.

The average value of g is somewhat lower than that of most tissues, 0.55 as compared with 0.7 - 0.99. (Cheong et al[79]). The maximum possible g value obtainable with this resin and TiO_2 particles is approximately 0.7, obtainable by using 0.7μm radius particles. Higher values of g are obtainable by using scattering materials of different

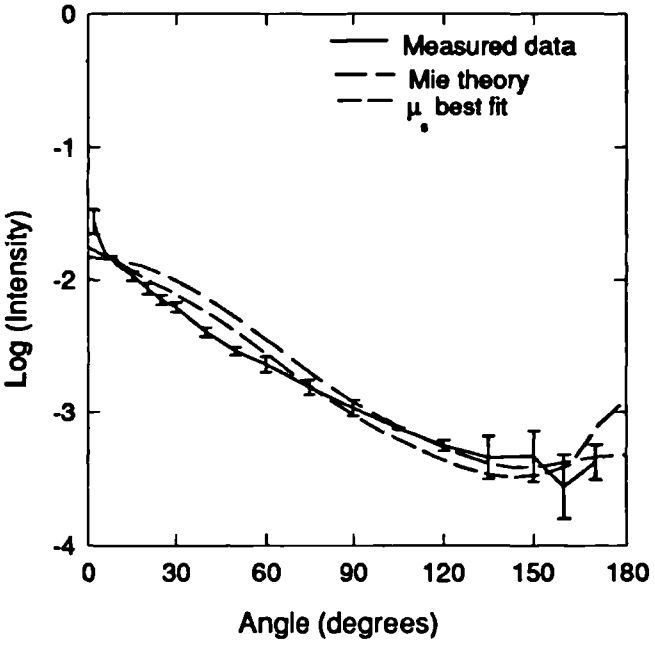

Figure 8.9 Averaged phase function (from 3 samples) of titanium dioxide particles in polyester resin at 800 nm (± 1SD)

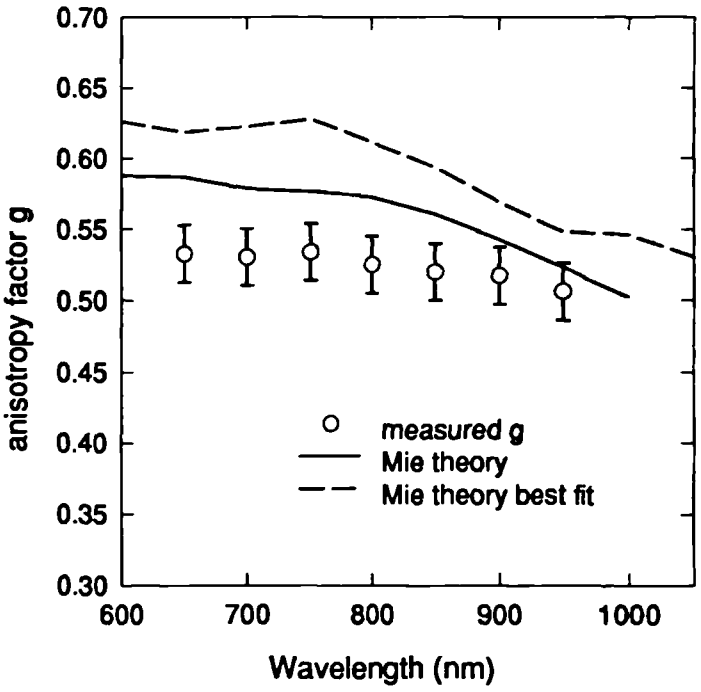

Figure 8.10 Showing the variation of g with wavelength (± 1 SD). The systematic error is ±0.03. Also shown is the value calculated from Mie theory using the measured size distribution and the distribution from the best fit to μ_s.

refractive index such as silica (see section 8.4.6).

8.4.3 Absorption properties

A range of dyes for addition to the resin are available from the manufacturer, but these absorb mostly in the visible region. Dyes which absorb light in the near infrared region (600-1100 nm) and which are compatible with the resin are available, and the absorbance spectrum of three such dyes developed by Zeneca ltd are shown in Figure 8.11. All of the data presented here is of the dye with the broad absorption band between 750-950 (PRO JET 900 NP).

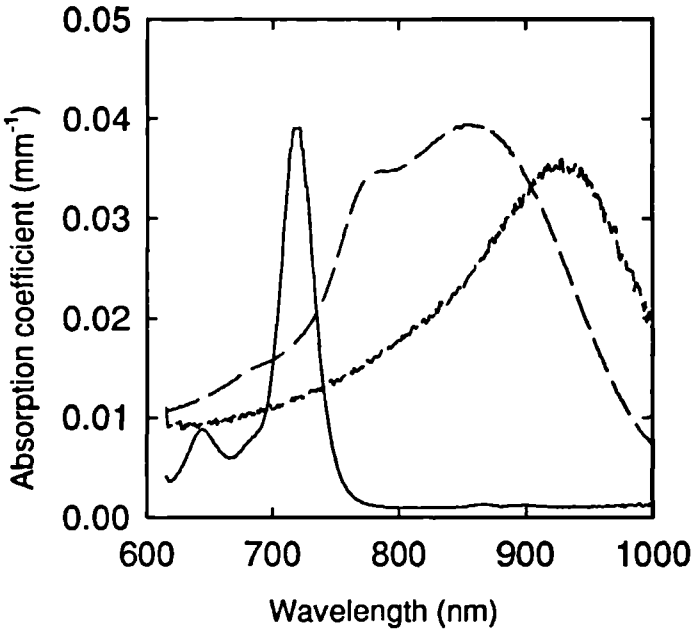

Figure 8.11 Absorption spectra of some dyes. S103508/5 (solid line) PRO JET 900NP (dashed line) and S159521/1 (dotted line).

To measure the absorption coefficient of the resin, an integrating sphere was used to collect the light from a collimated source transmitted through the samples. This was used to reduce the errors due to beam displacement

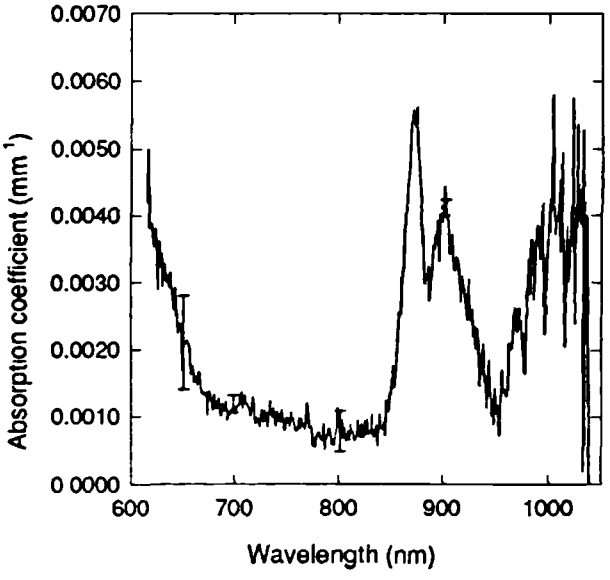

Figure 8.12 The absorption spectra of the resin (± 1 SD)

caused by fluctuations in the refractive index of the polyester (see section 8.3).

The absorption coefficient of the clear resin was measured on a total of 6 samples, varying in thickness between 2 cm and 7 cm. Figure 8.12 shows the resulting absorption spectra. As can be seen, the intrinsic absorbance of the plastic is low, approximately 0.001 mm^{-1} in the 650 to 850 nm region, and there is an absorption peak of 0.005 mm^{-1} at 875nm.

The absorption coefficient of the dyes in samples of resin with no scatterer were measured using the collimated system in an identical fashion to the measurement of scattering coefficient. Four different samples were used for the measurement. These had a relatively high concentration of dye added in order to minimise any errors due to scattering.

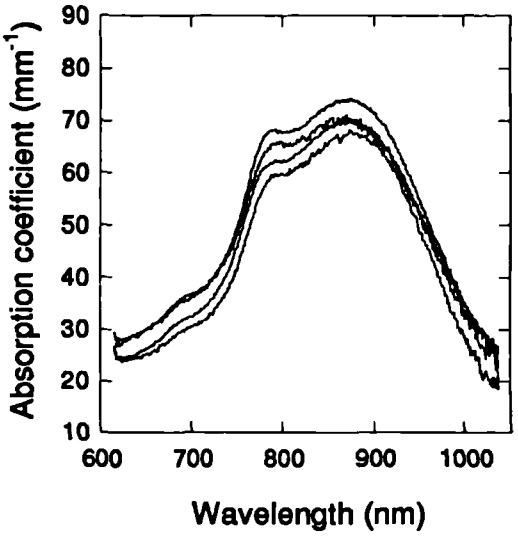

Figure 8.13 Graph showing the variation of absorption coefficient with wavelength for several different samples of dye in resin.

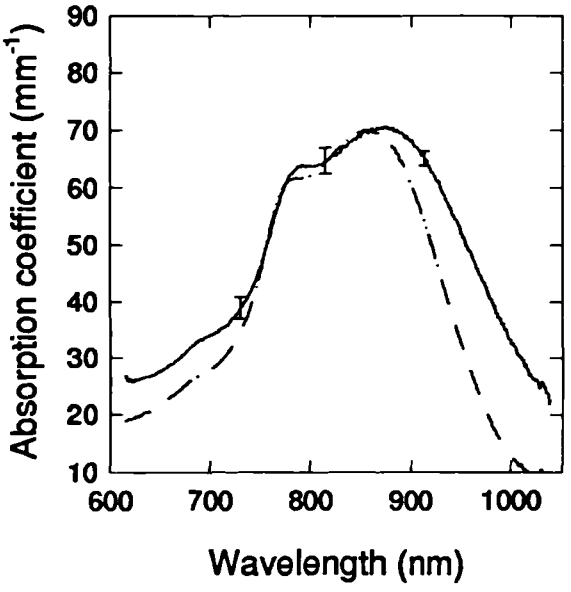

Figure 8.14 Graph showing the average absorption spectrum for dye in resin in comparison with the absorption coefficient for the dye in liquid styrene.

Figure 8.13 shows the absorption coefficient on these samples, and Figure 8.14 the average absorption coefficient in comparison with the absorption coefficient of the dye dissolved in liquid styrene. The absorption spectra of the dye is broader in the solid polyester. This is probably because the dye molecules are now bonded in a solid, and their absorption bands have hence changed.

8.4.4 Refractive index of the phantom

An important parameter to know is the refractive index of the plastic. This is a factor in determining the temporal distribution of light scattered in the plastic, as a larger refractive index obviously means that light travels more slowly through the material.

Knowledge of the refractive index also enables calculation of the scattering coefficient if the size and refractive index of the scattering particles is known.

To avoid possible error involved in measuring on a small sample of resin (since small local variation of refractive index could be seen), the refractive index was measured using the picosecond laser and streak camera to time a pulse of light as it travelled through a large clear block of polyester (17 cm thick). The refractive index, n was calculated as

$$n = 1 + \frac{ct}{d} \quad (8.3)$$

where c is the speed of light in vacuo, t the time delay introduced by the block, and d the block thickness. To make the

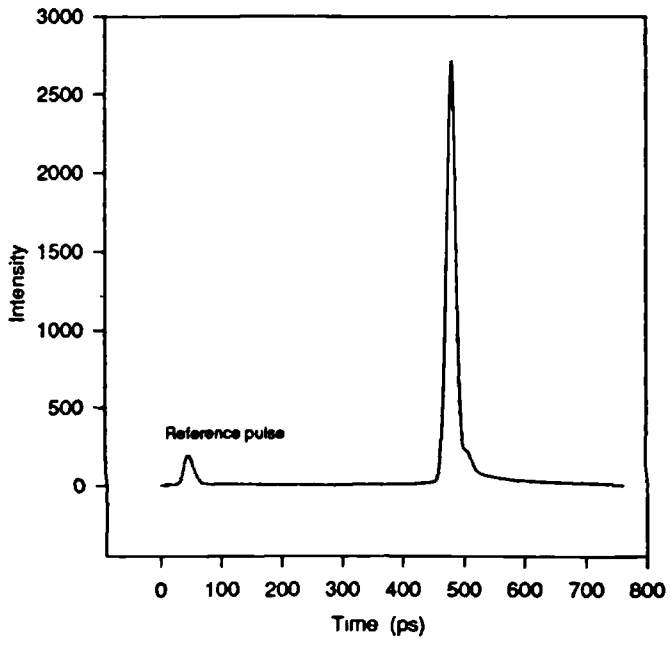

Figure 8.15 Showing the measured time delay of an ultra short pulse of light through a 17 cm thick clear block of polyester (at 800nm).

measurements, two pulses were recorded by the streak camera, one which had travelled through the block, and a reference pulse. The reference pulse was offset from the main beam by 100 ps, and a separate measurement was made of the pulse separation with no sample present. Figure 8.15 shows a typical pulse distribution. The refractive index was measured at 12 different points in the 765 - 870 nm wavelength range. The variation of refractive index with wavelength is shown in Figure 8.16. This figure also shows the refractive index of polystyrene[113] in comparison - the phantom is ~30 % polystyrene, and some separation of the polystyrene and polyester is thought to occur. No values for the refractive index for pure polyester were found in a search of literature.

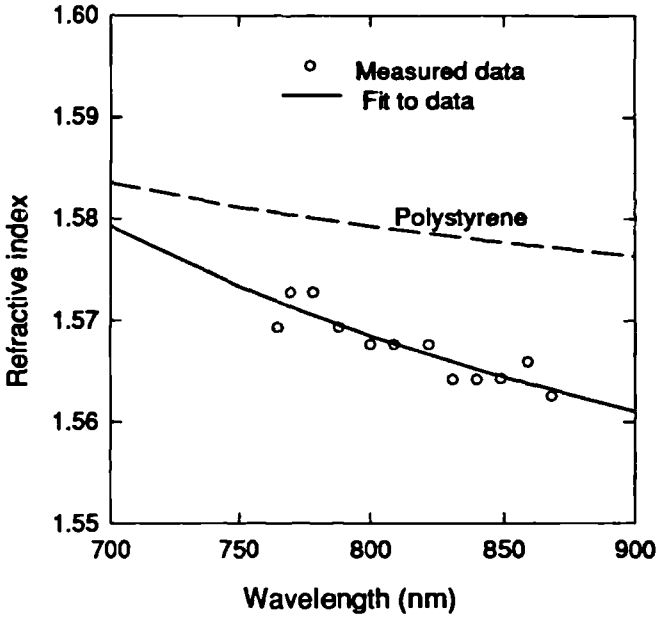

Figure 8.16 Showing the measured variation of refractive index with wavelength. The refractive index of polystyrene shown for comparison.

8.4.5 Stability of the phantoms

Once set, the scattering coefficient of the phantom cannot change, since the scattering particles cannot settle, and the refractive indices of the particles and the resin will not change. Water absorption by the polyester (Manufacturers data) 25 mg / 7 days.

The absorption coefficient of the material could, however be subject to change, since it is possible for the dyes to fade with time and from exposure to light. To check whether this was the case, two phantoms were made, using two dyes of interest (projet 900 NP, and S103508/5). Two samples were cut from each of these phantoms. One set

was kept in the dark, and the other exposed to ambient room light (under fluorescent lighting). The diffuse reflection and transmission through these samples was aperiodically measured over 130 days using the integrating spheres and the absorption and scattering coefficients calculated. The results of these measurements are shown in Figure 8.17. The dyes show very little variation in their absorption over time. The increase in the absorption on second and third data points on the S103508/5 (at 720nm) are thought to be an artefact due to undetected damage to the interior coating of one of the integrating spheres at the time of these measurements. This was subsequently discovered and repaired, and the absorption coefficient shows little change after this.

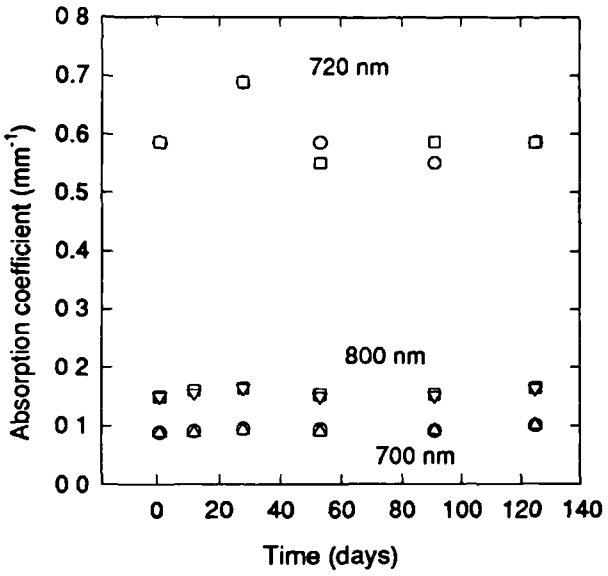

Figure 8.17 Showing the variation of absorption coefficient with time. Upper set of data at 720 from S103508/5. The other two are from PRO JET 900 NP. Triangles show data from samples kept in the dark.

8.4.6 Scattering suspensions of silica spheres

The phantom described above uses titanium dioxide particles to cause scattering. These have the disadvantage of having fairly isotropic scattering, due to their high refractive index. This makes it difficult to exactly match tissue which has a highly forward directed scattering distribution.

As an alternative to TiO_2 we tried amorphous silica spheres ('Monospher 1000M' Merck ltd) These have a refractive index of 1.42 at 550nm and a narrow size distribution, with a diameter of 1000 ± 20 nm. Other sizes are available, but at the

moment, they are only obtainable in small quantities, since Merck are not commercially producing them as yet. The spheres are coated with a methacrylic reactive group which aids dispersion in the resin. To make the measurements presented here, the spheres were dispersed using a mixture of stirring and ultrasonic bathing. If the silica was to be used on a regular basis, a concentrated suspension of the spheres in resin could be made using a ball mill. This could then be used in a sililar fashion to the concentrated suspension of TiO_2 described in previous sections.

The spheres have the added advantage that, since their refractive index and size distribution are accurately known, it is possible to calculate their scattering coefficient from Mie theory when they are suspended in a medium with a known refractive index.

8.4.6.1 Scattering properties of the silica spheres

As an initial experiment, the spheres were suspended in styrene monomer, and their scattering coefficient was measured. This was done for two reasons. Firstly to check that the spheres would disperse in the resin, which is 30 % styrene. Secondly, it is easier to measure the scattering coefficient of a liquid sample.

The spheres were suspended in styrene using an ultrasonic bath to agitate the mixture for 10 minutes. Then, measured quantities of the sphere suspension were added to a cuvette containing a measured volume of styrene. The transmitted unscattered light was then measured using the collimated system

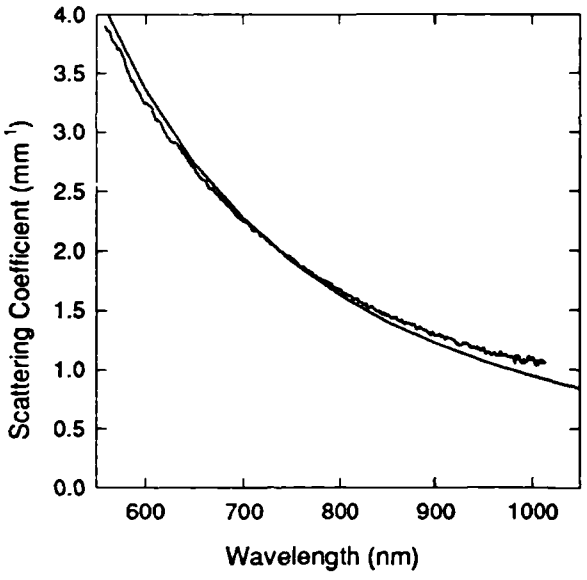

Figure 8.18 The scattering coefficient of the silica spheres in styrene: smooth data calculated, noisy data measured values.

described in section 6.2 and the scattering coefficient calculated. Results from this are shown in Figure 8.18 . The refractive index of styrene (1.566 at 486 nm, 1.5485 at 589 nm & 1.5419 at 656 nm) was taken from the American Institute of Physics handbook[113]. These data were interpolated out to the infrared using the Cauchy equation (3.21), giving:

$$n = 1.511 + \frac{13163}{\lambda^2} + \frac{64}{\lambda^4}$$

The refractive index of silica was quoted as 1.422 at 550 nm by Merck. To estimate its variation with wavelength, data for the wavelength dependence of the refractive index of fused silica was used[113]. From these two sources, a dispersion equation for silica was derived:

$$n = 1.41 + \frac{4168}{\lambda^2} - \frac{9.1}{\lambda^4}$$

These formulas were in Mie theory calculation of scattering coefficient, which is also shown in Figure 8.18 and shows good agreement with the measured values.

Being satisfied that the spheres were behaving sensibly in liquid styrene, the next move was to try to suspended them in the polyester resin. A measured mass of spheres was added to a quantity of the liquid resin and suspended using the ultrasonic bath and a stirring rod. The resin was then cast. The scattering coefficient of the cast resin containing the spheres was measured on two separate samples using the collimated system as described in section 8.4.

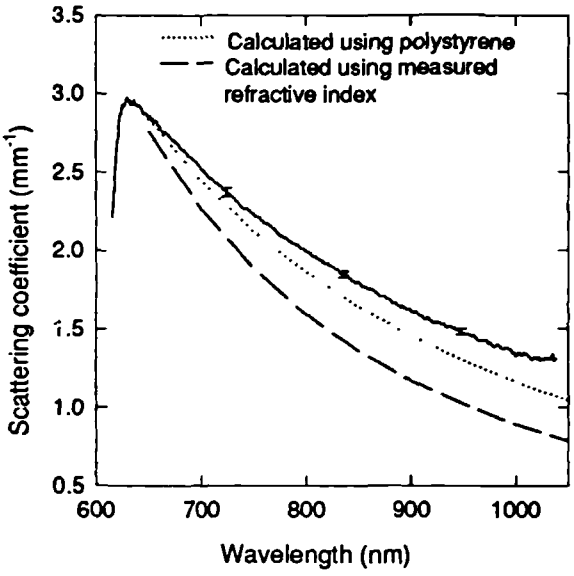

Figure 8.19 The measured scattering coefficient of the spheres suspended in solid resin. Also the scattering coefficient calculated using the empirical refractive index and that of polystyrene.

One problem encountered in calculating the scattering coefficient of the spheres in the

resin is the small fluctuations in the refractive index which were mentioned earlier (section 8.3). The refractive index shown in section 8.4.4 is the average through a large block, but the scattering coefficient depends only upon the refractive index of the medium immediately surrounding the spheres. The liquid resin is a mixture of polyester dissolved in styrene monomer. As suggested in 8.3, it would seem that these fluctuations are caused by the two polymers separating. If the spheres are preferentially surrounded by polystyrene, the scattering coefficient will be higher than if this is not the case. Unfortunately, the refractive index of polystyrene varies depending upon the exact degree of polymerisation. Figure 8.19 shows the measured scattering coefficient in comparison to the scattering coefficient calculated with Mie theory using the overall refractive index for the polymer and also using the refractive index for polystyrene taken from the literature[113]. The latter shows a better agreement with the measured data, though neither is a very good fit. The discrepancy can be explained if the refractive index of the surrounding medium is greater than that used in the calculation, or if a portion (~10 %) of the spheres are clumped together.

8.4.6.2 Angular scattering function

The angular scattering function of the silica spheres was also measured using the goniometer. The scattered intensity as a function of angle at 800 nm is shown in Figure 8.20. Also shown is the angular scattering function predicted by Mie Theory using the refractive index of polystyrene. There is a good agreement between the calculated and

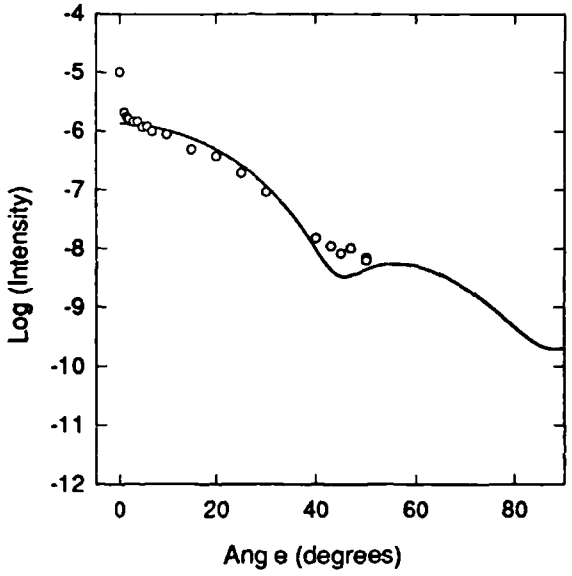

Figure 8.20 Scattering phase function at 800 nm in comparison with calculations. Symbol: measured points. Solid line: theory

measured data. Only the first 60° of the phase function were measured, due to the exponentially dropping light intensity. To calculate g, the phase function was extrapolated out to 180°, using the log slope of the data. The value of g at 800 nm was calculated as 0.935. The error in g from incorrect extrapolation was estimated by calculating g using two different slopes for comparison. Using a slope twice as steep gave a g value of 0.942, and using a slope half as steep a g of 0.916. Hence, the maximum error expected from incorrect extrapolation is +0.006, -0.02. The wavelength dependence of g is shown in Figure 8.21 in comparison with the value calculated from Mie theory using the refractive index for polystyrene.

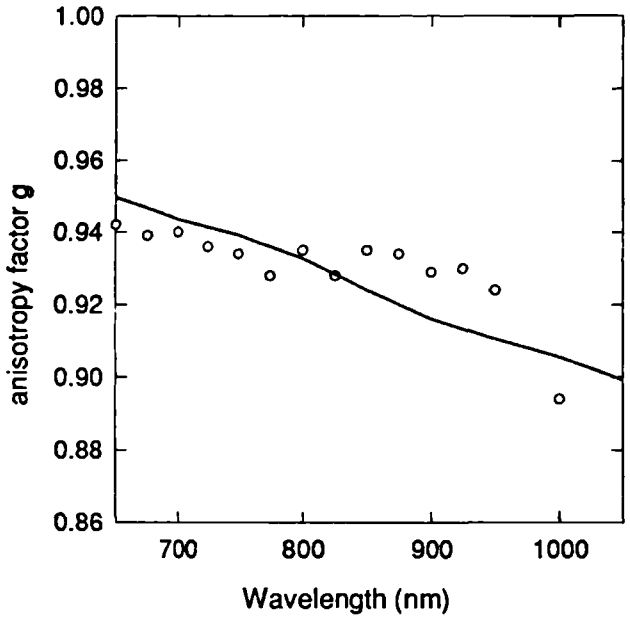

Figure 8.21 Anisotropy factor g as determined from the measured phase function. Solid line is theoretical value.

Chapter 9

Phantom application for spectroscopy and imaging

9.1 Introduction

This chapter describes the three major applications for which the phantom material has been used to date. The first of these was to investigate the accuracy of different methods for measuring the optical properties of tissue.

Secondly, a phantom was designed for use in calibrating NIR spectrometers. This provides a diffusing block with variable overall attenuation. It can be used to verify attenuation measurements of diffuse transmission and reflection made by spectrometers.

Finally, the material has been used to make phantoms for investigating imaging in scattering systems. The work involved in the development of the phantom for each of these applications and the associated problems are discussed in turn.

9.2 Comparison of methods for measuring optical properties

This section describes the use of the phantom material to compare different methods for measuring the optical properties of scattering materials.

The measurements of the scattering and absorption coefficients described in chapter 8 have been assumed to be accurate. These were measurements of the average scattering and absorption coefficients of the material as a function of the concentration of scatterer/dye present. To calculate the actual coefficients presented in this section, these average values per unit concentration have been multiplied by the quantity of scatterer/dye present in the particular phantom materials.

Using these coefficients, the phantom material was used to compare the two

other systems for measuring μ_a and μ_s described in chapter 6. The first of these was the integrating sphere system, which measures the diffusely transmitted and reflected light through a thin slab of material and uses a Monte Carlo model to derive the optical coefficients. The second method measures the temporal broadening of a short pulse of light through a thick slab of the material. The optical coefficients of the material can be calculated by fitting the experimental data to the time dependant diffusion equation.

One point to bear in mind is that the e latter two systems measure the *transport* scattering coefficient, whilst the measurement of collimated unscattered light gives the true scattering coefficient. Comparison between the systems is therefore somewhat hampered by the accuracy to which the angular scattering function is known. In this comparison, the value for g calculated using the measured particle size distribution and refractive index was used. Absorption coefficients can be directly compared.

9.3 Integrating spheres

The integrating sphere system was used to measure the absorption and scattering coefficients of a number of samples of the phantom material. At 800nm, these samples had a range of absorption coefficient from 0 001 mm^{-1} (no dye added to the phantom) to 0.3 mm^{-1} (dye used was Projet 900 NP - see section 8.4.3). The scattering coefficient ranged from 3 to 25mm^{-1}. There was no fixed relationship between the amount of scattering and absorption present in the samples. Measurements were performed on phantoms made with both titanium dioxide and amorphous silica as scattering particles.

9.3.1 Absorption coefficient

The comparison between the absorption coefficient measured at 800 nm with the collimated light system and the integrating sphere system is shown in Figure 9.1. The straight line regression for this graph gives a slope of 0.97 and an intercept of 0.014, ie the integrating sphere method overestimates μ_a by a small amount. The integrating spheres can probably be considered as giving an accurate estimation of the absorption coefficient at high values but overestimating μ_a at low absorptions. Unfortunately, in

the near infra red, the absorption coefficient of tissue is approximately of this magnitude (typically 0.01-0.08 mm^{-1} see section 5.4). This means that data previously measured with the integrating sphere method (van der Zee[94] and the bone measurements in section 7.1) will have overestimated the true absorption coefficient. It is also likely that data from other authors[104,93,103] who have used this technique will contain similar errors, since, as can be seen from chapter 8, we have tried, as far as possible to make accurate measurements.

Some error is perhaps to be expected in determining μ_a values of such low magnitude, as they correspond to an absorption length of 5 to 10 cm. This is much longer than the average photon path length through a 2.5 mm sample. Whilst the absolute measurement

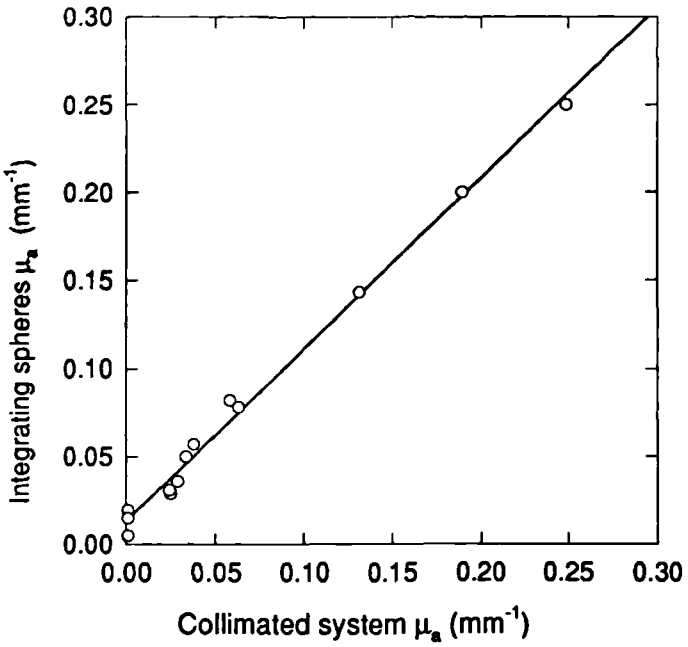

Figure 9.1 Comparison of μ_a measured using integrating spheres and by the collimated system measurements. A total of 13 samples used. The regression line has an intercept of 0.014 and a slope of 0.97

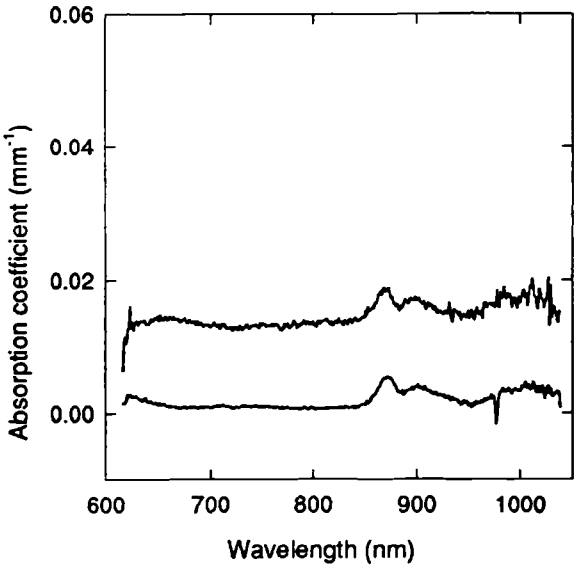

Figure 9.2 Wavelength variation of the μ_a. The upper curve shows the average μ_a of 3 samples measured by the integrating spheres. The lower data is μ_a measured with the collimated system.

of μ_a is not exact, the variation of absorption coefficient with wavelength is reasonably accurate. This is demonstrated in Figure 9.2, which shows the average μ_a of the resin measured on 3 scatttering samples with the integrating spheres. The absorption coefficient of the resin measured on clear samples with the collimated system is also shown. Figure 9.3 shows the difference between the two spectra. As can be seen this is fairly flat with a fluctuation of ~±0.001 mm^{-1} over the whole 600 to 100 nm range.

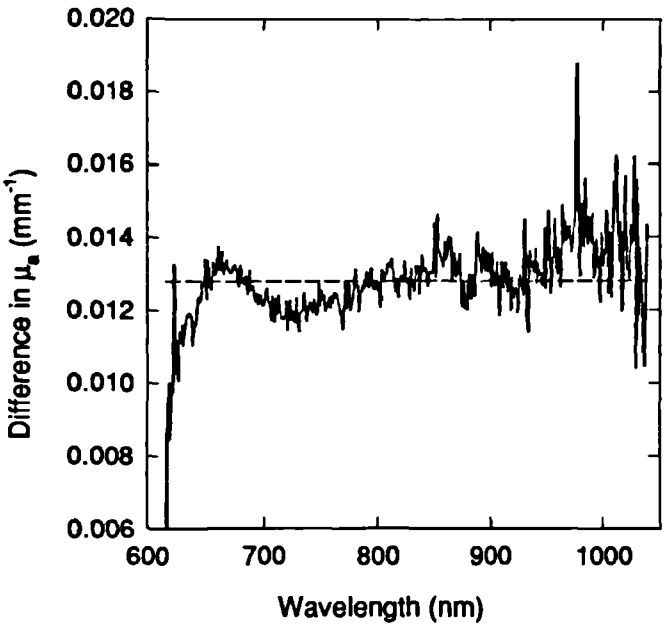

Figure 9.3 Difference between the integrating sphere μ_a and collimated system μ_a. Dotted line is the average difference.

9.3.2 Scattering coefficient

The Scattering coefficient was measured with the integrating spheres on samples containing both TiO_2 and amorphous silica as scattering particles. The Monte Carlo simulation which is used in the data analysis can include a scattering phase function to determine the angle through which the photons are scattered. For both scatterers, the simulation used the scattering function calculated at 800 nm from Mie theory from the measured size distribution (see chapter 8). As the same g value is used for the whole wavelength range, to calculate the correct transport scattering coefficent, a factor $(1-g_m)$ is used, g_m being the value of g used. To calculate the scattering coefficient from this, μ_s' should be divided by (1-g), g being the correct value for the particular wavelength.

The comparison of scattering coefficient is shown in Figure 9.4 for the titanium dioxide spheres and in Figure 9.5 for the silica particles. As can be seen there is a fairly good agreement between the two methods for both the amorphous silica and the titanium

dioxide scatterers. The integrating sphere technique does appear to under estimate the scattering coefficient by ~10 %. This may be due just to an inaccurate g value. For the TiO_2 particles, if we use the g value which was calculated using the best fit of theoretical μ_s to the measured μ_s (see section 8.4.2) a much better agreement between the integrating sphere and collimated data is obtained, the regression slope being 0.96 and the intercept 0.52.

Figure 9.6 shows the variation of the measured scattering coefficient with wavelength for the TiO_2 particles and Figure 9.7 for the silica particles.

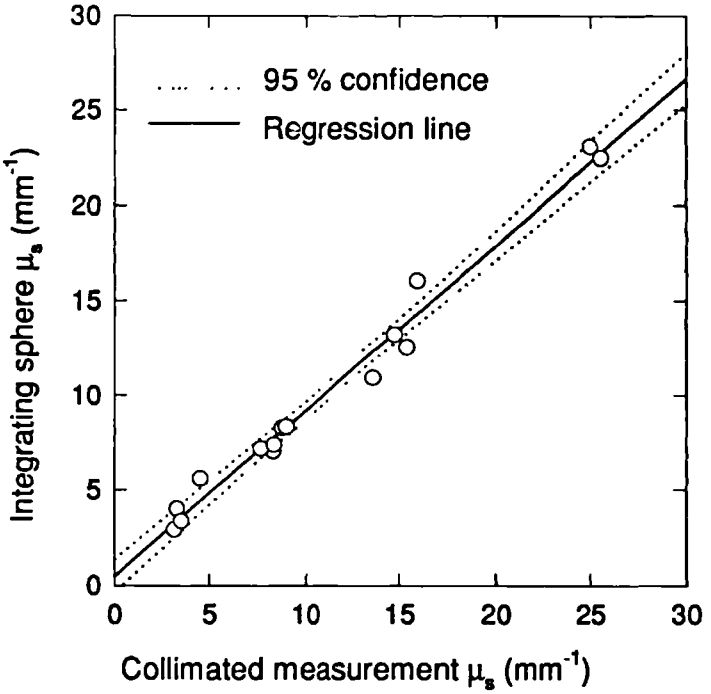

Figure 9.4 μ_s of TiO_2 suspension measured on 15 samples with integrating spheres compared with that calculated from collimated system data. The regression line shown has a slope of 0.87 and an intercept of 0.47

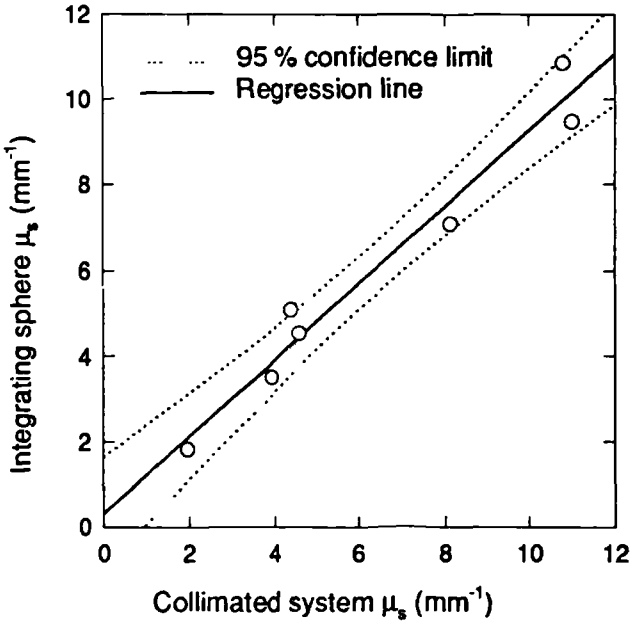

Figure 9.5 μ_s of silica sphere suspensions measured on 7 samples with the integrating spheres plotted against the calculated values. The regression line has a slope of 0.9 and an intercept of 0.32 mm^{-1}.

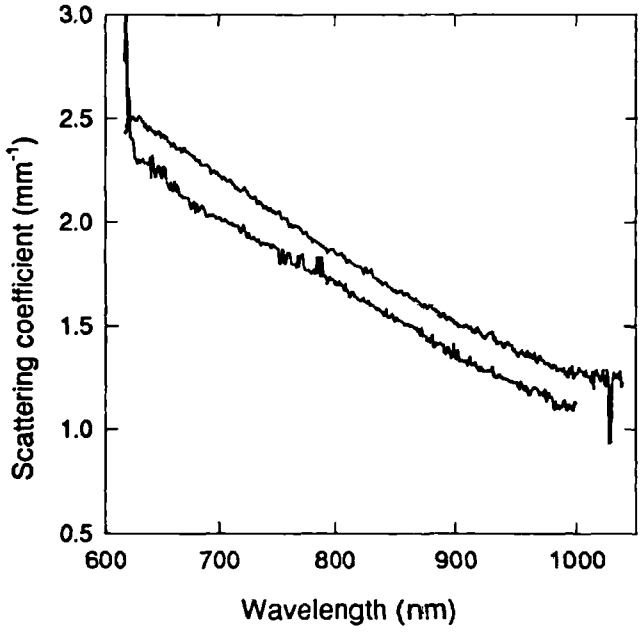

Figure 9.6 Scattering coefficient vs wavelength for TiO_2 particles from integrating sphere data (lower curve) and collimated system.

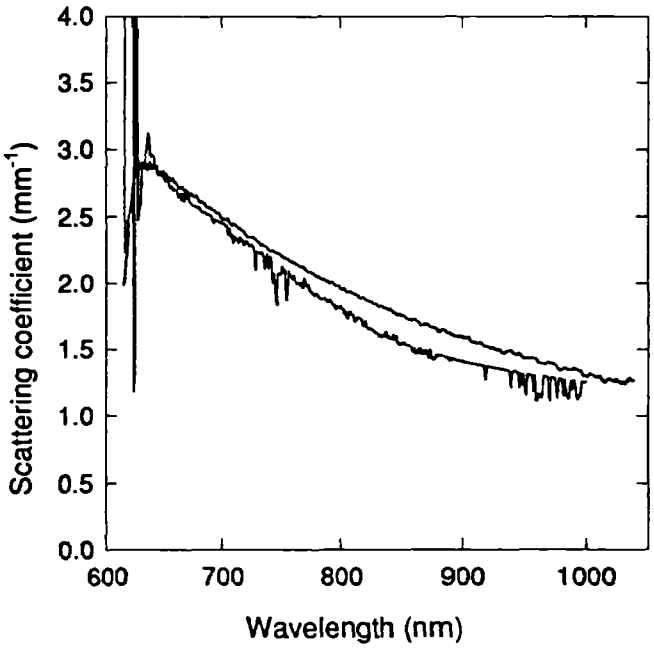

Figure 9.7 Scattering coefficient vs. wavelength for integrating sphere data (lower curve) and collimated system for silica particles

9.4 Diffusion theory fit

In order to compare the bulk properties of the phantom with calculations from diffusion theory, three large slabs of material were used. These differed in their thicknesses from 5 cm to 2 cm. They were all approximately 7 cm high and 10 cm wide.

The temporal spread of a short pulse of light transmitted through the slabs (at 800 nm) was measured as described in section 6.5 and the scattering and absorption coefficients were calculated from the best fit of the data to the time dependant diffusion theory for an infinite slab. Figure 9.8 shows the comparison between the measured scattering coefficients and the expected value, while Figure 9.9 shows the absorption coefficients. As can be seen there is a

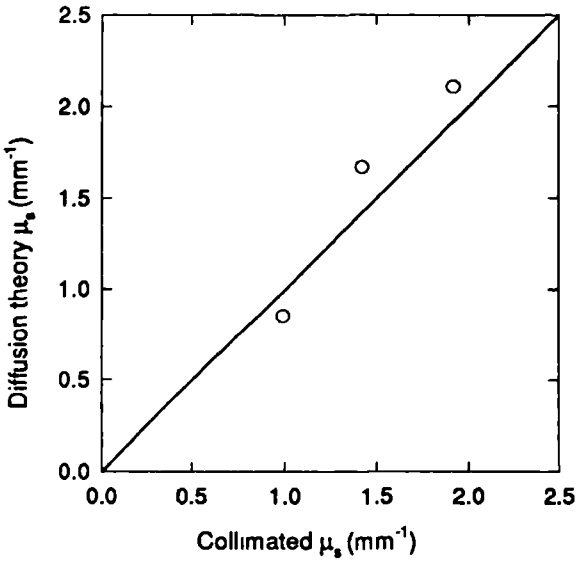

Figure 9.8 Scattering coefficient as measured using the diffusion approximation fit to the TPSF vs collimated measurements. The solid line is the unity line, not a regression.

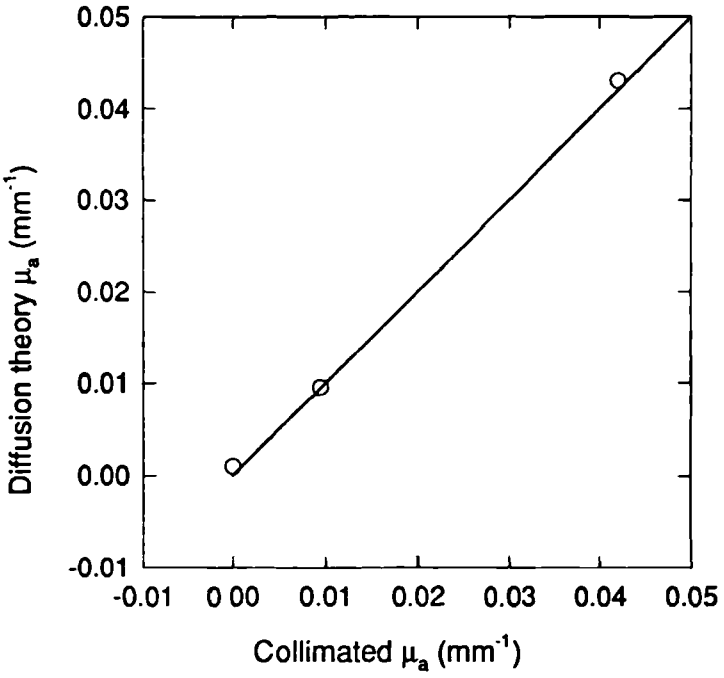

Figure 9.9 Absorption coefficient as measured using diffusion approximation fit to the TPSF. Unity line shown.

good agreement for the scattering coeffic ents, and a very good agreement for the absorption coefficients. The larger variation for the scattering coefficient may be caused by inadequate mixing of the scattering particles.

9.5 Spectroscopy phantom

With the increased clinical use of NIR spectrometers, there is a growing need for a simple means of periodically verifying the spectrometer's attenuation measurements and instrumental drift. This requires a standard calibrated phantom against which attenuation measurement can be compared.

The phantom must have an overall attenuation of approximately 6 optical densities (OD), variable in known amounts over about 3 OD. This will cover the physiologically feasible range of OD change, which is about 1 OD variation on a particular patient, but with a wider range of attenuation between different patients, depending on tissue type and interoptode spacing. The standard should ideally have a basic spectral attenuation over the NIR range which is similar to that of tissue, but the adjustable variation in attenuation should ideally have no wavelength dependence. The phantom should diffuse the light from the optodes so that the positioning of the fibres on the phantom does not significantly affect the measurements. A brief description of the phantom has been published[14]. This description is given in more detail here, along with some experimental results.

9.5 1 Design of the phantom

The spectroscopy phantom (see Figure 9 10) is made of an opaque black plastic assembly, glued between two blocks of phantom material. For this particular phantom, the transport scattering length is 3 mm. The dimensions of the blocks are shown in Figure 9.10.

The assembly between the two blocks of resin is made from two sheets of black PVC (each 4.5 mm thick) with a groove cut in each. These are bonded together to form a slab containing a slot 4.5 mm wide by 13mm high, in which a further piece of plastic

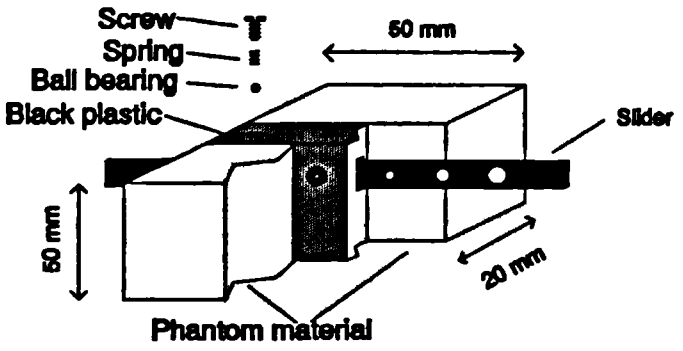

Figure 9.10 Phantom for use in calibrating spectroscopy instruments.

can slide. There is a 10mm diameter hole drilled in the slab through the slot, and light can travel through this from one side to the other. The sliding plastic section (also made of the black PVC) is rectangular, being 20 cm long, and 4.5 by 13 mm in cross section. There are nine holes drilled through the plastic, and as it is slid along in the slot, each hole in turn is aligned with the centre of the 10mm hole in the slab. The holes vary from 8-1 mm in diameter. On the top edge of the sliding section are a series of grooves into which a spring loaded ball bearing fits. This serves to accurately locate the holes in the slider with the hole in the slab. As the slider is moved, the size of hole between the two slabs of diffusing material changes, and hence the optical attenuation across the phantom is altered. The advantage of the design is that the attenuation change is wavelength independent, providing that the diffraction limit is not reached.

9.5.2 Modus operandi

Under diffuse illumination, the intensity of light transmitted through the central hole is dependant on its diameter. In a very thin sheet, the intensity of the light transmitted would vary simply in proportion to the area of the hole. In this case, however, the material has a significant thickness in comparison to the hole diameter, so that for a hole of given

Figure 9.11 Showing cut out view of slider hole and holder.

diameter, the intensity of the light transmitted is proportional to the solid angle of the hole. The solid angle is equal to the sine of the half angle, θ of the hole (see Figure 9.11). The relative intensity I/I_r between two holes of different diameter is hence given by

$$\log(I/I_r) = \log\left(\frac{\sin(\theta)}{\sin(\theta_r)}\right) + \log\left(\frac{R^2}{R_r^2}\right) \qquad (9.1)$$

where R is the radius of the hole, and the subscript r refers to the reference hole.

The fibres of the NIR spectrometer can either be placed on opposite faces of the phantom, or both on the top face, with one fibre on either side of the black plastic assembly. This latter arrangement suits NIR instruments whose optodes are attached together with a fixed separation between them. The optodes should ideally be clamped in position, especially when performing long term stability tests.

The phantom is painted black, except for the regions where the optodes are attached, in order to help shield the whole assembly from ambient light. The phantom should also be covered with black cloth once the fibres have been attached.

9.5.3 Measurements and results

To calibrate the phantom, light from a 150W halogen lamp was shone onto one face of the phantom via a fibre optic bundle, and the light on the other side collected by a second optical fibre connected to the CCD detector (see section 6.2). Measurements of the transmitted intensity are made over the range 750-1000 nm. The fibres were clamped in place against the phantom to prevent movement artifacts. Measurements of transmitted intensity were made with each of the holes in position and the results normalised to the intensity measured through the largest hole.

Figure 9.12 shows the overall attenuation through the phantom, with the 8mm hole in position, together with the wavelength dependence of the relative attenuation between the 8 and 6 mm diameter holes. Figure 9.13 shows the relative attenuation (averaged between 800 and 850 nm) versus the hole diameter. Also shown is the variation in attenuation calculated using equation (9.1).

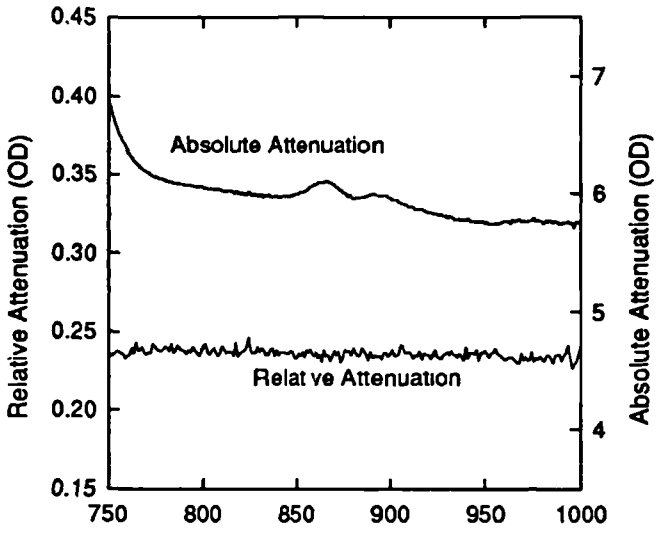

Figure 9.12 Variation of attenuation with wavelength for the calibration phantom 8 mm hole, plus the attenuation difference between 6 and 8 mm holes.

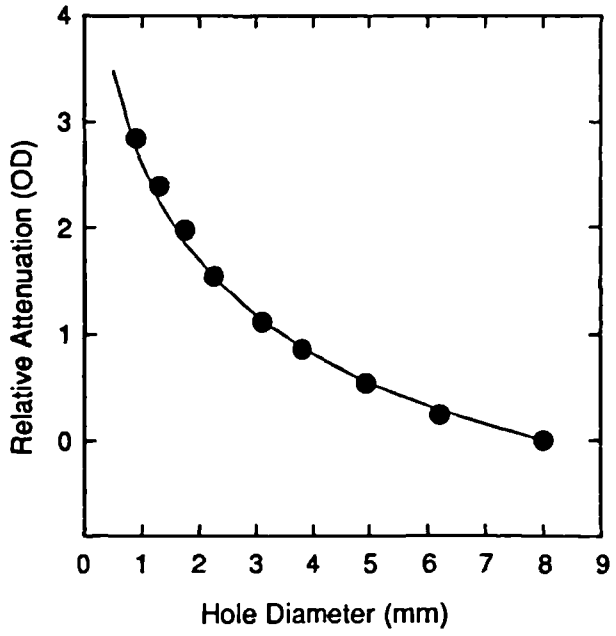

Figure 9.13 Showing the variation of attenuation with hole diameter for the spectroscopy phantom. Solid line is the caluculated values from equation (9.1).

To test the usage of the phantom and the repeatability of the attenuation changes, measurements were made by two NIR spectrometers (NIRO 500 Hamamatsu, Japan) of the diffuse transmission through the phantom. The measured intensities were averaged over 1 minute for each hole. The results of this test are shown in Figure 9.14 which shows the difference between the calibrated and measured values for the four different laser wavelengths in the machine. There is approximately a ± 0.02 OD variability on the first 7 holes. The values for the last two holes are dominated by noise (~ ± 0.2 OD), due to the low levels of light detected (8-9 OD attenuation).

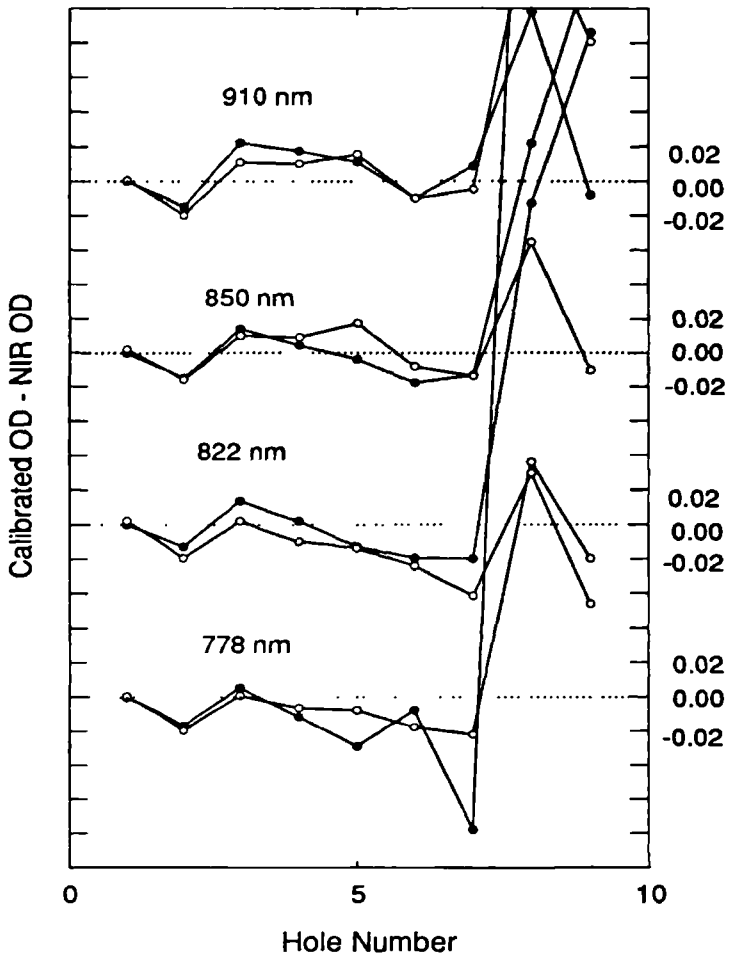

Figure 9.14 Difference in attenuation measurements made with two NIR spectrometers compared against the calibrated values. The four laser wavelengths are shown.

The phantom provides an easy and reproducible method of verifying the accuracy and stability of relative intensity measurements of near infra red spectrometers. The attenuation change it produces is wavelength independent, and covers a range from 6 to 9 OD. The relative attenuation measurements are not susceptible to change with time, as they depend solely on the size of the holes in the filter and the phantom can hence be used for long term stability tests.

9.6 Phantoms for imaging

For investigating imaging, phantoms are needed which include inhomogeneities. These can differ in either their absorption and/or scattering properties. The effect of position, contrast and size of inhomogeneity upon the image resolution need to be investigated.

Imaging phantoms were made in one of two different geometries. The first was a cylinder of 5.4 cm in diameter. Martin Schweiger, who is currently completing a PhD in this department on image reconstruction using infra red light used this phantom to obtain experimental data[138,139]. The phantom had a 5 mm diameter cylinder inserted through it as an object to image (see Figure 9.15). The main cylinder had a μ_s' of 1.7 mm^{-1} and a μ_a of 0.02 mm^{-1}, and the image cylinder 5 times the absorption, but the same scattering coefficient. Different rods could be used if required (see next section).

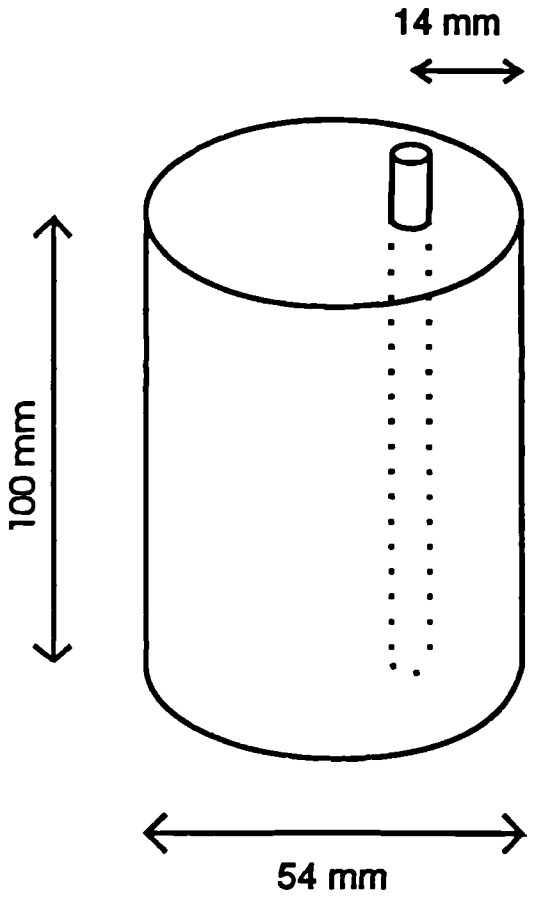

Figure 9.15 Cylindrical phantom with single inhomogeneity used to test NIR image reconstruction algorithms.

A slab geometry was used to construct phantoms to investigate

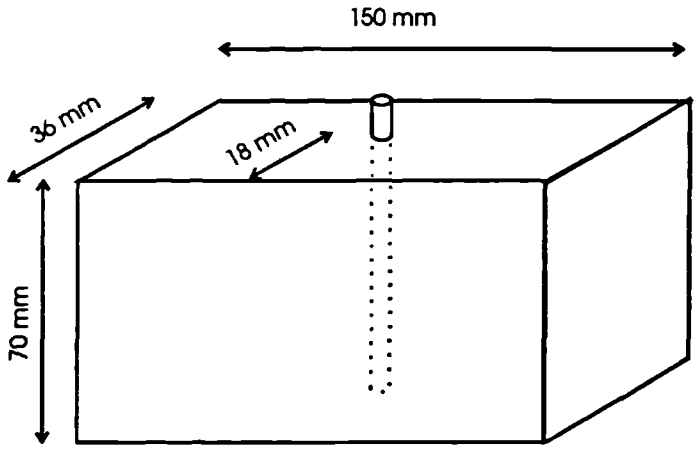

Figure 9.16 Slab phantom.

imaging in the female breast. For breast imaging with infra red light, the breast can be compressed, (similarly to X ray mammography) approximately forming a slab. This phantom also had cylinders inserted in it with different optical properties to the slab. It was made for work currently being carried out in this department by Jeremy Hebden and David Hall of the department.

To create these inhomogeneities, one of two approaches can be used. The first is to cast the phantom in two or more stages, casting the image objects inside of the phantom. This produces a phantom with permanent inhomogeneities. One technical problem with this method is that the resin undergoes shrinkage as it cures. If care is not taken, the two parts of the phantom may shrink away from each other, leaving an air gap. The second approach, which was used to make the two phantoms described above, is to make the phantom in separate pieces. This has the advantage that several different image objects can be used in the same phantom. The disadvantage is that some coupling liquid must be used to fill the gap between the different parts, and this may effect the light distribution. Ethyl cinnamate was used in this work (see section 8.3.1).

9.6.1 The effect of coupling liquid

To investigate the effect of a thin layer of ethyl cinnamate around the image objects, two slab phantoms were made, one with a μ_s' of 1.67 mm^{-1}, μ_a of 0.04 mm^{-1} and a thickness of 36 mm, and another with μ_s' of 2 mm^{-1}, and μ_a of 0.001 mm^{-1} with a thickness of 25 mm. The first one was made with properties similar to tissue as a typical phantom for imaging. The second was made as a phantom in which any effects of the coupling liquid would be most evident.

A hole of 7 mm in diameter was drilled in the first slab, and one of 8mm in the second. The holes were positioned centrally in the phantom. Rods with the same optical properties as the slabs were made. For the first phantom, the rod was made to just fit inside the hole, with a diameter of 6.9 mm. For the second slab, two rods were made, one 7.9 mm in diameter (to just fit inside the hole), and the other 7 mm. This was to investigate the effect of a having a thicker layer of matching fluid.

The slabs were illuminated with 800 nm picosecond pulses from a Ti Sapphire laser (see section 6.5), the laser beam being scanned across the slab, co-linearly with the

detector. The mean time of flight through the slab was determined together with the intensity integrated over the whole pulse width. Figure 9.17 shows the variation in mean time and intensity through the first phantom, and Figure 9.18 the second phantom.

For the first, more realistic phantom, there is a small (~2 %) dip in the mean time over the position of the rod although this is largely masked by noise. The integrated intensity shows no significant variation over the range scanned. In the second phantom, the presence of the rod is apparent in both cases, with approximately a 1 % total dip in the mean time for the 7.9 mm rod. Rod 2, which has a thicker layer of fluid around it (as the rod is smaller) produces a larger (~3%) change in the mean time. The integrated intensity,

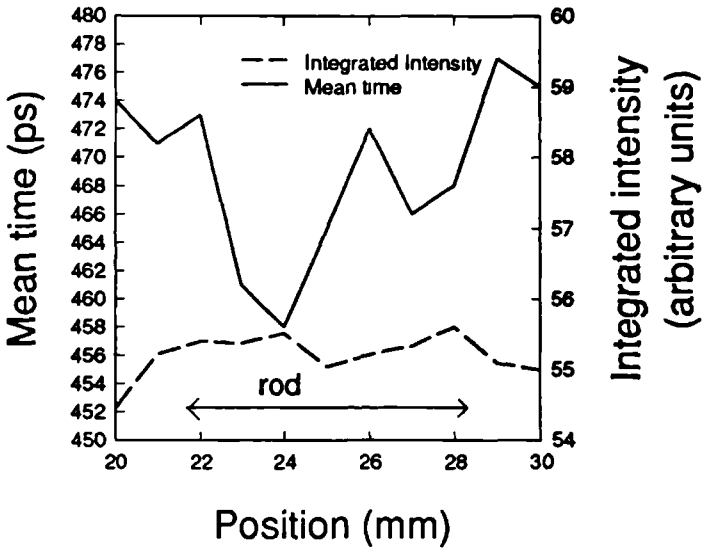

Figure 9.17 Mean time and integrated intensity along slab phantom. Rod of diameter 7 mm with same optical properties as slab located at 25 mm.

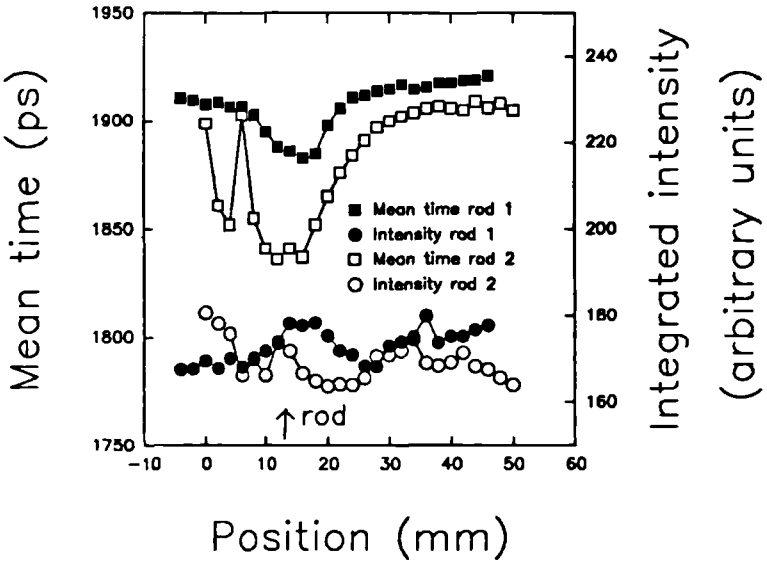

Figure 9.18 Mean time and integrated intensity scanned across a slab. A rod is in an 8 mm diameter hole through the slab, at position 12 mm. Rod 1 is 7.9 mm in diameter and rod 2 is 7 mm.

however does not show a change.

9.6.2 Preliminary imaging experiment

In the first phantom, as an initial imaging experiment, a further two holes of 7 mm in diamter were drilled in the phantom, and these were filled with rods having different optical properties. The optical properties of the rods and the phantom are shown in the following table

	μ_a mm^{-1}	μ_s' mm^{-1}	Position (mm)
rod 1	0.04	16.7	13
rod 2	0.4	16.7	27
rod 3	0.4	1.67	41
phantom	0.04	1.67	

The mean time of flight and integrated intensity were measured along the phantom, and are shown in Figure 9.19. The position of all three rods is clearly apparent, both in the mean time and the intensity data. It is not immediately apparent, however, how to determine the optical properties of the inhomogeneities from this data alone, although further analysis of the shape of the TPSF (temporal point spread function) would hopefully enable this.

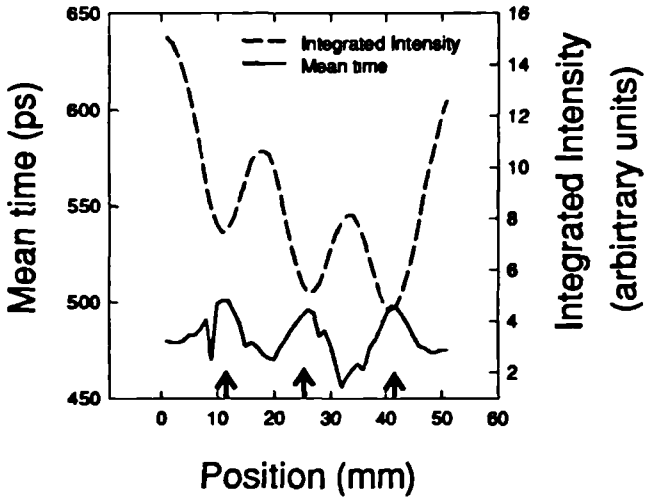

Figure 9.19 Mean time and integrated intensity across a slab with three rods through it. Rod 1 is on the left, rod 2 the middle and rod 3 on the right.

Martin Schweiger[139] made measurements of the TPSF as a function of source detector separation and position around the cylindrical phantom described in the previous section. To reconstruct an image of the phantom he used algorithms discussed in section 2.3.4 using the FEM solution to the diffusion equation. As parameters he used the mean time of flight <t> together with 6 higher moments of the TPSF (mean of higher powers of t, $\langle t^n \rangle$ where n>1). The resulting image of the absorption coefficient is shown in Figure 9.20.

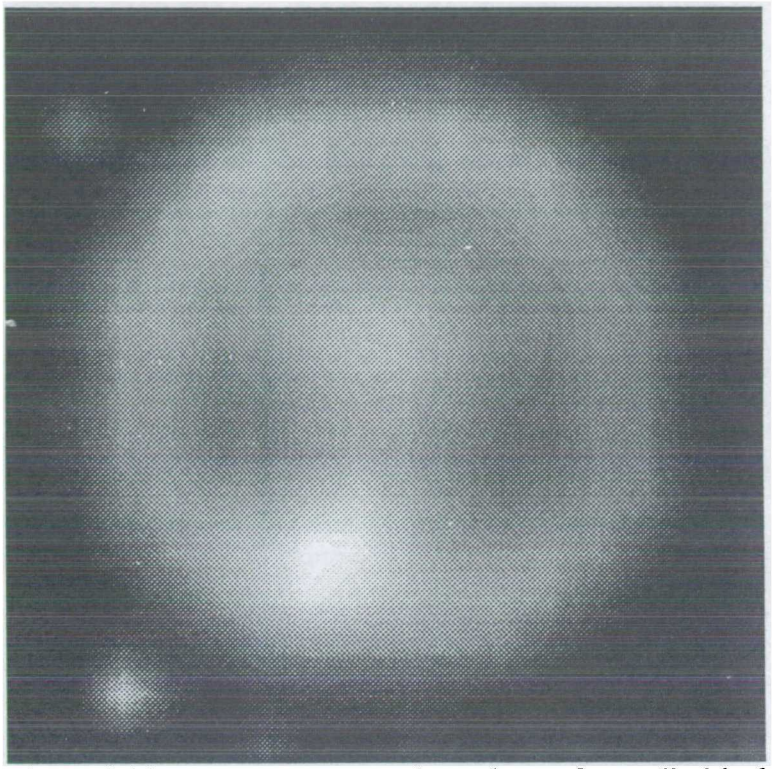

Figure 9.20 Image reconstruction of μ_a of a cylindrical phantom 54 mm in diameter. There is a 5mm diamter rod with 5 times the background μ_a positioned 14 mm from the bottom.

The rod is correctly positioned in the image, although the absolute values of μ_a were not accurately found.

Chapter 10

Discussion and further work

10.1 Phantom material

This thesis has shown the potential of the solid phantom for use in near infra red spectroscopy and imaging. The phantom is stable and reproducible and its optical properties can either be predicted or measured to an acceptable accuracy. There is, however, room for improvement.

Work is currently being started to investigate the use of epoxy resin instead of polyester as a base material for the phantom. Using this it is hoped that the problems caused by fluctuations in the refractive index of the clear phantom can be avoided. In the polyester phantom, these fluctuations were thought to by caused by the two polymers (polyester & polystyrene) separating out. As the epoxy is a single polymer, such a separation should not occur, and provided that the epoxy resin and hardener are thoroughly mixed, a clear plastic should be formed. The epoxy resin that we are looking at also has the advantage that it undergoes very little shrinkage and generates little exothermic heat as it sets. This will enable large phantoms to be cast in one go. The epoxy is stable once set, and offers good resistance to chemical attack. It can also be machined easily.

Initial experiments performed so far on the epoxy indicate that it has a similar refractive index to the polyester (ie 1.59 - 1.56). The absorption coefficient of the resin is estimated to be low - preliminary experiments show μ_a <0.01 mm^{-1}. The dye used with the polyester resin (PROJET 900 NP) is soluble in the epoxy resin, and its absorption spectrum is the same in solid epoxy as in solution. The amorphous silica spheres can be suspended quite easily in the epoxy resin, and will give a g value of

~0.9-0.95. The resin appears to be sufficiently viscous to prevent settling of the spheres as the resin sets.

There is also scope for investigating different dyes for use in the phantom, with the aim of matching the absorption spectra of tissue. If the absorption spectra of the different components in tissue (haemoglobin, cytochrome and water) could be matched, realistic phantoms could be made which allow the investigation of wavelength variations of attenuation.

10.2 Spectroscopy phantom

The spectroscopy phantom described in the thesis provides an adequate means of making measurements of overall attenuation by spectrometers. This is useful for comparing the accuracy of different instruments, and for performing periodic and long term stability tests.

There is also a need for a phantom which could be used to compare the algorithms of different machines, ie their calculation of haemoglobin concentration etc. In order to do this a phantom would be needed which matched the attenuation spectrum of tissue. Changes in attenuation would also need to be spectrally similar to those likely in tissue.

A phantom to do this can be envisaged as a three layer system, resembling the spectroscopy phantom presented in chapter 9. The two outer layers would have scattering and absorption similar to tissue and the two optical fibres from the spectrometer would be attached to these two outer layers. The middle layer would be moveable, probably sliding along, and would have the same scattering properties as the rest of the phantom, but a variety of realistic absorptions. These differences in absorption introduced by the central sliding layer could match changes in tissue, for example a change from deoxy Hb to oxy Hb.

To create such a phantom, dyes would be needed which could be used to match the absorption spectra of the components of tissue (Hb, HbO_2, cyt, water). A match at all wavelengths is not required, but the spectra would need to match at the wavelengths used by the spectrometers.

10.3 Imaging phantoms

To investigate imaging with near infra-red light, inhomogeneous phantom are needed. For an accurate appraisal of the imaging technique, the phantoms used to generate the image must have well known properties. The inhomogeneities must be at well defined locations, and have known size, so that the accuracy to which they can be positioned on an image can be investigated. The optical properties of the phantom and its inhomogeneities must be known so that the effects of object contrast can be investigated. Other than the required inhomogeneities, the phantom should be homogeneous.

The introduction of inhomogeneities into a phantom can present certain problems. Measurements described in section 9.6.1 indicate that any clear gap between the bulk and the image object will have an effect upon the light distribution. Even small gaps are likely to change the distribution. This emphasises the problems associated with using liquid phantoms with clear regions (such as test tubes) around image objects. The implication of this 'light piping' around clear layers is that image objects should ideally be embedded inside of phantoms.

The shrinkage occurring with the polyester phantom is probably too great for objects to be reliably embedded without shrinkage from them. The use of epoxy resin to embed objects inside of bulk phantoms is currently being investigated. Amorphous silica can be mixed into the epoxy to provide scattering which matches that of the bulk phantom. This can then be used to glue image objects in place. To test this technique, clear objects were glued inside of clear phantoms. No shrinkage of the glue was observed, and the join was almost invisible. Provided that the scattering coefficient of the glue matches the rest of the phantom, this is a good way of embedding objects.

To verify that objects have been successfully embedded, it would be useful to also embed an object of the same properties as the bulk phantom. If this cannot be subsequently detected, then the embedding can be considered as being effectively invisible insofar as the imaging system being used is concerned.

The scans shown in 9.6.1 show that under suitable circumstances, thin non scattering regions can be detected. This does offer hope for the potential of imaging techniques, since as sub-millimetre layers of clear fluid can be detected, it would seem likely that larger objects with lower contrast will be visible.

10.4 Measurements of the optical properties of tissue

It would seem that the determination of optical properties of materials using the integrating spheres to make measurements on thin samples is likely to lead to inaccurate estimates of the absorption coefficient. In our case the absorption coefficient is apparently overestimated. This finding is also supported by recent research done with tissues by Torres et al[140] and Graaff et al [141]. The latter report also noted that values of the scattering coefficient measured *in vivo* were lower than those measured *in vitro*.

Fitting measurements of the TPSF of transmitted light to the diffusion theory would appear from the testing performed in section 9.4, to be a more accurate method of measuring coefficients for large samples. Other authors have suggested this, showing that provided the sample is suitably large, estimates of μ_s and μ_a to 10 % accuracy can be obtained (Farrell et al[142] and Madsen et al[108]). The latter authors did find that for samples less than ~4 cm in diameter significant errors occurred. The technique can be used *in vivo*, but not easily, since the equipment is bulky and not portable. A version of this technique which measures the spatial distribution of the reflected light is more suitable for *in vivo* use. Unfortunately, this is susceptible to errors caused by fluctuations in the received intensity. These can be caused by variations in the surface absorption or by variations in the coupling of the light to the detector. Using liquid phantoms, Groenhuis et al 107 investigated the technique and found a deviation of ± 30 %, while Splinter et al[143] found error of ±15 %. Again, the technique is not suitable for small geometries. The inaccuracy in measuring on small samples means that these two techniques can only be used to measure bulk optical properties and cannot be used to find optical properties of individual tissues in general.

The phantom could be used to test the measurements made by other systems, including the use of different methods of analysing the integrating sphere measurements of reflection/transmission. For systems such as the integrating spheres, where there is a systematic error, the phantom could be used to determine this and hence enable a better estimate of optical coefficients to be made.

In order to fully investigate the accuracy of systems for measuring optical properties of materials, we need to have a fully calibrated phantom. While the scattering and absorption coefficients of the phantom described in this thesis have been accurately measured, its phase function is subject to some uncertainty. This means that in the

analysis of the scattering coefficient measurements by other systems, it would not be possible to know if a discrepancy was due to the system being investigated or a lack of precision in the measurement of g. Again, this problem may be solved by usage of epoxy resin together with the amorphous silica spheres, where the value of g should be calculable.

Conclusions

This thesis has presented work concerning the measurement of the optical properties of tissues and other scattering substances and the development of stable and reproducible tissue equivalent phantom materials. Several contributions to this field have been made as part of this work and have been presented in this thesis. These include:

The development of a stable and reproducible phantom which can match the optical properties of tissue. Two different materials were investigated as scattering particles for use in the phantom. Initially, TiO_2 was used, but the g value of this is somewhat low compared with tissue. To give a better g value, silica spheres were then tried. Using the silica spheres, the theoretical scattering coefficient can be predicted, and this was found to be in good agreement with the measured value.

A system was constructed for directly measuring the absorption and scattering coefficients of materials using a collimated light source and detector. The system was tested using aqueous suspensions of polystyrene particles, and was then used to measure the optical coefficients of a range of phantom materials.

The dual integrating sphere method for simultaneously measuring μ_a and μ_s' has been improved by increasing the degree of collimation of the input light source. This improved the measurement of low values of reflectance from 10 to 4% accuracy. The modelling of the light distribution inside the integrating spheres has been improved to more accurately match the actual system, with the incorporation of specular reflections from the sample, and of the incident light which hits the sphere walls. The internal surface area of the integrating spheres was also accurately measured, further improving the accuracy of the calculations.

The dual integrating sphere technique was then calibrated using the phantom material, and it was found that the method consistently overestimates the absorption coefficient (by approximately 0.015 mm^{-1}), and that the measurement of scattering coefficient is reasonably accurate (to within 10 %).

I measured the optical properties of skull using this technique, since no values could be found in the literature. These measurements were made on sections of excised

skull from six adult pigs. The value for μ_s' was found to be in the range 1.5 to 2.5 mm^{-1}, and μ_a 0.01-0.02 mm^{-1}. The anisotropy factor, g was found to be in the range 0.92-0.94.

The goniometer system for measuring scattering phase functions was improved by increasing the degree of collimation of the detection telescope, which reduced the inherent system response from 8° to 2°. The goniometer was then tested and validated from measurements made over the first 50° using the phantom material with scattering silica particles, whose angular scattering properties could be predicted. For this phantom, whose g value was approximately 0.93, the system was found to give g to ±0.02.

Using the phantom material, a device was designed and constructed which enabled the calibration of near infra spectrometers. This provided a range of calibrated attenuation steps (wavelength independent), against which the attenuation measured by the spectrometer could be compared. This device was adopted by the EC concerted action on infra-red spectroscopy and imaging for the purpose of testing spectroscopy machines.

Finally, suggestions were made for the further development of the phantom to avoid some of the practical problems involved in its manufacture, and to give a phantom whose scattering coefficient can be theoretically calculated, and whose absorption properties can be altered to accurately match those of tissue.

References

1. (a) Jöbsis FF. (1977) Non invasive infrared monitoring of cerebral and myocardial oxygen sufficiency and circulatory parameters. *Science* **198** pp1264-7

1. (b) Profio AE, Navarro GA, Sartorius OW (1989) Scientific basis of breast diaphanography *Med. Phys.* **16** pp60-5

2. McCrea E. (1988) Mammography. *In: Clinical imaging. Ed: Freedman M. (Churchill Livingstone, New York)* pp205-14

3. Gravelle IH. (1993) Mammography. *In: A textbook of radiology and imaging. Ed: Sutton D. (Churchill Livingstone, Edinburgh)* Volume 2.

4. Walmsley BN. (1979) Computed tomography - equipment. *In: medical Imaging Ed: Kreel L. (HM & M. Pulishing Ltd. Aylsebury, England)* pp15-22

5. Feig SA. (1984) Radiation risk from mammography: is it clinically significant? *Am. J. Roent.* **143** pp469-75

6. Fox SA, Klos DS, Tsou CV. (1988) Underuse of screening mammography by family physicians. *Radiology* **166** pp431-3

7. Ott RJ, Flower MA, Babich JW, Marsden PK. (1990) The physics of radioisotope imaging. *In: The physics of medical imaging. Ed: Webb S. (Adam Hilger, Bristol)* pp142-318

8. Wells PNT. (1979) Theory of ultrasound. *In: Medical imaging. Ed: Kreel L. (HM&M Publishing Ltd. Aylesbury, England)* pp23-6

9. Westbrook C, Kaut C. (1993) MRI in practice *Blackwell Scientific PUblications (Oxford)*

10. Delpy DT, Cope M, van der Zee P, Arridge S, Wray S, Wyatt JW. (1988) Estimation of optical pathlength through tissue from direct time of flight measurement. *Phys. Med. Biol.* **32(12)** pp1433-42

11. Cope M, Delpy DT. (1988) System for long term measurement of cerebral blood and tissue oxygenation on newborn infants by near infrared transillumination. *Med. Biol. Eng. Comput.* **26(3)** pp289-94

12. Wyatt JS, Cope M, Delpy DT, van der Zee P, Arridge SR, Edwards AD, Reynolds EOR. (1990) Measurement of optical pathlength for cerebral near infrared spectroscopy in newborn infants. *Dev. Neuroscience* **12** pp140-4

13. van der Zee P, Cope M, Arridge SR, Essenpreis M, Potter LA, Edwards AD, Wyatt JS, McCormick DC Roth SC, Reynolds EOR, Delpy DT. (1992) Experimentally measured

pathlength for the adult head, calf and forearm and the head of the newborn infants as a function of inter optode spacing. *Adv. Exp. Med. and Biol.* **316** pp143-53

14. Jacques SL. (1991) Principles of phase resolved optical measurements. *SPIE* **1525** pp143-53

15. Sevick EM, Weng J, Maris M, Chance B. (1991) Analysis of absorption, scattering and hemoglobin saturation using phase modulation spectroscopy. *SPIE* **1431** pp264-75

16. Lakowicz JR, Berndt KW, Johnson ML. (1990) Photon migration in scattering media and tissue. *SPIE* **1204** pp468-80

17. Duncan A, Whitlock TL, Cope M, Delpy DT. (1993) Multiwavelength, wideband, intensity-modulated optical spectrometer for near IR spectroscopy and imaging. *SPIE* **1888** (In press)

18. Matcher SJ, Cope M, Delpy DT. (1993) Quantification of tissue chromophore concentration via 975 nm water peak measurements *SPIE* **1888** (In press)

19. Wickramasinghe Y, Thorniley M, Rolfe P, Houston R, Livera N, Faris F. (1990) Development of algorithms for non invasive neonatal cerebral monitoring using near infrared spectroscopy. *Proc. of 12th Inter. IEEE Conf. Eng. and Biol.* **12(4)** pp1554-5

20. Chance B, Maris M, Sorge J, Zhang MZ. (1990) A phase modulation system for dual wavelength difference spectroscopy of hemoglobin deoxygenation in tissues. *SPIE* **1024** pp481-91

21. Giannini I, Carta F, Ferrari M. (1984) Non invasive brain monitoring in near IR : a first analysis of human physiological data. *Proc. 2nd internat. Conf. on Appl. of Phys. to Med. and Biol. Ed: Bajzer Ž, Baza P, Franconi C.* pp521-2

22. Cutler M. (1929) Transillumination as an aid in the diagnosis of breast lesions. *Surg. Gynaecol. Obstet.* **48** pp 721-9

23. Ohlsson B, Gundersen J, Nilsson DM. (1980) Diaphonography: a method for evaluation of the female breast. *World J. Surg.* **4** pp701-6

24. Sickles EA. (1984) Breast cancer detection with transillumination and mammography. *Am. J. Roentgenol.* **142** pp841-4

25. Geslien GE, Fisher JR, DeLaney C. (1985) Transillumination in breast cancer detection: screening failures and potential. *Am. J. Roentgenol.* **144** pp619-22

26. Monsees B, Destouet JM, Gersell D. (1985) Light scan evaluation of nonpalpable breast lesions. *Radiology* **163** pp467-70

27. Jarry G, Ghesquiere S, Maarek HM, Fraysse F, Debray S, Bui-Mong-Hung, Laurent D. (1984) Imaging mammalian tissues and organs using laser collimated transillumination. *J. Biomed. Eng.* **6** pp70-4

28. Araki R, Nashimoto I. (1991) Near infrared imaging in vivo: imaging of Hb oxygenation in living tissues. *SPIE* **1431** pp321-32

29. He P, Kaneko M, Takai M, Baba K, Yamashita Y, Ohta K. (1990) Breast cancer diagnosis by laser transmission photo-scanning with spectro-analysis (report 4). *Radiat. Med.* **8(1)** pp1-5

30. Hebden JC. (1992) Evaluating the spatial resolution performance of a time resolved optical imaging system. *Med. Phys.* **19(4)** pp1081-7

31. Hounsfield GN. (1973) Computerized transverse axial scanning (tomography). *Br. J. Radiol.* **46** p1016

32. Maarek JM, Jarry G, Crowe J, Bui M-H, Laurent D. (1986) Simulation of laser tomoscopy in a heterogeneous biological medium. *Med. & Biol. Eng. & Comput.* **24** pp407-14

33. Hebden JC, Wong KS (1993) Time resolved optical tomography *Appl. Opt.* **32(4)** pp 372-89

34. Wang L, Liu Y, Ho PP, Alfano RR. (1991) Ballistic imaging of biomedical samples using picosecond optical kerr gate. *SPIE* **1431** pp97-101

35. Berg R, Andersson-Engels S, Jarlman O, Svanberg S. (1991) Time resolved transillumination for medical diagnostics. *SPIE* **1431** pp110-9

36. Benaron DA, Lenox MA, Stevenson DK. (1992) 2-D and 3-D images of thick tissue using time constrained times of flight and absorbance (tc-TOFA) spectrophotometry. *SPIE* **1641** pp35-45

37. Yoo KM, Das BB, Alfano RR. (1992) Imaging of a translucent object hidden in a highly scattering medium from the early portion of the diffuse component of a transmitted ultrafast laser pulse. *Optics Letters* **17(13)** pp958-60

38. Hebden JC, Delpy DT. (1994) Enhanced time resolved imaging with a diffusion model of photon transport. *Opt. Lett.* **19(5)** 311-3

39. Arridge SR, van der Zee P, Cope M, Delpy DT. (1991) Reconstruction methods for infra red absorption imaging. *SPIE* **1431** pp204-15

40. Bouger P (1729) Essai d'Optique sur la gradation de la lumiere *(Paris)*

41. Bouger P. (1760) Traite d'Optique sur la gradation de la lumiere. *(Paris)* Translated by WE Knowles Middleton (1961) Optical treatise on the gradation of light *Toronto Press, Toronto*

42. Lambert JH. (1760) Photometria sive de mensura et gradibus luminis colorum, et umbrae *Augsburg*

43. Beer A. (1852) Bestimmung der Absorption des rothen Lichts in farbigen Flussigkeiten. *Ann. Phys. u. Chem.* **163** p78

44. Woodard HQ, White DR. (1986) The composition of body tissues. *Br. J. Radiol.* **59** pp1209-19

45. Hale GM, Querry MR. (1973) Optical constants of water in the 200 nm to 200 μm wavelength region. *App. Opt.* **12(3)** pp555-63

46. Conway JM, Norris KH, Bodwell CE. (1984) A new approach for the estimation of body composition: infrared interactance. *Am. J. Clin. Nutri.* **40** pp1123-30

47. Filerup DL, Mead JF. (1967) The lipids of the aging human brain. *Lipids.* **2(4)** pp295-8

48. Zwart A, van Kampen EJ, Zijlstra WG. (1985) Multicomponent analysis of haemoglobin derivatives: clinical significance. *In: Physiology and methodology of blood gases and pH. Vol. 6. Ed: Maas AHJ et al. (Private press, Copenhagen)* pp97-107

49. Cope M. (1991) The development of a near infrared spectroscopy system and its application for non invasive monitoring of cerebral blood and tissue oxygenation in the newborn infant. *PhD Thesis, University of London.*

50. Tamura M, Nomura Y, Hazeki O. (1987) Laser tissue spectroscopy - near infrared CT. *Rev. Laser Eng. 15(8)* pp657-65

51. Henyey LS, Greenstein JL. (1941) Diffuse radiation in the galaxy. *Astrophys. J.* **93** pp70-83

52. van der Hulst HC. (1980) Multiple light scattering Vol 2. *Academic New York.*

53. Mie G. (1908) Beitrage zur optik trüber medien speziell kolloidaler metallösungen. *Ann. Phys.* **25** pp377-445

54. Bohren CF, Huffman DR. (1983) Absorption and scattering of light by small particles. *(John Wiley and sons, New York)*

55. Cauchy L. (1830) Sur la dispersion de la lumière. *Bull. des sc. math.* **14** 9

56. Twersky V. (1962) Multiple scattering of waves and optical phenomena. *J. Opt. Soc. Am.* **52** pp145-71

57. Kubelka P. (1948) New contributions to the optics of intensely light scattering materials Part I. *J. Opt. Soc Amer.* **38** pp448-57

58. Kubelka P. (1954) New contributions to the optics of intensely light scattering materials. PartII: Non homogeneous layers. *J. Opt. Soc Amer.* **44** pp330-5

59. van Gemert MJC, Star WM. (1987) Relations between the Kubelka Munk and the transport equation models for the anisotropic scattering. *Lasers Life Sci.* **1** pp287-98

60. Crinkworth BJ. (1972) Interpretation of the Kubelka Munk coefficients in reflection theory. *Appl. Opt.* **11** pp1434-5

61. van Gemert MJC, Schets GACM, Bishop MS, Cheong W-F, Welch AJ (1988) Optics of tissue in a multi layer slab geometry. *Lasers Life Sci.* **2(1)** pp1-18

62. Welch AJ, Yoon H, van Gemert MJC. (1988) Practical models for light distribution in laser irradiated tissues. *Lasers Surg. Med.* **6** pp488-93

63. Case KM, Zweifel PF. (1967) Linear transport theory. *Addison Wesley Publishing Co. (New York)*

64. Chandrasekhar S. (1950) Radiation transfer. *Clarendon Press. (Oxford)*

65. Ishimaru A. (1978) Wave propagation and scattering in random media. *Academic press (New York).*

66. van der Hulst HC. (1980) Multiple light scattering. *Academic press (New York).*

67. Duderstadt JJ, Hamilton LJ. (1976) Nuclear reactor analysis. *John Wiley and Sons, New York.*

68. Lewis HW. (1950) Multiple scattering in an infinite medium. *Physical review.* **78(3)** pp526-9

69. Bremmer H. (1964) Random volume scattering. *Radio Sci. J. Research.* **680(9)** pp967-81

70. Arridge S, van der Zee P, Delpy DT, Cope M. (1990) Aspects of clinical infra red absorption imaging. *In: The formation, handling and evaluation of medical images. Ed Todd-Pokropek A, Vierger. MA (Springer Verlag, Berlin)* pp407-18

71. Patterson MS, Wilson BC, Wyman DR. (1991) The propagation of optical radiation in tissue I Models of radiation transport and their application. *Lasers in Med. Sci.* **6** pp155-68

72. Groenhuis RAJ, Ferwada HA, Ten Bosch JJ. (1983) Scattering and absorption of turbid materials determined from reflection measurements. 1 : theory. *Appl. Optics.* **22** pp2456-62

73. Reynolds L, Johnson C, Ishimaru A. (1976) Diffuse reflectance from a finite blood medium: applications to the modeling of fiber optic catheters. *Appl. Optics.* **15(9)** pp2059-67

74. Haselgrove J, Leigh J, Yee C, Wang N-G, Maris M, Chance B. (1991) Monte Carlo and diffusion calculations of photon migration in non-infinite highly scattering media. *SPIE* **1431** pp30-41

75. Arridge SR, Cope M, Delpy DT. (1992) The theoretical basis for the determination of optical pathlengths in tissue : temporal and frequency analysis. *Phys. Med. Biol.* **37(7)** pp1531-60

76. McKenzie AL. (1985) How may external and interstitial illumination be compared in laser photodynamic therapy. *Phys.Med Biol.* **30** pp455-60

77. Allen V, McKenzie AL. (1991) The modified diffusion dipole model. *Phys. Med. Biol.* **36(12)** pp1621-38

78. Patterson MS, Chance B, Wilson BC. (1989) Time resolved reflectance and transmittance for the non invasive measurement of tissue optical properties. *Appl. Opt.* **28** pp2331-6

79. Cheong W-F, Prahl SA, Welch AJ. (1990) A review of the optical properties of biological tissues. *IEEE J. of Quantum Elec.* **26(12)** pp2166-85

80. Star WM. (1989) Comparing the P3 approximation with diffusion theory and with Monte Carlo calculations of light propagation in a slab geometry. *SPIE* **1035** pp146-54

81. Arridge SR, Schweiger M, Hiraoka M, Delpy DT. (in press) A finite element model for photon transport in tissue. *Phys Med. Biol.*

82. Suddeath L, Sevick EM. (1993) Forward imaging using time and frequency resolved technique. *SPIE* **1888** in press

83. Yamada Y, Hasegawa Y. (1993) Time dependent FEM analysis of photon migration in random media. *SPIE* **1888** in press

84. Bonner RF, Nossal R, Havlin S, Weiss GH. (1987) Model for photon migration in turbid biological media. *J. Opt. Soc. Am.* **A4** pp423-32

85. Grünbaum FA, Kohn P, Latham GA, Singer JR, Zubelli JP. (1991) Diffuse tomography. *SPIE.* **1431** pp232-8

86. Schlereth FH, Fossaceca JM, Keckler AD, Barbour RL. (1992) Imaging in diffusing media by a progressive iterative backprojection method using time domain data. *SPIE* **1641** pp46-57

87. Chandrasekhar S. (1943) Stochastic problems in physics and astronomy. *Rev. Mod. Phys.* **15** pp1-89

88. Essenpreis M, van der Zee P, Mills TN. (1991) Monte Carlo modelling of light transport in tissue: The effect of laser coagulation on light distributions. *SPIE.* **1524**

89. Donnelli P, Bruscaglioni P, Ismelli A, Zaccanti G. (1991) Experimental validation of a Monte Carlo procedure for the evaluation of the effect of a turbid medium on the point spread function of an optical system. *J. Mod. Opt.* **38** pp2189-201

90. Flock ST, Patterson MS, Wilson BC, Wyman DR. (1989) Monte Carlo Modeling of light propagation in highly scattering tissues - I: model predictions and comparison with diffusion theory. *IEEE Trans. Biomed. Eng.* **36(12)** pp1162-8

91. Jacques SL. (1989) Time resolved propagation of ultrashort laser pulses within turbid tissues. *Appl. Opt.* **28(12)** pp2223-9

92. Key H, Davies ER, Jackson PC, Wells PNT. (1991) Monte Carlo modelling of light propagation in breast tissue. *Phys. Med. Biol.* **366** pp591-602

93. Peters VG, Wyman DR, Patterson MS, Frank GL. (1990) Optical properties of normal and diseased human breast tissues in the visible and near infrared. *Phys. Med. Biol.* **35** pp1317-34

94. van der Zee P. (1992) Measurement and modelling of the optical properties of human tissue in the near infrared. *PhD Thesis, University of London.*

95. Hiroaka M, Firbank M, Essenpreis M, Cope M, Arridge SR, van der Zee P, Delpy DT. (1993) A Monte Carlo investigation of optical pathlength in inhomogeneous tissue and its application to near-infrared spectroscopy. *Phys. Med. Biol.* **38** pp1859-76

96. Flock ST, Wilson BC, Patterson MS. (1987) Total attenuation coefficients and scattering phase functions of tissues and phantom materials at 633 nm. *Am. Assoc. Phys. Med.* **14(5)** pp835-41

97. Key H, Davies ER, Jackson PC, Wells PNT. (1991) Optical attenuation characteristics of breast tissues at visible and near-infrared wavelengths. *Phys. Med. Biol.* **36(5)** pp579-90

98. Essenpreis M. (1993) Thermally induced changes in optical properties of biological tissues. *PhD Thesis, University of London.* Chapter 5

99. Wilksch PA, Jacka F, Blake AJ. (1984) Studies of light propagation through tissue. *In:Porphyrin localization and treatment of tumors. Ed: Doiron DR, Gomer CJ (Alan R Liss Inc., New York)* pp149-61

100. Marchesini R, Bertoni A, Andreola S, Melloni E, Sichirollo AE. (1989) Extinction and absorption coefficients and scattering phase functions of human tissues in vitro. *Appl. Opt.* **28(12)** pp2318-24

101. van der Zee P, Delpy DT. (1988) Computed point spread functions for light in tissue using a measured volume scattering function. *Adv. Exp. Med & Biol.* **222** pp191-7

102. Handbook of chemistry and physics. (1974) *CRC Press Ed R.C. Weast.*

103. Prahl SA, van Gemert MJC, Welch AJ (1993) Determining the optical properties of turbid media by using the adding-doubling method. *Appl. Opt.* **32(4)** 559-568

104. Graaff R, Dassel ACM, Koelink MH, de Mul FFM, Aarnoudse JG, Zijlstra WG. (1993) Optical properties of human dermis in vitro and in vivo. *Appl. Opt.* **32(4)** 435-47

105. Sterenborg HJCM, van Gemert MJC, Kamphurst W, Wolbers JG, Hogervosrst W (1989) The spectral dependance of the optical properties of human brain. *Las. Med. Sci.* **4** pp221-7

106. Splinter R, Cheong WF, van Gemert MFC, Welch AJ. (1989) in vitro optical properties of human and canine brain and urinary bladder tissues at 633 nm. *Las. Surg. Med.* **9** pp37-41.

107. Groenhuis RAJ, Ferwada HA, Ten Bosch JJ. (1983) Scattering and absoption of turbid materials determined from reflection measurements 1: theory. *Appl. Opt.* **22(16)** 2456-2462

108. Madsen SJ, Wilson BC, Patterson MS, Park YD, Jacques SL, Hefetz Y. (1992) Experimental tests of a simple diffusion model for the estimation of scattering and absorption coefficients of turbid media from time resolved diffuse reflectance measurements. *Appl. Opt.* **31(18)** 3509-17

109. Prahl SA, Vitkin IA, Bruggemann U, Wilson BC, Anderson RR. (1992) Determination of optical properties of turbid media using pulsed photothermal radiometry. *Phys. Med. Biol.* **37(6)** pp 1203-17

110. van der Zee P, Essenpreis M, Delpy ST, Cope M. (1991) Accurate determination of the optical properties of biological tissues using a Monte Carlo inversion technique. *Proc ICO meeting atmospheric, volume and surface scattering and propagation. Florence, Italy.* pp125-8

111. Barilli M, Zaccanti G, Bruscaglioni P, Ismaelli A, Wei QN, Ferrari M. (1992) Optical properties of in vivo human skeletal muscle from near infrared picosecond laser pulse. *In Photodynamic therapy and biomedical lasers. Ed: Spinelli P et al (Elsevier, Amsterdam).* pp930-4

112. Cope M, Delpy DT, Wray S, Wyatt JS, Reynolds EOR. (1989) A CCD spectrometer to quantitate the concentration of chromophores in living tissue utilising the absorption peak of water at 975 nm. *Adv. Exp. Med. Biol.* **247** pp33-40

113. American Institute Physics Handbook (1972) *McGraw Hill (New York)*

114. Pickering JW, Moes CJM, Sterenborg HJCM, Prahl SA, van Gemert MJC (1992) Two integrating spheres with an intervening scattering sample. *J. Opt. Soc. Am. : Part A* **9(4)** pp621-31

115. Ojala KT, Koshi E, Lampinen MJ. (1992) Reflection and transmission measurements wiht an integrating sphere and Fourier transform infra red spectrometer. *Appl. Opt.* **31(22)** pp4582-9

116. Hecht E (1989) Optics *Addison-Wesley (Massachusetts)* Chapter 4

117. Patterson MS, Chance B, Wilson BC (1989) Time resoolved reflectance and transmittance for the non-invasive measurement of tissue optical properties. *Appl. Opt.* **28(12)** pp2331-6

118. Duplain G, Boulay R, Belanger PA. (1987) Complex index of refraction of dental enamel at CO_2 laser wavelengths. *App. opt.* **26** pp4447-51

120. Hancox NM. (1972) Biology of bone. *(Cambridge University Press)*

121. Firbank M, Hiraoka M, Essenpreis M, Delpy DT. (1993) Measurements of the optical properties of the skull in the wavelength range 650-950 nm. *Phys. Med. Biol.* **38** pp503-9

122. White DR, Widdowson EM, Woodard HQ, Dickerson WT. (1991) The composition of body tissues. *Br. J. Radiol.* **64** pp149-59

123. Posner AS. (1987) Bone mineral and the mineralisation process. *In: Bone and mineral research Ed. Peck WA.* pp65 - 116

124. Linford J, Shalev S, Bews J. (1986) Development of a tissue equivalent phantom for diaphanography. *Med. Phys.* **13(6)** pp869-75

125. Patterson MS, Schwartz E, Wilson BC. (1989) Quantitative reflectance spectrophotometry for the noninvasive measurement of photosensitizer concentration in tissue during photodynamic therapy. *SPIE* **1065** pp115-22

126. Jacques SL, Flock ST. (1991) Time resolved reflectance spectroscopy. *SPIE* **1525** pp35-40

127. Berg R, Andersson-Engels S, Jarlman O, Svanberg S. (1991) Tumor detection using time resolved light transillumination. *SPIE* **1525** pp59-67

128. Sun W, Li J, Li W, Lin Y, Ying J. (1992) Diffuse reflection measurements determining optical properties of tissues. *SPIE* **1645** pp216-228

129. Delpy DT, Arridge SR, Cope M, Edwards D, Reynolds EOR, Richardson CE, Wray S, Wyatt J, van der Zee P. (1989) Quantitation of pathlength in optical spectroscopy. *Adv. Exp. Med. & Biol.* **248** pp41-6

130. Wilson BC, Farrell TJ, Patterson MS. (1990) An optical fiber based diffuse reflectance spectrometer for non invasive investigation of photodynamic sensitizers in vivo. *SPIE* **IS6** pp219-32

131. Kaneko M, Hatakeymama M, He P, Nakajima Y, Isoda H, Takai M, Okawada T, Asumi M, Kato T, Goto S, Sugie Y, Hayashi T, Hayakawa T, Yamashita Y, Ohta K. (1989) Construction of a laser transmission photo scanner : pre clinical investigation (report 2). *Radiat. Med.* **7** pp129-134

132. Chance B, Haselgrove J, Wang N-G, Maris M, Sevick E. (1991) Photon dynamics in tissue imaging. *SPIE* **1525** pp68-82

133. Graber HL, Barbour RL, Lubowsky J, Aronson R, Das BB, Yoo KM, Alfano RR. (1992) Evaluation of steady state, time and frequency domain data for the problem of optical diffusion tomography. *SPIE* **1641** pp6-20

134. van Staveran HJ, Moes CJM, van Marie J, Prahl SA, Gemert MJC. (1991) Light scattering in intralipid 10% in the wavelength range of 400-1100 nm. *Appl. Opt.* **30(31)** pp4507-14

135. Madsen SJ, Patterson MS, Wilson BC. (1992) The use of india ink as an optical absorber in tissue simulating phantoms. *Phys. Med. Biol.* **37** pp985-3

136. Firbank M, Delpy DT (1993) A design for a stable and reproducible phantom for use in near infra-red imaging and spectroscopy. *Phys. Med. Biol.* **38** pp847-53

137. Firbank M, Delpy DT. (1994) A phantom for the testing and calibration of near infra-red spectrometers. *Phys. Med. Biol.* **39** pp1509-13

138. Schweiger M, Arridge SR, Hiraoka M, Firbank M, Delpy DT. (1993) Comparison of a finite element forward model with experimental phantom results: application to image reconstruction. *SPIE* **1993** pp179-190

139. Schweiger M (1994) Thesis in preparation (University of London)

140. Torres JH, Welch AJ, Çilesiz I, Motamedi M (1994) Tissue optical property measurements: overestimation of absorption coefficient with spectrophotometric techniques. *Las. Surg. Med.* **14** pp249-57

141. Graaff R, Dassel ACM, Koelink MH, Aarnoudse JG, de Mul FFM, Zijlstra WG, Greve J (1993) Condensed Monte Carlo simulations applies to reflectance pulse oximetry *Proc SPIE* **1888** pp201-12

142. Farrell TJ, Patterson MS. (1992) A diffusion theory model of spatially resolved steady-state diffuse reflectance for the noninvasive determination of tissue optical properties in vivo. *Med. Phys.* **19(4)** pp879-88

143. Splinter R, Svenson RH, Littmann L, Tuntelder JR, Thompson M, Tatsis GP, Chuang CH. (1992) Determination of optical properties in-situ from radial backscattering profile using a CCD camera. *SPIE* **1646** pp376-82